NUMERICAL STUDIES ON MANY-BODY LOCALIZATION

BY

BENJAMIN VILLALONGA CORREA

DISSERTATION

Submitted in partial fulfillment of the requirements
for the degree of Doctor of Philosophy in Physics
in the Graduate College of the
University of Illinois at Urbana-Champaign, 2020

Urbana, Illinois

Doctoral Committee:

Professor Taylor L. Hughes, Chair
Assistant Professor Bryan K. Clark, Director of Research
Professor Bryan L. DeMarco
Professor Jun Song

Abstract

Under certain conditions, an interacting system can defy the concept of thermalization, a keystone in our understanding of physical processes. Many-body localization (MBL) is a phase of matter in which thermalization does not apply and ergodicity is broken. This striking behavior, which can appears on closed, interacting, quantum systems subject to strong disorder, has been the focus of a large body of theoretical, numerical, and experimental work in recent years. In this thesis we numerically study several aspects of MBL and the ergodic-MBL transition.

Chapter 1 introduces the concept of thermalization in quantum systems, which relies on the idea of the eigenstate thermalization hypothesis (ETH). I then present localization as a phenomenon that breaks ETH, both in its single-particle as in its many-body versions. I discuss some of the main aspects that are known about MBL, as well as some of its open questions, some of which we tackle in later chapters.

Chapter 2 discusses the main numerical methods used in this thesis for the study of MBL. I provide both theoretical background as well as discuss some more practical matters, such as their advantages and disadvantages, or details on the software developed/used in my studies.

In Chapter 3 I present our work on MBL from the point of view of single-particle orbitals. In this work we access a complete set of approximate integrals of motion of a one-dimensional system by computing the one-particle orbitals (OPO) of highly-excited MBL energy eigenstates, which are obtained through the shift-and-invert matrix product state (SIMPS) algorithm. We then study the properties of the OPOs over large systems, up to $L = 64$. We find that the OPOs drawn from eigenstates at different energy densities have high overlap and their occupations are correlated with the energy of the eigenstates. Moreover, the standard deviation of the inverse participation ratio of these orbitals is maximal at the nose of the mobility edge. Also, the OPOs decay exponentially in real space, with a correlation length that increases at low disorder. In addition, we find that the probability distribution of the strength of the large-range coupling constants of the number operators generated by the OPOs approach a log-uniform distribution at strong disorder.

In Chapter 4 I present our work on the hybridization of eigenstates in either the MBL or the ergodic phase,

as well as at the transition. We do so by adiabatially evolving highly excited eigenstates of the Hamiltonian and measuring their their hybridization process with other eigenstates of the system. This hybridization, which dresses the eigenstate and has the potential of bringing it out of the MBL phase through the transition, is a consequence of the "collisions" of eigenstates in energy, which avoid level crossings every time their energy gap is small. The hybridization of eigenstates with each other involves only local regions of the system in the MBL phase, ignores locality in the ergodic phase, and is range-independent at the transition. This range independence suggests the proliferation of long-range resonances at the transition, as well as the divergence of a localization length.

In Chapter 5 I present our studies on the typical and extreme (atypically strong) correlations across a one-dimensional system in the ergodic-MBL phase diagram. While typical correlations decay exponentially with range in the MBL phase, in the ergodic phase they are constant and independent of the range. Surprisingly, we identify a moderate region of the phase in which typical correlations decay as a stretched exponential with range r, and in particular as $e^{-\sqrt{r}}$ at the transition, a decay that is reminiscent of the random singlet phase. Moreover, at the transition the distribution of the logarithm of the correlations show vanishing even excess moments and non-zero range-invariant odd excess moments. This distinct behavior at the transition is in contrast with ergodic and MBL phenomenologies. In addition, we study the extreme correlations in the system. Our results suggest that strong long-range correlations proliferate at the transition, in contrast with a decay with range in the MBL phase and the lack of strong long-range correlations in the ergodic phase. Finally, we analyze the probability that a single bit of information is shared across two halves of a system, which has been proposed as a robust order parameter in the ergodic-MBL phase diagram. We find that this probability is non-zero deep in the MBL phase, but vanishes at moderate disorder, well above the transition, thus not providing a proper order parameter.

Chapter 6 I summarize the work presented with an emphasis on context and perspective.

To my parents, whose love not only gave me life, but made it meaningful in more ways than I can count.

Acknowledgments

I would like to thank all the people that have been with me in the years I have spent in Urbana-Champaign, either physically present or in spirit. My biggest thanks go to my advisor, Assistant Professor Bryan K. Clark, for teaching me how to think, how to write, and how to persist, in a scientific way. He convinced me of many things, and a few of them come to mind. On the technical side, I will always remember that "The universe is probably a quantum computer". Also, I am now convinced that "If we have data, we should analyze it!" as a fundamental part of the discovery process. On the mentoring side, he convinced me that caring about the well-being and the opinion of our coworkers can have a large impact in the outcome of a group endeavor. With his infinite patience, he allowed me to explore other paths and was always willing to spend time solving and advising on non-scientific problems that might get on the way of my ultimate scientific goals.

I owe special thanks to Salvatore Mandrà and Sergio Boixo for their mentorship over the last two years of my PhD. Both of them introduced me to the world of quantum computing and let me work in some of the most exciting projects a could have ever dreamt of. Beyond science and career advice, they were supportive at all times beyond all expectations.

I am also grateful to all of the present and past members of the Clark Group I have closely worked with: David, Xiongjie, Dima, Eli, Ryan, Gabi, Greg, and Di. They offered me help whenever needed, as well as sparked some of the most interesting conversations about research I have had. From them I have learnt a large fraction of what grad school has given me.

Although living different continents, my parents and my siblings, Bernardo and Agustina, have been an integral part of my experience in America. Their support is truly unconditional. They are the strongest connection I have to my past and my culture, and having them in the present is a blessing that I am very proud of and grateful for.

I would also like to thank the many people I have met through these years. From them, a portion have become some of my closest friends, roommates, and amazing partners.

Last, but not least, I owe big thanks to Professor S. Lance Cooper, as well as to Mel Schweighart and

Wendy Wimmer. They made the Physics Department at the UIUC a very welcoming and pleasant place to be at, and made grad school as smooth an experience as possible.

This thesis is based upon work supported by the U.S. Department of Energy, Office of Science, Office of Advanced Scientific Computing Research and Office of Basic Energy Sciences, Scientific Discovery through Advanced Computing (SciDAC) program under Award Number de-sc02-12ER46875. This thesis is also based upon work supported by the Department of Energy grant DOE de-sc0020165. In addition, I acknowledge support from the Google AI Quantum team. All projects in this thesis are part of the Blue Waters sustained petascale computing project, which is supported by the National Science Foundation (awards OCI-0725070 and ACI-1238993) and the State of Illinois. Blue Waters is a joint effort of the University of Illinois at Urbana-Champaign and its National Center for Supercomputing Applications.

Contents

List of Abbreviations

CDF	Cumulative distribution function.
DMRG	Density matrix renormalization group.
ED	Exact diagonalization.
EE	Entanglement entropy.
FMBL	Fully many-body localized.
MBL	Many-body localization or many-body localized.
OPDM	One-particle density matrix.
OPO	One-particle orbital.
PDF	Probability distribution function.
QMI	Quantum mutual information.
SDRG	Strong disorder renormalization group.
SIMPS	Shift-and-invert matrix product state.
WWF	Wegner-Wilson flow.

Chapter 1

Introduction

In this chapter we motivate and introduce the concepts of *thermalization* and *localization*, provide some background, and give an overview of what is known and what are the open questions in the *many-body localization* problem. First, we describe the concept of thermalization. We then introduce many-body localization as an example of systems that do not thermalize. Then, we focus on the phase diagram of the standard model of many-body localization and discuss what has been learnt from it, as well as the questions that remain open.

1.1 Thermalization

All of us have learnt from our daily life experience that a hot cup of coffee that is left on top of a kitchen counter will eventually get colder, and that a glass of cold water placed outside in a summer day will not remain that cold for too long. This process, in which a small system that is out of equilibrium with its surroundings progressively finds a mutual equilibrium receives the name of *thermalization*. Based on evidence, we assume that, if physics behaves the way it usually does, then thermalization should continue to be a keystone in our understanding of nature. The day thermalization breaks, we would be extremely surprised, but we would also wonder under what conditions this happens, in what ways our description of physical processes has failed, how could the lack of thermalization expand our understanding of nature, and, perhaps, to what extent can this novel behavior be exploited as a technological resource.

Such a familiar process is manifested in the *macroscopic* degrees of freedom of the systems we observe. For any *microscopic* description of these systems (at the level of single or a few particles) to be reconciled with our macroscopic observations, we should require therefore that it restores thermalization when used to describe a large number of particles, *i.e.* in the so-called *thermodynamic limit*.

1.1.1 Thermalization from quantum mechanical microscopic descriptions

This section is partially based on Ref. [63], which is an excellent review of thermalization and MBL can be found in.

Let us have a quantum mechanical description of the microscopic degrees of freedom of a system. To be more specific, let us describe both system (A) and surroundings (B, with size $|B| \gg |A|$) by the same theory, which encodes how A and B behave, as well as how they interact with each other. The combination of $A + B$ can now be considered as a single, closed system. The system $A + B$ is closed in the sense that it is described by a Hamiltonian, H, which has no terms coupling its degrees of freedom to those that might have support outside $A + B$. Let us now considered an extensive conserved quantity of the system; H is time-independent, so we already guarantee by definition that the energy is conserved, but we could have Hamiltonians that preserve other extensive quantities, like magnetization or charge. Extensive conserved quantities are interesting because they must satisfy a continuity equation, *i.e.*, if the density of this quantity decreases on some region, it must increase at a different one, in order to preserve the total amount. In turn, what this means is that we find transport of this quantity: we can transport energy across the system, as well as spin or charge, if either magnetization or total charge are conserved.

For transport to be a physical process [1] , we must have some notion of space or locality, *i.e.*, we must have a sense of whether two regions of the system are contiguous or far from each other; similarly, and closely related to locality, we must have a notion of dimensionality: are we describing a wire in one dimension, a sheet of material in two dimensions, or a slab of material that fills all three dimensions of space? In fact, it turns out that, since all couplings that appear in nature are local, that is, all terms that contribute to the energy of a system only couple degrees of freedom that are close to each other, for a Hamiltonian to be physical it has to be the sum of only local coupling terms; we will come to this later. This sense of locality in the structure of the Hamiltonian results in a notion of locality in all transport phenomena and is well studied by the beautiful theory behind the Lieb-Robinson bounds [51], which guarantee that causality holds; as a consequence, for example, some charge that is being transported from one region to another of the system has to travel sequentially through contiguous regions and cannot "jump" directly from its origin to its destination.

The process of thermalization is intimately related to the concept of transport. Given a distribution of a conserved quantity (*e.g.* energy) with a density imbalance between different regions of a system, it is the transport of this precise quantity that lets us recover a state of equilibrium in which all regions have the same density, provided that we give it enough time. The question now is: do all physical (local) quantum

[1] Here we refer to the word physical as describing a process that could reasonably appear in nature, *i.e.*, a process that could in principle physically take place, as opposed to a hypothetical process that is far from reality.

Hamiltonians guarantee thermalization of the closed systems they describe, in the thermodynamic limit? In other words, do all small regions, A, equilibrate with their surroundings, B, provided the dynamics imposed by the local Hamiltonian H_{A+B}, and the limit $|B| \to \infty$? The answer to this question is *no*, but we will learn more about thermalization, its implications, and its assumptions on quantum models before we dive into its breakdown in Section 1.2.

Formalism

Let us have a Hamiltonian, H, defined over a system $A + B$ in the state described at time t by the density matrix $\rho(t)$. Note that we have assumed that the Hamiltonian, and hence the dynamics of the system, have no terms that couple degrees of freedom outside the system with those internal to the system. However, the generality of the density matrix formalism allows for the preparation of a state that is entangled with the degrees of freedom external to the system. [2] The evolution of $\rho(t)$ is given by

$$\rho(t) = e^{-itH/\hbar}\rho(0)e^{itH/\hbar}. \tag{1.1}$$

Given any observable O defined over the system, the expectation value of O is $\langle O\rangle = \mathrm{Tr}\left[\rho(t)O\right]$. Equivalently, for an observable O_A defined over a compact subsystem (small, for our purposes) A, which we call a local observable, the expectation value is $\langle O_A\rangle = \mathrm{Tr}\left[\rho_A(t)O_A\right]$, where ρ_A describes the state in A and is referred to as the reduced density matrix over A: $\rho_A(t) \equiv \mathrm{Tr}_B\left[\rho(t)\right]$, where Tr_B traces out all degrees of freedom of B.

Thermalization under this formalism can be expressed in the following way: for a system initialized at a certain energy E and with small fluctuations around it ($\sigma(E)$ small) in the limit of $t \to \infty$ and $|B| \to \infty$, while keeping the size $|A|$ constant, all extensive conserved quantities O that are sums of local observables reach time-averaged densities that are constant in time and equal across all local subregions, *i.e.* $\frac{\overline{\langle O_A\rangle}}{|A|}$ is independent of A and becomes time independent in the $t \to \infty$ limit. Moreover, the time-averaged expectation value of this observable is equal its thermal value, for a temperature T which is a function of the initial energy of the system: $\langle E(0)\rangle = \frac{\mathrm{Tr}\left[e^{-H/T}H\right]}{\mathrm{Tr}\left[e^{-H/T}\right]}$. This means that the final state of a system that is initialized with $\langle O\rangle$ and evolved in time (assuming we consider a large enough system and large enough times) is, as far as local observations are concerned, independent of the details of the initial state. This might seem like a contradiction, since the evolution given by Eq. (1.1) is unitary, and all unitary evolutions are reversible, which implies that we should be able to infer the initial state of the time evolution from its

[2] This can be achieved during the preparation of the state, *i.e.*, by evolving the system and the outside degrees of freedom with a Hamiltonian that *does* couple internal and external degrees of freedom, but "turning off" those couplings after the preparation, *e.g.* at time $t = 0$.

final state. The way out of this paradox turns out to be hidden, once again, in the use of the concept of locality: even though the local degrees of freedom of the system lose the memory of the initial conditions of the time evolution, we have not ruled out the possibility of encoding these initial conditions in a global way, which is only accesible by global observables. Without violating the unitarity of the time evolution of the system, an observer that has access only to local observations over the system has lost by all means the ability to backtrack the trajectory of the system, and with it the ability to infer its initial state; in that sense, the system has (locally) lost memory of its initial conditions, which are now accessible only through non-local, unphysical, observables.

Is thermalization as presented in this section a reasonable thing to expect from reasonable microscopic models that aim at describing physical macroscopic systems? On the one hand, under certain assumptions, this is a very reasonable expectation: generic models do indeed thermalize as expected. On the other hand, the concept of *localization* (see Section 1.2) arises on a family of reasonable, physical models that present phenomenology that defies thermalization, which is the subject of this thesis. In the next section we present the eigenstate thermalization hypothesis, which elaborates on the concept of thermalization in closed quantum systems.

The eigenstate thermalization hypothesis

Let us have a thermalizing system that is described by a Hamiltonian H. This means that, at large times and in the thermodynamic limit, all subsystems A (small compared to the full isolated $A+B$, *i.e.*, subsystem plus surroundings) equilibrate with each other and present local observables that are in agreement with the initial values of the extensive conserved quantities of the system. More strongly, the reduced density matrix over A becomes at large times equal to the reduced density matrix $\rho_A(t \to \infty) = \rho_A^{\text{thermal}}(T) = e^{-\beta H_A}$, which is the thermal reduced density matrix at temperature $T = \beta^{-1}$ over subsystem A, and where H_A is the Hamiltonian H constrained to subsystem A. For all local observables over A, the expectation value is computed as:

$$\langle O_A \rangle = \frac{\text{Tr}\left[e^{-\beta H_A} O_A\right]}{Z_A}, \tag{1.2}$$

where $Z_A \equiv \text{Tr}\left[e^{-\beta H_A}\right]$ is the partition function. Local observables become therefore a smooth function of the temperature. By extension, the energy is also a smooth function of the temperature. All local observables are therefore smooth functions of the energy at which the system was initialized.

The eigenstate thermalization hypothesis arises from the following consideration. In the case that the system is initialized in an eigenstate of H, $|n\rangle$, then its evolution is stationary and the state of the system

already equals its long-time limit. For this reason, an eigenstate $|n\rangle$ should look thermal over subsystems that are small compared to the full size of the system: $\rho_A^n = e^{-\beta H_A}$. [3] The statement that eigenstates of a system look thermal over small subsystems is known as the eigenstate thermalization hypothesis (ETH).

A consequence of the ETH is that local observables should be a smooth function of the energy of the eigenstates. States that are superpositions of eigenstates that lay over a small energy window should also present observables that are functions of the energy in the same way. The fact that a system satisfies this condition is an indication that the it is in a thermal phase. On the contrary, if the local observables of a system vary wildly from eigenstate to eigenstate, then it breaks down the ETH, and thermalization does not apply.

Thermalization and ergodicity

The terms *thermal* and *ergodic* are used interchangeably in the literature of MBL. In classical statistical mechanics, ergodicity means that the long time average of a quantity is equal to a statistical average over microstates of the statistical ensemble. In quantum mechanics, we require that the long time average of a local observable is equal to the average of the observable over the microcanonical ensemble, *i.e.* over eigenstates laying in a narrow window in energy.

Following the discussion of Ref. [79], let us be more specific and consider the matrix elements of an observable $O^A_{mn} = \langle m| O |n\rangle$ for all pairs of eigenstates of H. Let us now initialize a state (pure, for simplicity) $|\psi(0)\rangle = \sum_n c_n |n\rangle$ which has energy E and a narrow value of $\sigma(E)$. The expectation value of O^A is initially equal to $\langle O\rangle = \sum_{mn} c^*_m c_n O^A_{mn}$. As we evolve $|\psi(t)\rangle$ in time, we get: $\langle O(t)\rangle = \sum_{mn} c^*_m c_n e^{-i(E_n - E_m)t} O^A_{mn}$. The long time average of $\langle O^A\rangle$ is:

$$\overline{\langle O^A\rangle} = \lim_{t\to\infty} \frac{1}{t}\int_{\tau=0}^{t} \langle O^A(\tau)\rangle d\tau = \lim_{t\to\infty} \frac{1}{t}\int_{\tau=0}^{t} \sum_{mn} c^*_m c_n e^{-i(E_n-E_m)\tau} O^A_{mn} d\tau = \sum_n |c_m|^2 O^A_{mm}, \tag{1.3}$$

where in the last step the off-diagonal terms of the observable, O^A_{mn}, for $m \neq n$, average to 0.

Let us now compute the average of the local observable O^A over eigenstates in a narrow window in energy of width ΔE around E:

$$\langle O^A\rangle^{\text{microcanonical}} = \frac{1}{N_{E,\Delta E}} \sum_{|E-E_n|<\Delta E} O^A_{nn}, \tag{1.4}$$

where $N_{E,\Delta E}$ is the number of eigenstates the lay in the energy window considered.

[3] In fact, this should be the case for any density matrix over the system that is diagonal when written in the basis of eigenstates of H; single eigenstates just represent the pure-state subset of these.

Ergodicity requires the left hand side terms of Eqs. (1.3) and (1.4) to be equal. While $\overline{\langle O^A \rangle}$ depends on the initial conditions of $|\psi(0)\rangle$ through $\{c_n\}$, $\langle O^A \rangle^{\text{microcanonical}}$ does not. The only way to satisfy ergodicity is therefore to require that the expectation values O^A_{nn} for all eigenstates in the narrow energy window are very close to each other or, in other words, that $\langle O^A \rangle_n$ is a smooth function of the energy of the eigenstates E_n, which is precisely stated by the ETH.

Note that so far we have only required that the time average of O^A is equal to the microcanonical average. In the stronger case where the expectation value of O^A (rather than its time average) approaches its thermal value, we require the off-diagonal terms in Eq. (1.3) to contribute very little. In particular, for a constant $\sigma(E)$ of the initial state $|\psi(0)\rangle$, the number of eigenstates considered grows with the dimension of the Hilbert space, $\mathcal{D}$, which grows exponentially with system size. If we want the fluctuations introduced by these off-diagonal terms to vanish in the thermodynamic limit (note that we cannot rely anymore on their time averate to vanish), then we need to require that the off-diagonal terms themselves vanish exponentially with system size, *i.e.*, that $O^A_{mn} \propto (e^{-\mathcal{D}})$, for $m \neq n$.

In systems for which ETH is satisfied, ergodicity is automatically satisfied. As is done in the literature, we will use the terms *thermal* and *ergodic* interchangeable to refer to generic systems that thermalize, as opposed to non-thermalizing MBL systems.

1.2 Localization

The concept of localization is central to the study of systems that break down thermalization. Most studies over many decades have focused on single-particle localization, known as Anderson localization, which we briefly discuss in Section 1.2.1. In Section 1.2.2 we introduce the interacting version of Anderson localization, which has been the subject of extensive study in recent years, and is known as many-body localization.

1.2.1 Anderson localization

The concept of localization was introduced by Anderson in his 1958 seminal paper of Ref. [7]. Anderson localization involves non-interacting Hamiltonians with disorder, such as the following fermionic, quadratic Hamiltonian:

$$H = t \sum_{\langle ij \rangle} \left(c_i^\dagger c_j + c_j^\dagger c_i \right) + \sum_i \mu_i c_i^\dagger c_i, \tag{1.5}$$

where, $\{c_i^\dagger\}$ are fermionic cration operators, t is the strength of the nearest-neighbor hopping term, and $\{\mu_i\}$ are random on-site potentials. The model of Eq. (1.5) can be solved by a transformation $a_n^\dagger \equiv U_{ki}^\dagger c_i^\dagger$, which allows us to rewrite H in diagonal form in the new operators:

$$H = \sum_k E_k a_k^\dagger a_k. \tag{1.6}$$

The new operators $a_k^\dagger$ are creation operators on the *single-particle orbitals* of the system, rather than on its sites. In three and higher dimensional systems, it turns out that, for strong enough disorder, the weight of these opeators on each site, given by U_{ki} for each single-particle orbital k on each site i, decay exponentially towards both sides of a particular orbital center. We say that the single-particle orbital is localized. Moreover, in one and two dimensional systems any amount of disorder localizes the single-particle orbitals. Furthermore, the single-particle eigenstates of H, which are generated by the creation of a particle with the single-particle orbital creation operators, also decay exponentially away from a localization center: $\phi_k \propto \exp\left\{\frac{|i-R_k|}{\xi}\right\}$, where ξ is the localization length of the eigenstate. This is in contrast with generic systems, which have eigenstates that are extended over the system.

Anderson localized states violate the ETH. Furthermore, the exponential decay of the widths of a single-particle wave function implies that, in the thermodynamic limit, a non-zero weight remains around the localization center. This implies that a state that is initialize with a particle in a site, then even at infite times it will preserve a non-zero probability of finding the particle in that site, keeping some memory of its initial conditions. Creating a many-body state in these systems does not change their phenomenology, due to the fact that particles do not interact, as a consequence of the Hamiltonian being quadratic [17].

1.2.2 Many-body localization

Comprehensive review in MBL can be found in Refs. [2, 5, 6, 56, 63]

Many-body localization (MBL) focuses on the study of localization on interacting systems. The field took flight with the work of Basko, Aleiner, and Altschuler in 2006 [11] and has been extensively studied in recent years. Surprisingly, the presence of interactions does not completetly destroy the phenomenon of localization. Furthermore, as opposed to single-particle localization, one-dimensional systems with weak disorder remain thermal, and localization only destabilizes the thermal phase at strong enough disorder.

The study of many-body localization has followed two complementary paths in the literature. Some works have focused on the dynamics of states, their equilibrarion (or lack thereof) when initialized out of equilibrium, as well as their spread of correlations across the system. Other works have studied the physics

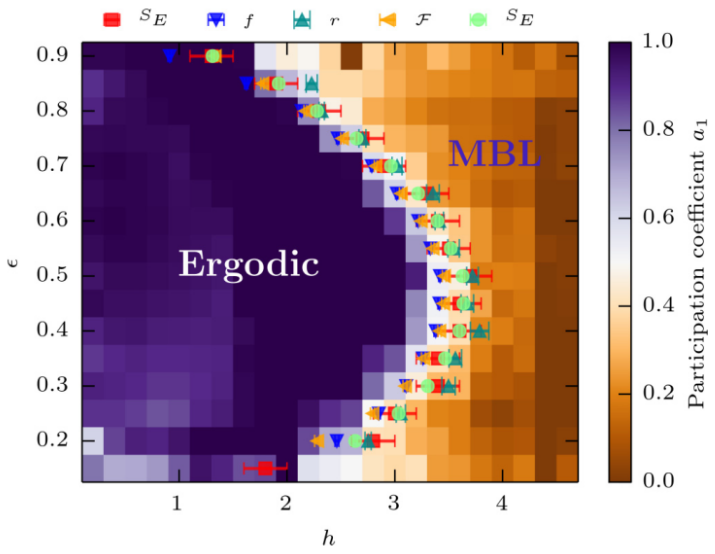

Figure 1.1: (From Ref. [59]) Phase diagram of the standard model of MBL in the $W - \epsilon$ plane, where W (h in the figure and in Ref. [59]) is the disorder strength and ϵ the energy density.

of eigenstates, their correlations, and whether they statisfy the ETH or not. In both cases, the body of work has tried to tackle the problem from both the numerical and the analytic point of view.

The sometimes called standard model of MBL has attracted substantial attention in the study of MBL. The numerical study of this model, which we introduce in the following section, has been the subject of my work.

The standard model of many-body localization

The most studied model that presents an ergodic-MBL transition is the sometimes called standard model of MBL, which in one dimension takes the form:

$$H = \frac{1}{4}\sum_{i=0}^{L-2} \vec{\sigma}_i \cdot \vec{\sigma}_{i+1} - \frac{1}{2}\sum_{i=0}^{L-1} h_i \sigma_i^z, \tag{1.7}$$

where the coefficients $\{h_i\}$ are random on-site magnetic fields sampled from the uniform distribution over the interval $[-W, W]$, and W is the disorder strength.

The model of Eq. (1.7) has been thoroughly studied in the literature [4, 8, 12, 14, 15, 30, 38, 44, 46, 54, 55, 57, 59, 60, 64, 67, 85, 106, 110]. The phase diagram of this model in the $W - \epsilon$ plane is shown in Fig. 1.1, where the disorder strength W is denoted by h, following the notation of Ref. [59]. ϵ represents the energy density

of an eigenstate, defined as:

$$\epsilon \equiv \frac{E - E_{min}}{E_{max} - E_{min}}, \tag{1.8}$$

where E is the energy of the eigenstate; the energy density ranges from 0 to 1. As we can see, the phase diagram presents a transitiong between the ergodic phase and the MBL phase at a critical disoder strength of $W_c \approx 3.7$ for $\epsilon = 0.5$. At lower and higher values of ϵ, the transition shifts towards lower values of W, defining a so-called mobility edge, which separates low-energy ergodic eigenstates from high-energy MBL eigenstates. At strong disorder all eigenstates of H are MBL; this region of the phase diagram is called the fully MBL (FMBL) region.

In one dimension, the standard model of MBL can be written, through a Jordan-Wigner transform, in terms of fermionic operators as follows:

$$\hat{H} = -\frac{t}{2}\sum_{i=0}^{L-2}\left(\hat{c}_i^\dagger \hat{c}_{i+1} + \hat{c}_{i+1}^\dagger \hat{c}_i\right) + V\sum_{i=0}^{L-2}\hat{n}_i\hat{n}_{i+1} + \sum_{i=0}^{L-1}\mu_i\hat{n}_i, \tag{1.9}$$

where $n_i = c_i^\dagger c_i$ are the occupation operators, and the chemical potentials $\{\mu_i\}$ play the role of the magnetic fields $\{h_i\}$ in the spin version of the model. For $t = V = 1$, this model corresponds exactly to the one in Eq. (1.7). Both the spin and the fermionic models appear often in the literature.

The model of Eq. (1.7) has total magnetization symmetry, which means that the operator $\sum_i \sigma_i^z$ commutes with H. Equivalently, the model of Eq. (1.9) has particle number symmetry, which means that the operator $\sum_i n_i$ commutes with H. This splits Hamiltonian in total magnetization (or total particle number) sectors that are independent of each other; each block of the Hamiltonian acts on independent regions of Hilbert space. This provides computational advantages to numerical studies, as discussed in Section 2.4; in practice, most studies focus on the zero-magnetization (half-filling) sector.

1.3 Characterization and phenomenology of many-body localization

There are several ways to distinguish MBL states from ergodic ones. In this section, we describe some of the more interesting characterizations of the MBL phase, as well as the phenomenology that comes with them. As mentioned above some aspects of MBL arise in the dynamics of systems initialized out of equilibrium, while other arise in the eigenstates themselves. In either case, we are interested in highly excited eigenstates,

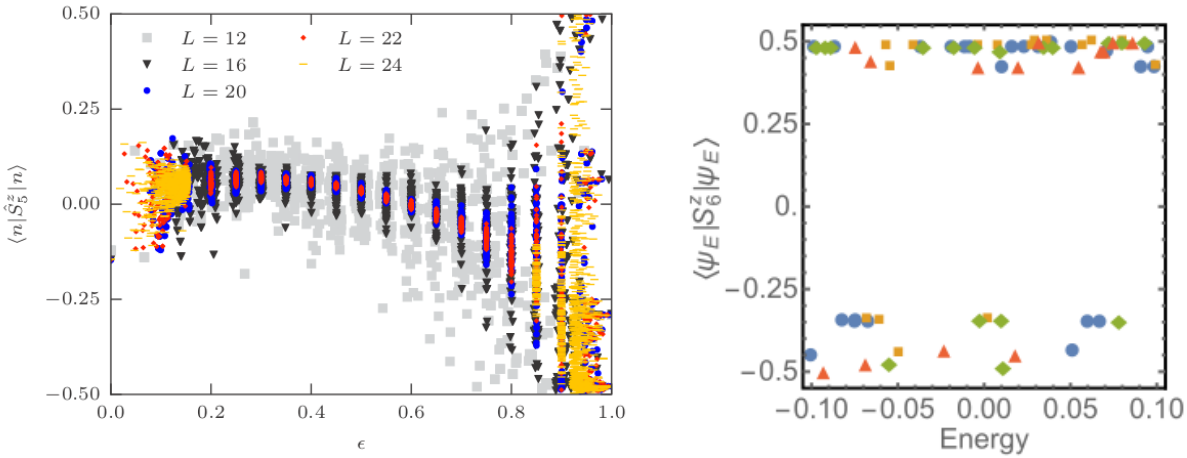

Figure 1.2: **Left:** (from Ref. [54]) Expectation value of S_5 as a function of energy density ϵ at weak disorder (ergodic phase). The local observable becomes a smooth function of ϵ with small fluctuations at the largest system size L. This is indicative of ETH being satisfied. The fact that ETH is satisfied only for intermediate values of ϵ shows phenomenology compatible with the presence of a mobility edge, outside of which the system is MBL. **Right:** (from Ref. [107]) Expectation value of S_6 over a small energy window close to the middle of the energy spectrum, for a system at strong disorder. We can see that the local observable considered does not follow a smooth function over contiguous energy eigenstates, but rather varies wildly. This behavior indicates that ETH is not satisfied.

which carry the dynamical properties of the system.

1.3.1 Local observables: ETH

A generic ergodic phase satisfies the ETH. This implies that the expectation value of local observables over eigenstates are smooth functions of the energy density of the eigenstate. Indeed, the fluctuations around this smooth function decrease quickly with system size, and vanish in the thermodynamic limit.

Fig. 1.2 shows the difference between ergodic and MBL eigenstates. In the ergodic phase, eigenstates that are contiguous in energy show similar expectation values over local observables, which are a smooth function of the energy density ϵ. On the contrary, an MBL system has eigenstates whose expectation values of a local observable vary wildly even when contiguous eigenstates over a small energy window are considered.

1.3.2 Scaling of the entanglement entropy

Given a system and a bipartition of it into two subsystems A and B, the correlations between them are quantified by the entanglement entropy, which is typically denoted by S_A. The entanglement entropy, which is formally defined as $S_A = -\operatorname{Tr}[\rho_A \log(\rho_A)]$, ranges from 0 to a maximum value of $\log_2(\dim(\mathcal{H}_A))\log(2)$, where $\mathcal{H}_A$ is the Hilbert space associated with subsystem A and we have assumed that $|A| < |B|$, *i.e.*, that A is smaller than its surroundings B. Since the dimension of the Hilbert space of A grows exponentially in

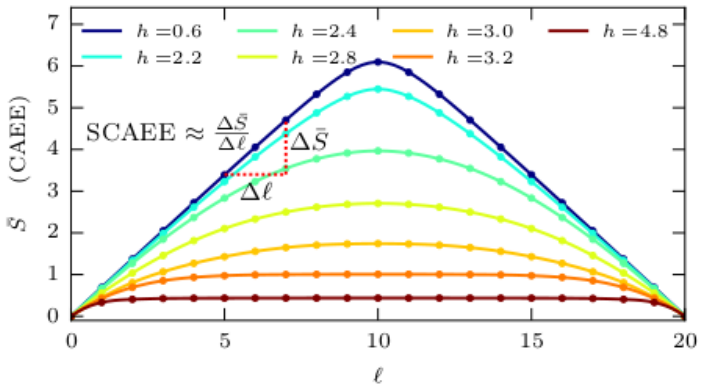

Figure 1.3: (From Ref. [106]) Cut averaged entanglement entropy (CAEE) of the smallest subsystem after a bipartition of a one-dimensional system. We can see that at small disorder strength the entanglement entropy scales with the size of the subsystem, *i.e.*, it grows linearly with subsystem size l, following a volume law of entanglement. At large disorder strength, the entanglement entropy is constant, regardless of subsystem size, and thus following an area law of entanglement.

$|A|$, then maximum value of S_A grows with the size of A.

One of the differences between ergodic and MBL eigenstates is the scaling of the entanglement entropy with the size of a subsystem. For ergodic eigenstates, $S_A \propto |A|$, *i.e.*, the entanglement entropy scales proportionally to its upper bound; we call this a *volume law* of entanglement, since S_A grows with the volume of A, $|A|$. MBL eigenstates, on the contrary, have an entanglement entropy that scales with the size of the area of subsystem A: $S_A \propto |\partial A|$; we call this an *area law* of entanglement. Area laws of entanglement are typical in non-critical ground states of local Hamiltonians; suprisingly, MBL highly excited eigenstates resemble ground states in this regard. In one dimension, this means that the entanglement entropy is constant. Both behaviors can be observed in Fig. 1.3.

While the entanglement entropy follows a volume law in the MBL phase and an area law in the ergodic phase, at the transition, the distribution of entanglement entropies becomes bimodal, suggesting the coexistence of large and small amounts of entanglement across different systems [106]. A similar idea has been used to estimate the position of the critical value of the disorder strength W_c, by identifying the value of W at which the standard deviation of the distribution of entanglement entropies is maximum [47].

It is also interesting to discuss the dynamical scaling of the entanglement entropy, *i.e.*, the growth of the entanglement entropy across a single cut as a state initialized out of equilibrium is evolved. In a typical setup, a one-dimensional spin chain is initialized in a product state over its spins. Then, this state is time evolved under the influennce of a disordered Hamiltonian, like that one of Eq. (1.7), and the entanglement entropy across the half cut is recorded. In generic, clean systems, the entanglement entropy grows linearly with time. At low disorder and ergodic behavior, the entanglement grows subballistically in time, *i.e.*, as a power law

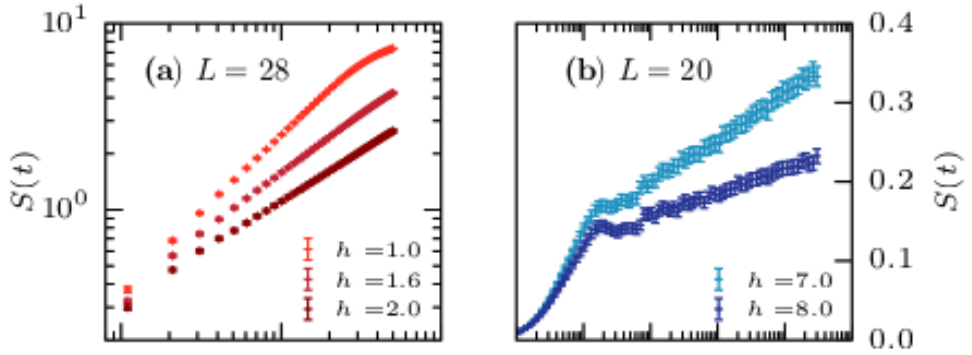

Figure 1.4: (From Ref. [60]) Growth in time of the entanglement entropy across half cut of a one-dimensional spin chain subject to the disordered Hamiltonian of Eq. (1.7) with disorder strength h after a product state initialization. In the ergodic phase (left), the entanglement grows as a power law in time t; at very low disorder, the growth is ballistic (linear in t), while it is subballistic closer to the MBL transition. In the MBL phase (right), the entanglement grows logarithmically in t.

with an exponent smaller than 1; at very weak disorder, the exponent approaches 1, thus recovering the ballistic (linear) growth. This is in contrast to the logarithmic growth shown by MBL dynamics at strong disorder.

1.3.3 Correlations

In Section 1.3.2 we discussed correlations from the point of view of the entanglement entropy. This focuses on the correlations across a cut of the system. Here, we pay attention to a different view of the spatial correlations across a system. In particular, it is interesting to consider the decay of correlations between small subregions of the system as these subsystems move further apart from each other. Although the behavior is universal for correlation functions of local observables, one convenient way to study correlations that is agnostic to the particular choice of correlation function is the quantum mutual information (QMI) between two non-overlapping subregions of the system. In particular, in the MBL phase the typical two-site QMI (QMI between sites i and j) decays exponentially as a function of the distance between the two sites. In the ergodic phase, this quantity decays slower than exponential.

1.3.4 Local integrals of motion: l-bits

One of the most suggestive phenomenological approaches to the MBL phase arises from the point of view of integrals of motion of the system [40, 71, 86]. In a region of the phase diagram where the Hamiltonian of Eq. (1.7) is fully MBL, *i.e.*, where all eigenstates of H are MBL, withouth the presence of a mobility edge, then we can find a complete set of *local* integrals of motion. The existence of an extensive set of local integrals of motion is not possible for a Hamiltonian in the ergodic side of the phase diagram.

Let us be more specific. Let us have the spin Hamiltonian H, which is diagonalized by a $\dim((H)) \times \dim((H))$ unitary matrix U. All operators

$$\tau_i^z \equiv U \sigma_i^z U^\dagger \tag{1.10}$$

is a binary operator that commutes with the H: $[H, \tau_i^z] = 0$. Furthermore, these operators commute with each other, $[\tau_i^z, \tau_j^z] = 0$, $\forall i, j$, since they inherit the commutation relations of the bare spin operators, $\{\sigma_i^z\}$. The operators $\{\tau_i^z\}$, which can be regarded as pseudo-spins, form a complete set of integrals of motion: by specifying a sequence of eigenvalues of all of these binary operators, we uniquely specify an eigenstate of H. This is similar to specifying configuration basis state by the specification of the expectation values of each operator σ_i^z over the state. Given a complete set of integrals of motion like those of Eq. (1.10), an eigenstate of H can therefore be regarded as a sequence of up and down pseudo-spins, which uniquely defines it.

While the above construction is valid for any spin Hamiltonian (and in a similar way for other kinds of systems), what is special about an MBL Hamiltonian is that there is a choice of a complete set of $\{\tau_i^z\}$ in which *all operators τ_i^z are local*. By this we mean that each τ_i^z is well approximated by an operator of finite support in the system; enlarging the support of the approximation only achieves exponentially small corrections to the approximation. In other words, the operators $\{\tau_i^z\}$, which are called local bits, or *l-bits*, have weight on each site that decreases exponentially fast away from its center i, in a manner that is reminiscent of the exponential decay of the weight of the single-particle orbitals of a non-interacting Anderson localized system (see Section 1.2.1).

The spin Hamiltonian H can be expanded in terms of $\{\tau_i^z\}$ as follows:

$$H = \sum_{i_0=0}^{L-1} f_{i_0}^{(1)} \tau_{i_0}^z + \sum_{i_0,i_1=0}^{L-1} f_{i_0 i_1}^{(2)} \tau_{i_0}^z \tau_{i_1}^z + \sum_{i_0,\ldots i_{L-1}=0}^{L-1} f_{i_0,\ldots i_{L-1}}^{(L)} \tau_{i_0}^z \ldots \tau_{i_{L-1}}^z. \tag{1.11}$$

The Hamiltonian is diagonal in the basis of pseudo-spins, which means that it can be written only in terms of the z component of the τ operators, without any off-diagonal term involving τ_i^x or τ_i^y. The fact that H is diagonal in the basis of l-bits comes at a price: H has to encode now many-body interaction terms, while only nearest-neighbor terms were present in the non-diagonal, real-space spin Hamiltonian of Eq. (1.7); the coupling constants of the Hamiltonian, $f_{i_0,\ldots i_{L-1}}^{(L)}$, encode the strength of the n-body interactions between different l-bits. However, as an empirical observation, the typical coupling constants decay exponentially fast with the range of the n pseudo-spins represent. The locality of the l-bit operators together with the locality of the interactions between l-bits, is in line with other observations of locality in the MBL phase.

Constructing a complete set of l-bits is not a well defined problem, in the sense that it does not have a

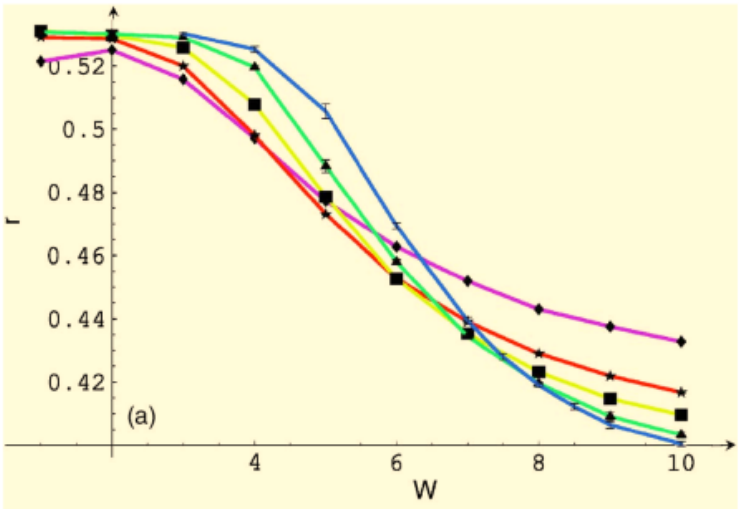

Figure 1.5: (From Ref. [64]) Disorder averaged level spacing ratios r of eigenstates in the middle of the spectrum as a function of disorder strength W, for systems of size $L = 8, 10, 12, 14, 16$. Deep in the MBL phase, r approaches $r \approx 0.39$, which is expected for Poisson level statistics. Deep in the ergodic phase, r approaches $r \approx 0.53$, characteristic of Gaussian Orthogonal Ensemble (GOE) statistics.

unique solution. In Section 2.3 we discuss a numerical method that gives good results and has been used to gain insight on the phsyics of the MBL phase and its transition.

1.3.5 Energy level statistics

The ergodic-MBL phase diagram can be studied from the point of view of random matrix theory. In MBL, level repulsion is very rare, giving rise to Poisson statistics. This is a consequence of the exponential decay of the coupling constants between distant l-bits, which give off-diagonal terms of the Hamiltonian between two eigenstates in perturbation theory that are exponentially smaller than the typical energy level spacings. Two states need to be extremely close in energy in order to experience level repulsion, and thus the typical situation for eigenstates is to be randomly distributed across the energy spectrum. In the ergodic phase, levels follow typical Gaussian Orthogonal Ensemble (GOE) statistics, which are a prototypical class of statistics that arise in random matrix theory.

In the literature, it has been common to study level spacing statistics by defining the consecutive level spacing ratio, r. Given the n^{th} eigenvalue of the Hamiltonian H, we denote by $\delta_{n,n+1}$ the energy difference between E_n and E_{n+1}; equivalently, the energy difference between E_n and E_{n-1} is denoted by $\delta_{n-1,n}$. The ratio between the largest and the smallest energy level spacings is r:

$$r \equiv \frac{\min(\delta_{n,n+1}, \delta_{n-1,n})}{\max(\delta_{n,n+1}, \delta_{n-1,n})}. \tag{1.12}$$

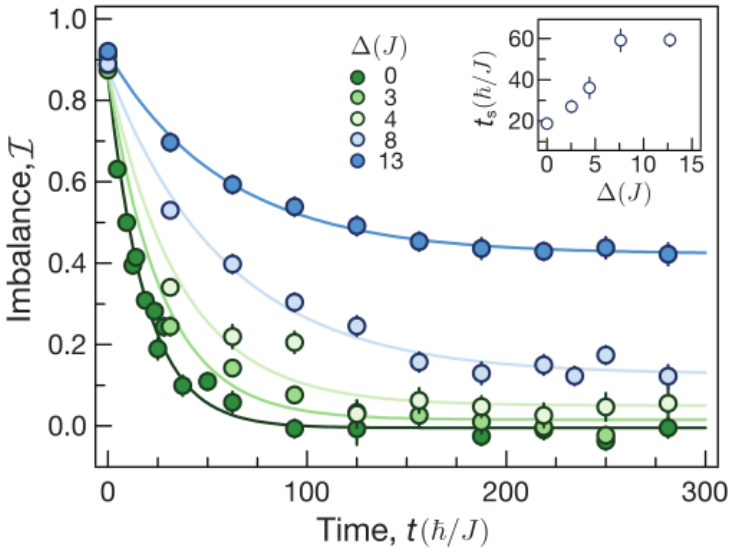

Figure 1.6: (From Ref. [25]) Disorder averaged evolution of the right and left atom number imbalance for a two-dimensional Bose-Hubbard Hamiltonian with on-site disorder with disorder strength Δ. At large disorder strength, the imbalance at large times remains finite, and the system retains memory of its initial conditions. At weak disorder, the imbalance vanishes.

The average level spacing ratio $\langle r \rangle$ (where the average is taken across disorder realizations and across eigenstates for each disorder realization) is often used to characterize level spacing statistics. In the MBL region of the phase diagram, $\langle r \rangle$ approaches 0.39, which is characteristic of Poisson statistics. Deep in the ergodic phase, $\langle r \rangle \approx 0.53$, which is characteristic of GOE statistics. At finite sizes, there is a crossover between both limiting values, which becomes sharper as the system size is increased. This quantity is usually used for finite-size scaling analyses, which lead to the estimation of the critical value of the disorder strength $W_c \approx 3.7$.

1.3.6 Experimental work

Although the study of the MBL has been largely focused on theoretical and numerical works, there have been experimental studies on the subject [18, 24, 25, 37, 48, 81, 84, 90] In general, the study of MBL has relied strongly on numerical works. However, the difficulty of simulating large-scale quantum systems is a burden typically found by these studies, whose conclusions are subject to scrutiny due to the small system sizes analyzed. In that regard, experimental simulations of MBL and ergodic systems over several quantum simulation platforms are preferable. On the other hand, these analog simulations are typically subject to large levels of noise.

In experiments related to MBL, a typical quantity of interest that can be measured is the spin, charge,

or atom number imbalance. In the case of Ref. [25], a two-dimensional optical lattice of bosons is initialized with all atoms on the left half of the system. As the system evolves, atoms diffuse to the right half. The left (N_L) and right (N_R) atom number imbalance is defined as $I = (N_L - N_R)/(N_L + N_R)$. In an ergodic system, the imbalance quickly drops to zero, since on average atoms disperes evenly over the lattice. In an MBL system, the imbalance is non-zero even at lont times, $t \to \infty$. This can be seen in Fig. 1.6.

1.4 Open questions

Despite the large body of work devoted to MBL in recent years, there are several questions around the MBL phase and its transition that remain open. Some of them are related to the ergodic-MBL transition, its mechanisms and its nature. Others are related to the MBL phase itself and its stability, both in one [1,68,93] and higher dimensions [3, 21, 28, 29, 58, 76, 77]. Here we mention a few of the questions that remain totally or partially unanswered.

First, the question of the existence of a mobility edge is not settled. Numerical studies consistently find a mobility edge, implying that, at intermediate disorder strengths, there is coexistence of ergodic and MBL, which are separated in energy. However, the mechanism that gives rise to this phenomenon is not known. Furthermore, it is sometimes argued that the mobility edge is seen on small systems, which numerical studies have access to, but should not survive in the thermodynamic limit [27]. Our own work maps out a mobility edge out to systems of size $L = 64$ [97], which is much larger than previous exact diagonalization studies, limited to sizes $L \lessapprox 24$.

While the existence of a complete set of local integrals of motion in a fully MBL system well characterizes that region of the phase diagram, an extension of this framework as we cross the transition into the ergodic phase is not known. On the one hand, it is clear that in the ergodic phase there is no complete set of local integrals of motion. On the other hand, it is unclear whether these integrals of motion should delocalize progressively as they undergo the transition, or they should do so in a discrete manner. Furthermore, in a region of the phase diagram with a mobility edge, what would be the role of the integrals of motion? Does the coexistence of local and extended integrals of motion give rise to the mobility edge?

Another subject that remains obscure is the relation between rare regions, resonances and the mechanism behind the ergodic-MBL transition. Close to the transition, statistical fluctuations of the disorder strength of subsystems can lead to the coexistence of ergodic bubbles in an otherwise MBL system, and vice versa. Resonances refer to the appearance of highly entangled subsystems that are far apart from each other in an otherwise MBL system. The study of both resonances and rare regions might be key in understanding

the critical properties of the system at the transition, as well as the mechanism driving the meltdown of the MBL phase.

To date, a few renormalization group studies have aimed at tackling the question of rare regions and resonances from a phenomenological point of view [69, 78, 100, 101, 108]. These studies allow to derive critical properties at the transition, as well as properties of the limiting ergodic and non-ergodic phases. For example, Ref. [101] finds subdiffusive transport in the ergodic vicinity of the transition. On the other hand, the authors of Ref. [78] can identify the presence of a resonating "backbone" that percolates across either the full system or a subsystem, thus flowing towards the ergodic or non-ergodic phase, respectively. While these studies shine light on the nature of the transition, they are phenomenological, and thus ignore the microscopic details of any MBL model. Observing critical properties, as well grasping the concepts of rare regions and resonances from a microscopic point of view remains a challenging and largely open question. Our own works aim at tackling this problem numerically. As was the case with the mobilidy edge, one of the main burdens in analyzing the transition resides in the difficulty to scale up the system sizes studied; while there are efficient algorithms to study the MBL phase over large systems, close to the transition one relies on exact diagonalization, which can only scale up to systems of size $L \lessapprox 24$.

Most studies on MBL have focused on one-dimensional systems. The existence of MBL in two (and higher) dimensions is controversial. On the one hand, experimental studies are compatible with the existence of MBL in two dimensions [18, 25]. Also numerical studies have given promising results, pointing towards that direction [42,102] However, analytical arguments suggest that the MBL phase is unstable in dimensions higher than one [3, 21, 28, 29, 58, 76, 77].

Chapter 2

Methods

Our studies of the ergodic-MBL phase diagram are focused on the analysis of highly excited eigenstates of the Hamiltonian of Eq. (1.7), which includes the study of their correlations across the system, as well as on sets of conserved quantities, which are local in MBL and extended in the ergodic phase. In this chapter we describe the tools used to numerically access these quantities, essential to our work.

2.1 Entanglement entropy

Given a bipartition of a system into two subsystems, the entanglement entropy between them is a measure the amount of correlations crossing that cut, hence "entangling" both subsystems. More precisely, if a closed system is in a pure state $|\psi\rangle$ and we bipartition the system in subsystems A and B, we can rewrite $|\psi\rangle$ as:

$$|\psi\rangle = \sum_{\alpha,\beta}^{N_A,N_B} c_{\alpha\beta} \, |\alpha\rangle_A \otimes |\beta\rangle_B \,, \tag{2.1}$$

where N_A and N_B are the dimensions of the Hilbert space of subsystem A and B respectively, and $\{|\alpha\rangle_A\}$ and $\{|\beta\rangle_B\}$ are complete bases of A and B, respectively. The singular value decomposition (SVD or Schmidt decomposition) of matrix $c_{\alpha\beta}$ yields $c_{\alpha\beta} = \sum_{\gamma}^{N_{\text{bond}}} U_{\alpha\gamma}\lambda_{\gamma\gamma}V^{\dagger}_{\gamma\beta}$, where N_{bond} is in general equal to the smallest of N_A and N_B (for us, $N_A < N_B$ due to $|A| < |B|$), $\lambda_{\gamma\gamma}$, or simply λ_γ is a diagonal matrix of real and positive values, and $U^{\dagger}U = V^{\dagger}V = \mathbb{1}_{N_{\text{bond}}}$. This transformation allows us to rewrite Eq. (2.1) as:

$$|\psi\rangle = \sum_{\gamma}^{N_{\text{bond}}} \lambda_\gamma \, |\gamma\rangle_A \otimes |\gamma\rangle_B \,, \tag{2.2}$$

where the sum is now a single sum, and from which it is easy to read that each state in the basis of $\{|\gamma\rangle_A\}$ comes paired with each state in the basis of $\{|\gamma\rangle_B\}$, making manifest the structure of correlations. Due to normalization, $\sum_{\gamma}^{N_{\text{bond}}} \lambda_\gamma^2 = 1$. The entanglement entropy of ψ over the bipartition into A and B is defined

as:

$$S_A = -\sum_{\gamma}^{N_{\text{bond}}} \lambda^2 \log(\lambda), \tag{2.3}$$

where the notation with a single subindex A means that we are computing the entanglement entropy between A and its surroundings, *i.e.*, between A and B; unsurprisingly, the entanglement entropy S_B would be exactly equal to S_A.

The entanglement entropy S_A ranges from 0 to $N_{\text{bond}} \log(2) = \min(N_A, N_B) \log(2)$. It is convenient to order the singular values λ_γ in descending order. The flatter the decay of λ_γ, the larger the entanglement entropy; in that case the state $|\psi\rangle$ is "encoded" across the bipartition over many pairs of basis states across A and B. If the entanglement singular values $\{\lambda_\gamma\}$ decay sharply, then the state $|\psi\rangle$ can be well approximated with the first few most contributing pairs $\lambda_\gamma |\gamma\rangle_A \otimes |\gamma\rangle_B$; as a result, the entanglement entropy S_A is small. As an example, let us consider a Bell pair prepared over two spins:

$$|\psi\rangle_{\text{Bell}} = \frac{1}{\sqrt{2}} \left(|\uparrow\downarrow\rangle + |\downarrow\uparrow\rangle\right). \tag{2.4}$$

In this case, $|\psi\rangle_{\text{bell}}$ is already written in decomposed form over a bipartition of the system into site 1 (A) and site 2 (B), with $\lambda_1 = \lambda_2 = \frac{1}{\sqrt{2}}$. The entanglement entropy is equal to $S_A = \log(2)$ and we say that there is a single *bit* of entanglement across the system.

Sometimes, the dimension of the common index γ, N_{bond}, is smaller than $\min(N_A, N_B)$. By this we mean that $|\psi\rangle$ can be well appoximated by a few N_{bond} largest contributing pairs with entanglement singular values λ_γ. Performing this truncation, which allows us to enconde good approximations of wave functions, $|\psi\rangle$, which much less memory resources, is often called "compression". Compression by shrinking the bond dimension across cuts of a system is a central concept in the field of tensor networks and, in particular, in the use of matrix product states, which we discuss in Section 2.2.2.

Finally, the entanglement entropy is often defined in terms of the reduced density matrix of a subsystem A, ρ_A, as $S_A = -[\rho_A \log(\rho_A)]$. Both definitions are equivalent, and their connection lays on the eigenvalues of the ρ_A, which are equal to the entanglement singular values squared, λ_γ^2.

2.2 Obtaining highly excited eigenstates

As opposed to typical quantum mechanical studies on condensed matter systems, in the MBL problem we are not concerned with the ground state of the Hamiltonian, but rather with its highly excited eigenstates.

In particular, a Hamiltonian H defined on a finite-dimensional Hilbert space has a ground state of energy $E_{\min}$ and an anti ground state of energy $E_{\max}$, which are the lowest and highest energy eigenstates of H, respectively. Any eigenstate of energy E is said to have an energy density equal to $\epsilon \equiv (E - E_{\min})/(E_{\max} - E_{\min})$, *i.e.*, the energy density is normalized between 0 and 1. Most of the time we will be interested in eigenstates at an energy density of 0.5, *i.e.*, right in the middle of the spectrum, although we will also look at other values of the energy density, for which the eigenstate properties might differ and the ergodic-MBL phase transition point might change due to the existence of a mobility edge. In this section we describe the two methods used: exact diagonalization, which is used on small systems, and SIMPS, a matrix product state method used for larger systems.

2.2.1 Exact diagonalization

As its name suggests, the basic idea behind exact diagonalization (ED) is numerically diagonalizing the Hamiltonian matrix, H. This explicitly gives us all eigenenergies and eigenvectors (eigenstates) of H, with the clear advantage of providing exact answers, up to machine precision. The large disadvantage of this method is its poor scalability. Both memory and time resources of ED scale exponentially with system size, thus restricting ourselves to relatively small systems.

To understand this exponential scaling, an example is illustrative. Let us define a Hamiltonian H over a spin lattice with L sites. The local Hilbert space of each site (each spin) has dimension 2, and the global Hilbert space of the entire system is the outer product of all local Hilbert spaces, and thus has dimension 2^L. The Hamiltonian matrix has therefore size $2^L \times 2^L$, and we will have 2^L eigenstates of 2^L entries each, which implies an exponential scaling in the memory resources needed to store both H and its eigenstates. The time complexity of diagonalization is polynomial in the dimension of the matrix [1] , and scales therefore exponentially in L as well.

It is rarely the case that we are interested in all eigenstates of H. In condensed matter we are very often interested in the ground state of H, and in MBL we are interested in a single or a few highly excited eigenstates of H. In those cases, the Lanczos algorithm and its variants lets us speed up the computation of the eigenstate we target, with the caveat that we do not compute an extensive number of eigenstates of H.

Ground state Lanczos

The Lanczos algorithm for the computation of the ground state $|GS\rangle$ of a Hermitian matrix H aims at solving an eigenvalue problem over a small subspace of Hilbert space, which by construction contains $|\psi_0\rangle$

[1] Matrix diagonalization has the same complexity as matrix multiplication, which scales as $\mathcal{O}(n^3)$ for a matrix of size $n \times n$.

to high precision. The subspace at hand is the so-called *Krylov* subspace, which is spanned by the vectors obtained by applying H iteratively to a randomly chosen initial state $|\psi_0\rangle$:

$$K^m \equiv \text{span}\{|\psi_0\rangle, H|\psi_0\rangle, H^2|\psi_0\rangle, \ldots, H^m|\psi_0\rangle\},$$

which has dimension $m+1$, where m is a hyper-parameter.

The rationale behind why the Krylov subspace contains $|GS\rangle$ to high accuracy is that applying H to a state (*e.g.*, ψ_0) enhances the components of $|\psi_0\rangle$ along eigenstates with eigenvalues of large magnitude. Applying H iteratively, we are spanning a subspace that contains $|GS\rangle$ to higher and higher accuracy. This includes both low and high laying eigenstates of H, if their eigenvalues are negative and positive, respectively. In the case that the spectrum of H is strictly positive, shifting H by a constant would lead us to the desired results. We can now obtaine $|GS\rangle$ by diagonalizing H projected onto the m-dimensional Krylov subspace a looking for the ground state of this smaller eigenvalue problem.

Correctly applying the Lanczos method involves paying attention to several numerical considerations. First, it is desirable to orthonormalize the Krylov subspace as it is built; diagonalization procedures are more efficient and stable when applied over orthonormal bases. We do so by applying Gram-Schmidt orthonormalization as we build the Krylov subspace. For each iteration n, with $n = 1, \ldots, m$:

1. Compute $\left|\tilde{\psi_n}\right\rangle = H|\psi_{n-1}\rangle - \sum_{n'}^{n-1} |\psi_{n'}\rangle \langle\psi_{n'}| H|\psi_{n-1}\rangle$, which has magnitude $\left|\left|\tilde{\psi_n}\right\rangle\right| = \beta_n$.
2. Normalize $|\psi_n\rangle = \frac{|\tilde{\psi_n}\rangle}{\beta_n}$.

It is easy to realize that following this procedure we iteratively build vectors $H|\psi_{n-1}\rangle$ which are automatically orthogonal to all previously obtained Krylov basis vectors, but $|\psi_{n-1}\rangle$. For this reason, we can simplify each iteration and rewrite it as:

1. Compute $\left|\tilde{\psi_n}\right\rangle = H|\psi_{n-1}\rangle - |\psi_{n-1}\rangle \langle\psi_{n-1}| H|\psi_{n-1}\rangle$, which has magnitude $\left|\left|\tilde{\psi_n}\right\rangle\right| = \beta_n$.
2. Normalize $|\psi_n\rangle = \frac{|\tilde{\psi_n}\rangle}{\beta_n}$.

One consequence of this is that H projected onto the Krylov subbasis constructed this way is tridiagonal, *i.e.*, only $\langle\psi_n| H|\psi_n\rangle = \alpha_n$ and $\langle\psi_n| H|\psi_{n-1}\rangle = \langle\psi_{n-1}| H|\psi_n\rangle^*$ are non-zero. In fact, $\langle\psi_n| H|\psi_{n-1}\rangle = \beta_n$,

which is real and positive, and H projected onto K^m is simply:

$$H_{K^m} = \begin{pmatrix} \alpha_0 & \beta_1 & 0 & \dots & 0 & 0 \\ \beta_1 & \alpha_1 & \beta_2 & \dots & 0 & 0 \\ 0 & \beta_2 & \alpha_2 & \dots & 0 & 0 \\ 0 & 0 & 0 & \ddots & 0 & 0 \\ 0 & 0 & \vdots & 0 & \alpha_{m-1} & \beta_{m-1} \\ 0 & 0 & \vdots & 0 & \beta_{m-1} & \alpha_m \end{pmatrix}, \tag{2.5}$$

which is a symmetric, real, tridiagonal, $(m+1)\times(m+1)$ matrix. If we are interested only on the eigenvalue of $|GS\rangle$, we only need to keep track of $|\psi_n\rangle$ and $|\psi_{n-1}\rangle$ at each step. If we are interested in the eigenstate as well, then we need to keep track of every vector in the basis. The time complexity of the Lanczos algorithm scales as $\mathcal{O}(n^2)$.

In practice, the Lanczos method as presented here is numerically unstable. The reason for this is that, as we iteratively build K^n by applying H^n to $|\psi_0\rangle$, K^n becomes approximately an invariant subspace under the action of H. This means that with realistic machine precision, $H|\psi_n\rangle$ is almost entirely contained in K^n. Under those circumstances, β_{n+1} is very close to 0, which in turn results in $\left|\tilde{\psi_{n+1}}\right\rangle$ not really being orthogonal to the rest of the elements in the basis, which was a key assumption of our construction. Solutions that make Lanczos numerically stable work in three complementary directions: (1) explicitly orthogonalizing $|\psi_{n+1}\rangle$ against more than just the previous iteration vector, thus preserving orthogonality; (2) often fully orthogonalizing the basis, thus recovering orthogonality; (3) removing poorly orthogonalized basis states by restarting Lanczos often from an already good approximation of $|GS\rangle$.

Highly-excited eigenstates with Lanczos

In MBL, we need to obtain highly-excited eigenstates of H close to energy E, rather than $|GS\rangle$. Formally, we can achieve this by applying Lanczos to the shifted and inverted Hamiltonian $\tilde{H}_{SI} = (H-E)^{-1}$; the eigenvectors of $\tilde{H}_{SI}$ are the same as those of H, while the eigenvalues of those eigenstates that lay close to E and were interior eigenvalues of H are now extremal eigenvalues $\tilde{H}_{SI}$. However, while shifting the matrix H by E is trivial, inverting the matrix $(H-E)$ is numerically very expensive. In practice, we do not need to invert the full matrix $(H-E)$, but rather just be able to apply $(H-E)^{-1}$ to $|\psi_n\rangle$ at each step of the iteration. This can be done by solving the following linear system of equations:

$$(H-E)\left|\tilde{\psi}_{n+1}\right\rangle = |\psi_n\rangle\,. \tag{2.6}$$

The complexity of the shift-and-invert Lanczos method is dominated this step, which scales as with $\dim(\mathcal{H})^3$, where $\dim(\mathcal{H})$ is the dimension of the Hilbert space, *i.e.*, the size of the vectors $|\psi_n\rangle$. Obtaining highly-excited eigenstates is thus much more expensive than obtaining ground states with the Lanczos method.

Numerically stable implementations of the ground state Lanczos as well as the shift-and-invert Lanczos can be found in several linear algebra packages. We make extensive use of the `scipy.sparse.linalg.eigsh` function in `python`, which ultimately makes use of ARPACK routines [50, 98].

2.2.2 Using matrix product states for large systems: DMRG and SIMPS

Exact diagonalization techniques are limited to small systems, given the exponential scaling with system size of the amount of resources needed. For certain problems in condensed matter, tensor networks provide a powerful framework that lets us scale up the size of the systems we can study; in some cases, they even provide algorithms whose time and memory requirements scale polynomially with system size. One such problem is obtaining ground states of gapped, local Hamiltonians in one dimension. This is done through the use of a subclass of tensor networks called matrix product states (MPS) and the so-called density matrix renormalization algorithm (DMRG) [104, 105]. As we will discuss, MPSs can be leveraged to obtain highly excited eigenstates of MBL Hamiltonians through a DMRG-like algorithm [107].

Refs. [16, 65, 66] are excellent reviews on tensor networks. For an in-depth review of MPSs and their algorithms, including DMRG, see Ref. [83].

Matrix product states formalism

As a first approach, matrix product states (MPS) provide an alternative way to represent many body wavefunctions, which is convenient in one-dimensional systems. For convenience, lets restrict ourselves to spin-$\frac{1}{2}$ wave functions. A generic wave function defined on a system of L spins $(\sigma_1, \ldots, \sigma_L)$ a system has vector entries:

$$|\psi\rangle = \sum_{\sigma_1,\ldots\sigma_L} c_{\sigma_1,\ldots,\sigma_L} |\sigma_1, \ldots, \sigma_L\rangle \tag{2.7}$$

over the basis of spin configurations. As we can see, all information of the wave function is encoded in tensor c, which has L binary indices, one per spin (with possible values $\uparrow$ and $\downarrow$); we call this a rank-L tensor c. A

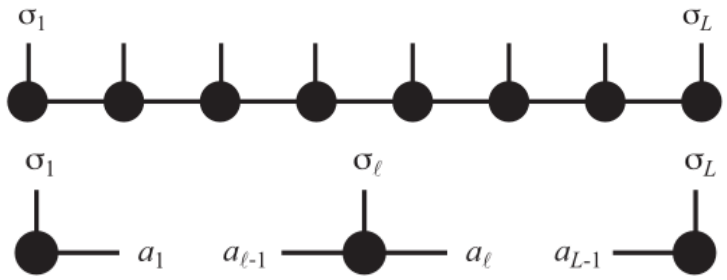

Figure 2.1: (From Ref. [83]) **Top:** pictorial representation of an MPS. **Bottom:** physical and virtual indices of an MPS.

MPS encoding of this wave-function would look like:

$$|\psi\rangle = \sum_{\sigma_1,\sigma_2,\ldots\sigma_L} \left(\sum_{a_1,a_2,\ldots,a_{L-1}}^{B_1,B_2,\ldots,B_L} M^1_{\sigma_1;a_1} M^2_{\sigma_2;a_1,a_2} M^3_{\sigma_3;a_2,a_3} \ldots M^L_{\sigma_L;a_{L-1}} \right) |\sigma_1,\ldots,\sigma_L\rangle\,, \tag{2.8}$$

where, for each configuration $\{\sigma_1,\ldots\sigma_L\}$ the entries of the tensor c, $c_{\sigma_1,\ldots,\sigma_L}$, can be computed as the product of matrices $\sum_{a_1,a_2,\ldots,a_{L-1}}^{B_1,B_2,\ldots,B_L} M^1_{\sigma_1;a_1} M^2_{\sigma_2;a_1,a_2} M^3_{\sigma_3;a_2,a_3} \ldots M^L_{\sigma_L;a_{L-1}}$. Note that each M^i is a tensor of rank 3, which becomes a matrix (or a vector for the left and right tensors, M^1 and M^L) once σ_i is fixed. The dimension of the indices σ_i is 2, which means that, as mentioned above, it can only take two values. However, the dimension of the a_i indices, which are shared between tensors, is B_i, which so far has not been determined, and which we call the bond dimension between site i and $i+1$. Note that Eq. (2.8) can always be satisfied, *i.e.*, we can find tensors $\{M^i\}$ such that the product of these matrices is equal to $c_{\sigma_1,\ldots,\sigma_L}$ for all spin configurations; we just have to allow the bond dimensions to be large enough, in which case we have enough freedom to fit the parameters properly. It would though be a challenge to encode (maybe approximately) the wavefunction $|\psi\rangle$, with 2^L entries, with tensors $\{M^i\}$ of small bond dimension, *e.g.* upperbounded by some value. We will elaborate on this idea later.

Let us now introduce some convenient notation for the tensor network presented in Eq. (2.8), *i.e.*, the MPS representation of $|\psi\rangle$. As we can see in Fig. 2.1, we pictorially represent all tensors $\{M^i\}$ as nodes in a graph, and their indices as edges of the graph. When indices are connected to two nodes, we mean that the sum over all possible values of that index (edge) is considered, *e.g.*, the sum $\sum_{a_1}^{B_1}$. Summing over an index is often called *contracting* the index, and summing over all indices on a tensor network is referred to as *contracting* the tensor network. The spin indices $\{\sigma_i\}$ are called *physical* indices, and correspond to the physical degrees of freedom of the system. The bond indices $\{a_i\}$ are called *virtual* indices. With this notation in mind we can represent more complicated quantities, such as $\langle\psi|\psi\rangle$ (which sums over all phsyical indices) or the computation of the matrix element $\langle\phi|\, O^i O^j\, |\psi\rangle$, as is represented in Fig. 2.2. In

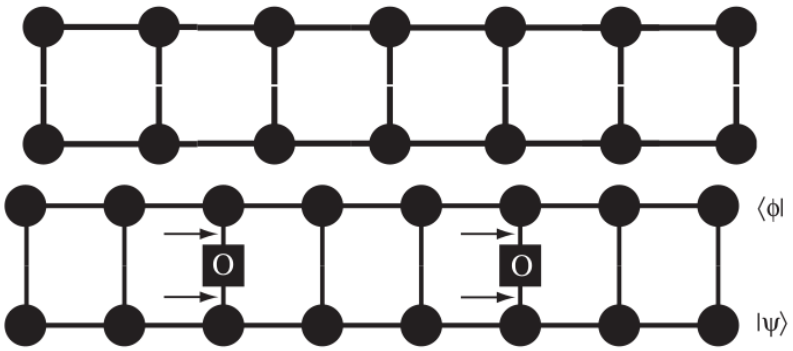

Figure 2.2: (From Ref. [83]) **Top:** pictorial representation of $\langle\psi|\psi\rangle$. The top MPS represents $\langle\psi|$, which is being contracted with the bottom MPS, $|\psi\rangle$. **Bottom:** computation of $\langle\phi|\, O^i O^j \,|\psi\rangle$. The two operators O over sites i are rank-2 tensors with indices $\{i, i'\}$ and $\{j, j'\}$, respectively.

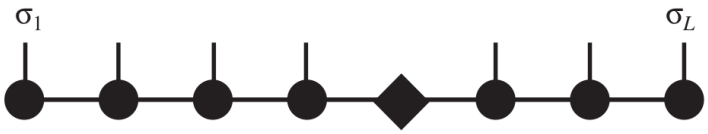

Figure 2.3: (From Ref. [83]) Result of applying an SVD ($T = U\lambda V^\dagger$) to a two-site tensor T^l in between sites l and $l+1$. The diamond tensor represents the diagonal matrix λ, while the tensor U ($V^\dagger$) is on site l (resp. $l+1$). We usually absorb (contract) the tensor λ with either of its contiguous tensors. Some authors contract $\sqrt{\lambda}$ with both the left and right contiguous tensors contiguous to λ.

both cases, the entries of the tensors of the upper MPS have been conjugated, so the product $\langle\psi|\psi\rangle$ is correctly computed. In the latter case, the one-site operators O^i and O^j each have two indices, *i.e.*, $O^i_{\sigma_i,\sigma_{i'}}$, as is represented through edges in the figure.

Compression, canonization, entanglement entropy, and contraction complexity

There is some gauge freedom in the choice of tensors in an MPS that we will exploit very often. Let us consider two consecutive tensors of the MPS, M^l and M^{l+1}, and contract them together into a single tensor T:

$$M^l_{\sigma_l;a_{l-1},a_l} M^{l+1}_{\sigma_{l+1};a_l,a_{l+1}} = T_{\sigma_l,\sigma_{l+1};a_{l-1},a_{l+1}}.$$

We can now factorize T into two tensors by:

1. Writing it explicitly as a matrix: $T_{\sigma_l,a_{l-1};\sigma_{l+1},a_{l+1}}$, where the tuple (σ_l, a_{l-1}) for a *superindex* of dimension $2 \times B_{l-1}$ and the tuple (σ_{l+1}, a_{l+1}) form a superindex of dimension $2 \times B_{l+1}$.

2. Performing a singular value decomposition (SVD) on T: $T_{\sigma_l,a_{l-1};\sigma_{l+1},a_{l+1}} = U_{\sigma_l,a_{l-1};\alpha}\lambda_{\alpha,\alpha'}V^\dagger_{\alpha';\sigma_{l+1},a_{l+1}}$, where λ is a positive semi-definite diagonal matrix.

3. Contracting U with λ into $\tilde{M}^l$, $\tilde{M}^l_{\sigma_l,a_{l-1};\alpha'} = U_{\sigma_l,a_{l-1};\alpha}\lambda_{\alpha,\alpha'}$.

4. (For convenience) Renaming $\tilde{M}^{l+1}_{\alpha';\sigma_{l+1},a_{l+1}} \equiv V^\dagger_{\alpha';\sigma_{l+1},a_{l+1}}$

5. (For convenience) Renaming index $\tilde{a}_l \equiv \alpha'$.

6. (For convenience) Reordering the indices of $\tilde{M}^l$ and $\tilde{M}^{l+1}$ to the standard form $M^l_{\sigma_l;a_{l-1},\tilde{a}_l}$ and $M^{l+1}_{\sigma_{l+1};\tilde{a}_l,a_{l+1}}$.

The new pair of tensors, $\tilde{M}^l$ and $\tilde{M}^{l+1}$, is different from the original M^l and M^{l+1}, in the sense that their entries are different, but the pairs are completely interchangeable, *i.e.*, they contract to the same result, T There is however a subtle but crucial difference between both pairs of tensors: the dimension of index $\tilde{a}_l$, $B_{\tilde{a}_l}$, could be different from the dimension of index a_l, B_{a_l}. In particular, $B_{\tilde{a}_l}$ is at most $\min(2 \times B_{l-1}, 2 \times B_{l+1})$, but it could even be lower if the SVD finds singular values (the values λ_α of the diagonal matrix λ) that are 0. Most interestingly, if the singular values decay fast enough, we can keep just the χ largest, thus imposing a cutoff in the bond dimension $B_{\tilde{a}_l}$, which would allow us to aggresively *compress* the MPS while still keeping a good approximation of it.

There is a series of questions that might arise from the definition of this process. Is the approximation made by the compression procedure controllable? What is the relation between the singular values of this SVD and the entanglement entropy discussed in Section 2.1? Is compression achievable for MPSs describing physical wave functions? We answer these questions in the remaining of this section.

By applying the compression procedure above (for simplicity, lets apply it in an exact way, without any approximation) to the right-most pair of tensors on an MPS, M^{L-1} and M^L, we guarantee that $\tilde{M}^L$ contracted with $\tilde{M}^{L*}$ through index σ_L becomes the identity matrix, *i.e.*, $\tilde{M}^L_{\sigma_L;\tilde{a}_L}\tilde{M}^{L*}_{\sigma_L;\tilde{a}'_L} = \mathbb{1}_{\tilde{a}_L,\tilde{a}'_L} = \delta_{\tilde{a}_L,\tilde{a}'_L}$, which is a consequence of $V^\dagger V = \mathbb{1}$. We can now apply the same procedure to the pair of tensors M^{L-1} and M^{L-2}, with similar consequences. We can cascade the procedure from right to left, applying it to every contiguous pair of tensors all the way down to M^1, M^2. The MPS is now in what is known as a *right canonical form*. The contraction of $\langle\psi|\psi\rangle$ is now trivial: we know that the right-most tensor of $\langle\psi|$ contracts with the right-most tensor of $|\psi\rangle$ (see top panel of Fig. 2.2) into the identity; after this contraction, we can contract the next pair of tensors into the identity as well; we can continue to do so trivially. At an arbitrary point during this contraction, the tensors on l look like the top panel of Fig. 2.4, *i.e.*, M^l (we have dropped the notation $\tilde{M}$ for simplicity) has only $\delta a_l, a'_l$ matrix to its left, which is represented by a single edge, since both indexes are really the same one once they are forced to agree. A similar procedure can give rise to the *left canonical form* of the MPS (bottom panel of Fig. 2.4). Equivalently, if we canonize the MPS from the right up to site $l+1$ and from the left up to site l, then we say that the MPS is in its *mixed canonical*

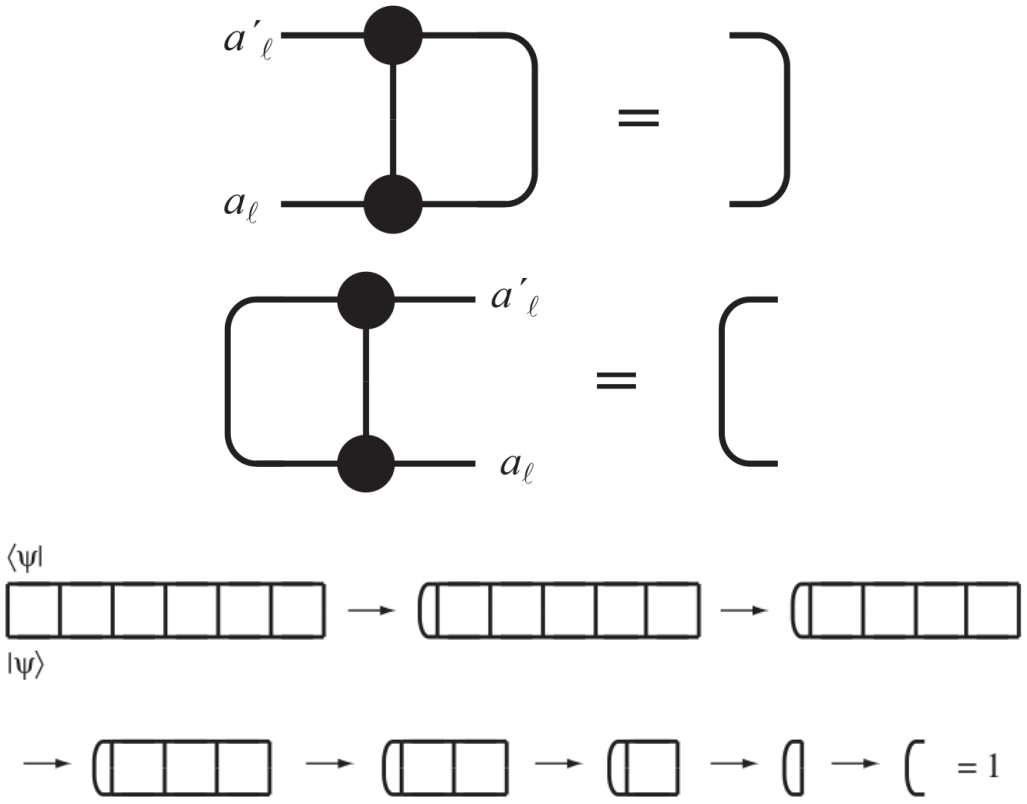

Figure 2.4: (From Ref. [83]) **Top:** intermediate step in the right canonization of an MPS. The index to the right of the tensor at site l becomes trivially connected to an identity operator when contracting $\langle\psi|\psi\rangle$. **Middle:** same as the top panel, but for a left canonization. **Bottom:** full contraction procedure of $\langle\psi|\psi\rangle$ for a left canonical MPS.

form between sites l and $l+1$. The full contraction of $\langle\psi|\psi\rangle$ can be seen pictorially in the bottom panel of Fig. 2.4.

Beyond the fact that an MPS contracts trivially with itself when it is in a canonical form, the importance of the mixed canonical form is that, if we compress an MPS between sites l and $l+1$ while it is canonized around that pair of sites, then the approximation we are taking by throwing away small singular values is guaranteed to be the best possible, given the χ cutoff we are employing to truncate the bond dimension between that pair of sites. On the contrary, if we compress an MPS between an arbitrary pair of sites without canonizing it first around that pair of sites, then our approximation is not optimal for that particular bond dimension cutoff χ. Interestingly, the singular values drawn from the compression procedure are exactly the Schmidt singular values of Section 2.1, *i.e.*, the values λ_α are the same for both sections. Moreover, the magnitude of the error we make by approximating the MPS (in this compression step) is equal to $1-\sum_\alpha^\chi \lambda_\alpha^2$, which makes the approximation controllable.

The fact that the singular values squared read from the (properly canonized) MPS are exactly equal

to the entanglement singular values, λ_α^2 has an intriguing implication: the bond dimension of an MPS is upper-bounding its entanglement entropy. More strongly, a low bond dimension MPS can approximate all one-dimensional wave functions with low enganglement entropy. To be more precise, it can be proved that, if a one-dimensional wave function $|\psi\rangle$ follows an area law of entanglement, *i.e.*, the entanglement entropy saturates to a finite value that is independent of the system size, then for a given approximation error ϵ there exists a system size independent bond dimension χ for which we can find an MPS that approximates $|\psi\rangle$ within error ϵ.

It turns out thus that MPSs provide an excellent framework to encode area law, one-dimensional wave functions. The ground states of local, gapped, one-dimensional Hamiltonians follow an area law of entanglement. MBL highly-excited eigenstates follow an area law as well. For the former case, the density matrix renormalization group (DMRG) is a very successful algorithm for finding MPS representations of ground states of such Hamiltonians. In the latter case, the shift-and-invert MPS algorithm lets us find MPS representations of MBL eigenstates with machine high precision. Note that an MPS defined over a spin system of L sites and bond dimension upper-bounded by χ has $\mathcal{O}(2 \times \chi \times L)$ tensor entries, which scales linearly with system size, as opposed to the exponential scaling of $|\psi\rangle$ when explicitly written as a vector in Hilbert space. The time and moemory complexity of the contraction of an MPS to compute expectation values or matrix elements of local observables, such as those in Fig. 2.2, also scales polynomially with χ ($\mathcal{O}(\chi^4)$) and linearly in L. Finally, DMRG and SIMPS can find the target MPS representations of eigenstates with a modest amount of resources as well.

Ground states: density matrix renormalization group

We have already discussed the fact that MPSs are excellent memory-efficient placeholders for area law, one-dimensional wave functions, such as the ground states of gapped, local, one-dimensional Hamiltonians. Furthermore, we have seen that, once we have an MPS, computing local observables is also an efficient procedure, both memory and time wise. We now explore the question of how to find a good MPS representation of a ground state of a gapped, local, one-dimensional Hamiltonian in polynomial time. The DMRG algorithm provides the standard way in which this optimization is carried out [104, 105].

First, let us introduce the concept of a matrix product operator (MPO). A local Hamiltonian, such as the one in Eq. (1.7), acts on all sites of a spin chain, as opposed to the examples of Fig. 2.2, where the operator O affected only a single site. Despite this fact, there is a tensor network that exploits the locality of the Hamiltonian and encodes it in a very frugal way: an MPO. An MPO (see top panel of Fig. 2.5) is very similar to an MPS, with the difference that each tensor $W^l_{\sigma_l,\sigma'_l;b_{l-1},b_l}$ has two physical indices, σ_l and

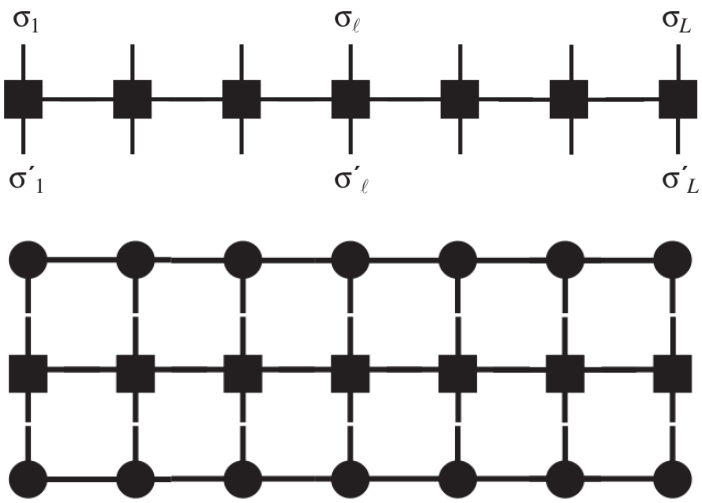

Figure 2.5: (From Ref. [83]) **Top:** MPO representation of a local Hamiltonian. **Bottom:** pictorial representation of $\langle\psi| H |\psi\rangle$, where $|\psi\rangle$ is an MPS and H is represented by the MPO in the middle.

σ_l'. Indeed for local Hamiltonians, the bond dimension of the virtual indices, b_{l-1} and b_l is very small (5 for the Hamiltonian of Eq. (1.7)), and independent of system size. Moreover, computing the expectation value of H for an MPS $|\psi\rangle$, $\langle\psi| H |\psi\rangle$, is efficient (see bottom panel of Fig. 2.5).

Given an MPO representation of a Hamiltonian H and a randomly initialized MPS $|\psi_0\rangle$ with bond dimension χ, DMRG iteratively optimizes the parameters (tensor entries) of $|\psi_i\rangle$ (i labels iterations), converging to a good MPS representation of the ground state of H (provided that the Hamiltonian is gapped, local, and one-dimensional). Each iteration optimizes the entries of a single tensor M^l in the chain [2] , and contiguous tensors are optimized in consecutive iterations, following a sweeping fashion in which we optimize tensors in ascending order, from left to right, and then in descending order, from right to left; many sweeps are performed until convergence. The optimization i of a single site l proceeds as follows:

1. Canonize the $|\psi_{i-1}\rangle$ around sites l and $l+1$ (simply left canonize if the site is $l = L$).

2. Remove tensor M^l from both the *bra* and the *ket* MPSs of the MPS-MPO-MPS tensor network $\langle\psi| H |\psi\rangle$.

3. Contract the resulting tensor network. The resulting tensor $\tilde{H}$ has $\{\sigma_l, a_{l-1}, a_l; \sigma_l', a_{l-1}', a_l'\}$; when written as a matrix with the following superindices, $\tilde{H}_{(\sigma_l, a_{l-1}, a_l);(\sigma_l', a_{l-1}', a_l')}$, $\tilde{H}$ is equal to H projected onto the subspace spanned by all partial derivatives $\left\{ \frac{\partial}{\partial M^l_{\sigma_l; a_{l-1}, a_l}} |\psi_{i-1}\rangle \right\}$, which for an orthonormal basis of this subspace.

[2] There is also a two-site version of DMRG, in which pairs of contiguous tensors are optimized simulatneously, which for simplicity we do not present here, but which is actually more popular than the one-site verion.

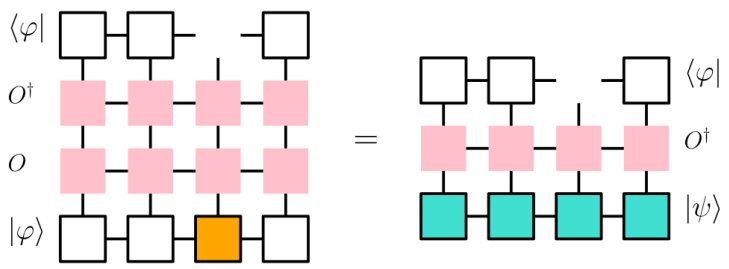

Figure 2.6: (From Ref. [107]) Setup for the optimization performed in each iteration of the SIMPS algorithm.

4. Solve for the ground state of this projected Hamiltonian and replace the $2 \times B_{l-1} \times B_l$ many entries of M^l by the corresponding entries of this low dimensional ground state.

5. Rename the updated MPS $|\psi_i\rangle$ and go to the next iteration.

This way, DMRG iteratively looks for ground states of H projected onto low dimensional subspaces. The time complexity of the diagonalization step of DMRG scales as $\mathcal{O}(\chi^6)$, or $\mathcal{O}(\chi^4)$ if we use a Lanczos-like solver. DMRG is the standard method to find ground states of non-critical, one-dimensional, local Hamiltonians.

Highly-excited states: shift-and-invert MPS

A straightforward to adapt DMRG to flow towards an excited state at a target energy E would be to modify the diagonalization step and look for the excited state of $\tilde{H}$ that is closest to E in energy. However, in practice a different, slightly more involved approach, works better. This is the shift-and-invert MPS (SIMPS) algorithm [107], which we describe in this section.

SIMPS is based on the idea of repeatedly applying O^{-1}, $O = H - E$, to $|\psi\rangle$ until it converges to an eigenstate of H that is close to E in energy. However, explicitly computing O, either as a matrix or in MPO representation, is infeasible. As an alternative, SIMPS relies on sweeping procedure, similar to that one of DMRG. A few sweeps aim at approximately applying O^{-1} to $|\psi\rangle$, by finding the $|\phi\rangle$ that minimizes $|O|\phi\rangle - |\psi\rangle|^2$; this is achieved at the fixed point:

$$\frac{\partial}{\partial \phi^*_{l,\sigma_l}} \langle\phi| O^\dagger O |\phi\rangle = \frac{\partial}{\partial \phi^*_{l,\sigma_l}} \langle\phi| O^\dagger |\psi\rangle \tag{2.9}$$

for all sites l, where the notation $\frac{\partial}{\partial \phi^*_{l,\sigma_l}}$ represents the tensor resultant after removing M^l from either the $\langle\phi| O^\dagger O |\phi\rangle$ or the $\langle\phi| O^\dagger |\psi\rangle$ tensor networks. This fixed point equation is pictorially represented in Fig. 2.6, and corresponds to a linear system of equations over the parameters of M^l. For each iteration, we solve this linear system of equations and proceed to optimize the next site in the sweep, *without updating M^l with the new values*. For stability reasons, we only update M^l after we have performed an entire sweep.

The time complexity of SIMPS is dominated by the linear system of equations step, which scales as $\mathcal{O}(L\chi^6)$ for direct solvers and as $\mathcal{O}(L\chi^4)$ for indirect solvers. We have extensively used SIMPS to find highly excited eigenstates of MBL Hamiltonians at a target energy E. Although computationally more expensive than DMRG, due in part to the larger bond dimensions needed, in practice it achieves convergence down to machine precision.

2.3 Obtaining integrals of motion

We saw in Section 1.3.4 that an FMBL system has a complete set of local integrals of motion. Given a spin Hamiltonian H and a unitary matrix U that diagonalizes it, the set of pseudo-spin operators $\{\tau_i^z\}$ defined as follows:

$$\tau_i^z \equiv U\sigma_i^z U^\dagger, \tag{2.10}$$

forms a complete set of local integrals of motion, which commute with H and also with each other. However, the unitary matrix U that diagonalizes H is not unique, and so the choice of the set of $\{\tau_i^z\}$ is not unique either. In general, there is no guarantee that the pseudo-spins obtained are local, or that they are as local as possible. In particular, one could permute the columns of U, as well as freely choose their sign, defining another unitary matrix $\tilde{U}$, which would also diagonalize H. There are as many choices of sets of $\{\tau_i^z\}$ as permutations of the columns of U and choices of each of their signs.

Given the vast number of choices of U one could make, we rely on heuristics to obtain a choice that is good, *i.e.*, that is able to find local integrals of motion (l-bits) for FMBL Hamiltonians. Here we make use of the Wegner-Wilson flow (WWF) of Ref. [103], which was introduced in the context of MBL in Ref. [71]. While computationally expensive, the WWF provides good results in finding l-bits. The WWF defines a continuous trajectory for the Hamiltonian $H_{\mathrm{WWF}}(\beta)$ and for the unitary matrix $U_{\mathrm{WWF}}(\beta)$ as a function of the parameter β, which ranges from 0 to ∞. At $\beta = 0$, $H_{\mathrm{WWF}}(0) = H$ and $U_{\mathrm{WWF}}(0) = \mathbf{1}$; at $\beta = \infty$, $H_{\mathrm{WWF}}(\infty) = D$, where D is a diagonal matrix with the eigenvalues of H, and $U_{\mathrm{WWF}}(\infty) = U$, which

diagonalizes H. The equations of motion that define the WWF trajectory are given by:

$$H(\beta) = H_0(\beta) + V(\beta), \tag{2.11}$$

$$\eta(\beta) = [H_0(\beta), V(\beta)], \tag{2.12}$$

$$\frac{dU(\beta)}{\beta} = \eta(\beta), \tag{2.13}$$

$$\frac{dH(\beta)}{\beta} = [H(\beta), \eta(\beta)], \tag{2.14}$$

$$\tag{2.15}$$

where $H_0(\beta)$ is the diagonal part of matrix $H(\beta)$, $V(\beta)$ is the off-diagonal part of matrix $H(\beta)$, and $\eta(\beta)$ is the generator of the flow.

Numerical integration of Eqs. (2.11) lets us evolve numerically from $H(0)$ and $U(0)$ to $H(\beta \gg 1)$ and $U(\beta \gg 1)$. Although exactly diagonalizing H would require integrating the WWF for an infinite amount of time (or for a very large amount of time if we want to achieve machine precision), at $\beta \gg 1$, the matrix $U(\beta)$ approximately diagonalizes H. At that point, we compare $U(\beta \gg 1)$ to the matrix U_{ED} obtained with a more standard and efficient diagonalization, which does indeed achieve provide exact diagonalization up to machine precision, but which, as discussed above, has the "wrong" choice of column order, as well as of their sign structure. By applying bipartite matching on the sets of columns of both matrices, $U(\beta \gg 1)$ and U_{ED}, we can reorder the columns of U_{ED} provide them with the right signs, so we effectively obtain $U(\beta = \infty)$ up to machine precision. We can now use $U(\beta = \infty)$ to compute a set of l-bits from Eq. (2.10) that are indeed local in the FMBL.

Note that there is no step in the WWF procedure described above that requires H to be in the FMBL phase. Indeed, we do apply this procedure to Hamiltonians on both sides of the transition, in order to obtain phenomenology also in the ergodic phase, as well as at the transition; however, the WWF is much less expensive in the MBL phase, where the τ operators are local and thus close to the σ spin operators, requiring only a low-depth quantum circuit (in the quantum computing terminology) to achieve good results.

There is a sense in which a continuous flow diagonalization of H (as is the case for the WWF) is the right choice for the construction of U, such that it preserves locality in the transformation between σ and τ operators. This can be intuitively understood as follows. If a local Hamiltonian is already diagonal in the basis of spin configurations, then its l-bits are simply $\{\sigma_i^z\}$. In that case, $U = \mathbf{1}$, and permutations and sign flips of the columns of $\mathbf{1}$ would lead to a poor choice of l-bits, which will have lost part of the locality inheret to $\{\sigma_i^z\}$. The WWF starts with $U(\beta = 0) = \mathbf{1}$, and then evolves continuously from there, thus

avoiding discrete changes, such as sign flips and column permutations. A flow diagonalization procedure that is continuously connected to the identity operator is a better candidate to preserve locality than a precedure that involves discrete transformations.

2.4 Exploiting symmetry

Symmetry is a recurrent concept in phsyics. In quantum mechanics, we say that a Hamiltonian has a symmetry operator O if $[H, O] = 0$. This has several implications over the Hamiltonian H. One of these implications is that the time evolution of a state that is initialized with an expectation value of O equal to $\langle O \rangle$ will preserve this expectation value along its trajectory. Another consequence of this symmetry is that there exists a basis of vectors which are simultaneously eigenvectors of H and O. In that case, the eigenvalues of O divide this basis of eigenvectors into sets, each labeled by its corresponding eigenvalue of O. We then say that O is a good quantum number of the eigenvectors of H. The subspace spanned by each of these sets of basis vectors is called a symmetry sector of Hilbert space.

Dividing Hilbert space in different sectors has the advantage of letting us know that the cross terms of the Hamiltonian between states in different sectors are 0. In the case that the symmetry is simple enough that we can build a basis of a particular sector (not necessarily the basis of eigenstates, which might be unknown), then we can diagonalize the Hamiltonian in this sector alone; this is a much simpler task that diagonalizing H in the full Hilbert space, which might have a much larger dimension than each particular sector. If we have a basis for each symmetry sector, then H can be written as a block diagonal matrix, each block corresponding to a different sector. It should be obvious that diagonalizing each block separately is computationally a much simpler task than diagonalizing the full matrix of H.

The standard model of MBL presented in Eq. (1.7) has total magnetization symmetry, which means that it commutes with the operator $M \equiv \sum_i \sigma_i^z$ [3] . Interestingly, this symmetry is indeed a symmetry for all values of W, as well as for any particular disorder realization; it is therefore a symmetry over the entire family of Hamiltonians defined in Eq. (1.7). For a system of L spins, where L is even, the total magnetization has eigenvalues $M = -L, -L+2, \ldots, -2, 0, 2, \ldots L-2, L$; similarly for odd L. This symmetry is indeed simple enough that we can write down a basis for each magnetization sector. For $M = -L$, the sector has a single vector $|\downarrow\downarrow \ldots \downarrow\rangle$. A basis for the $M = -L+2$ sector includes all configurations with two spins up: $\{|\uparrow\uparrow\downarrow\downarrow \ldots \downarrow\downarrow\downarrow\rangle, |\uparrow\downarrow\uparrow\downarrow \ldots \downarrow\downarrow\downarrow\rangle, |\uparrow\downarrow\downarrow\uparrow \ldots \downarrow\downarrow\downarrow\rangle, \ldots, |\downarrow\downarrow\downarrow\downarrow \ldots \downarrow\uparrow\uparrow\rangle\}$. For other sectors we proceed in a similar way. Indeed, bases for all sectors are subsets of the spin configuration basis. The dimension of each sector

[3] When the fermionic version of this spin Hamiltonian is considered, then this symmetry is called *particle conservation* symmetry, and the operator $N = \sum_i n_i = \sum_i c_i^\dagger c_i$ commutes with H.

is equal to $\binom{L}{M}$. The zero-magnetization sector ($M = 0$) is of particular interest. It is the largest sector of all magnetization sectors, and its basis is composed of all configurations with equal number of spins up and down. We will often work in this sector, in which the Hamiltonian becomes a $\binom{L}{L/2} \times \binom{L}{L/2}$ sparse matrix.

The presence of symmetry sectors provides a computational advantage (both memory and time wise) to other routines that we have used in this thesis as well. Matrix product states and its algorithms can be constrained to particular symmetry sectors, and so finding highly excited eigenstates using SIMPS benefits from this. The WWF presented in Section 2.3 benefits from working with smaller matrices H and U. Finally, the computation of quantum mutual information between pairs of spins becomes computationally cheaper when total magnetization is an integral of motion and we work in the zero-magnetization sector, as we discuss in Section 2.5.

2.5 Computing the two-site quantum mutual information

The quantum mutual information (QMI) measures all correlations, classical and quantum, between two subregions of a system, A and B. The QMI is defined as

$$QMI_{AB} \equiv S_A + S_B - S_{AB}, \tag{2.16}$$

where S_A (S_B, S_{AB}) is the entanglement entropy between A (resp. B, $A + B$) and the rest of the system. The term $-S_{AB}$ subtracts correlations of A or B with other parts of the system. In this thesis we work with the two-site QMI between sites i and j, QMI_{ij}, for which both A and B are single sites. In the two-site, spin-$\frac{1}{2}$ case, the QMI is upper bounded by $2\log(2)$, which is the value it takes when two spins form a singlet, with $S_i = S_j = \log(2)$ and $S_{ij} = 0$. When a subset of spins form a multi-site "cat" state, then $S_{ij} = \log(2)$ as well, asn the QMI betwen all pairs of spins involved in the cat state is $\log(2)$.

The QMI involves the computation of a large number of entanglement entropies, which itself involves the computation of a large number of reduced density matrices; for enganglement entropies between one or two sites and the rest of the system, most of the computation time is being spent in tracing out the degrees of freedom of the environment of those one or two sites. Fortunately, for spin models with total magnetization symmetry in the zero-magnetization sector, we can derive analytically the one and two-site reduced density matrices analytically; evaluation of these analytical formulas relies on the computation of a few expectation values, which are easily obtained.

The one-site reduced density matrix on site i is

$$\rho_i = \begin{pmatrix} b & 0 \\ 0 & 1-b \end{pmatrix} \tag{2.17}$$

and the two-site reduced density matrix on sites i and j is

$$\rho_{ij} = \begin{pmatrix} a & 0 & 0 & 0 \\ 0 & b-a & d^* & 0 \\ 0 & d & c-a & 0 \\ 0 & 0 & 0 & 1-b-c+a \end{pmatrix}, \tag{2.18}$$

where $a \equiv \langle n_i n_j \rangle$, $b \equiv \langle n_i \rangle$, $c \equiv \langle n_j \rangle$, and $d \equiv \langle \sigma_i^+ \sigma_j^- \rangle$; and where $n_i \equiv \frac{\sigma_i^z + 1}{2}$.

Chapter 3

Exploring one-particle orbitals in large many-body localized systems

This chapter is mainly based on Ref. [97].

3.1 Introduction

The eigenstate thermalization hypothesis (ETH) [19, 26, 31, 74, 79, 91, 92] provides a mechanism for the thermalization of generic isolated quantum systems. A pure quantum state initially prepared to be sharply peaked in energy can relax to the thermodynamic equilibrium in the sense that subsystems evolve such that their reduced density matrix looks like a mixed thermal density matrix whose temperature is characterized by the energy of the initial state. In this way, a pure quantum state can behave locally like a mixed thermal state. The mechanism of thermalization is provided by the special structure of local operators in the eigenbasis of the Hamiltonian, where they become a smooth function of energy in very large systems.

In contrast, the phenomenon of Anderson localization [7] describes the existence of an insulating phase that fails to thermalize in closed, non-interacting, quantum systems with quenched disorder. In one dimension, any arbitrarily small amount of disorder leads to localization.

Surprisingly, the presence of strong interactions does not completely destroy this phenomenon. Contrary to naive expectations that strongly interacting systems are always ergodic, a large number of studies following pioneering works [11, 34, 35] showed that usually interactions can stabilize an ergodic phase only at weak disorder, while at strong disorder the system many-body localizes (MBL) (see Refs. [2, 3, 5, 6, 41, 56, 63] for recent reviews). The MBL transition between the ergodic and localized phases has been the focus of many recent numerical studies [6,15,44,46,47,59,64,67,72,78,101,106,108,110] , and numerical evidence points to the existence of a mobility edge (although the existence of a mobility edge is not settled [27]): for disorder strengths W below a critical value, MBL eigenstates at low and high energy density are separated at a critical energy density ϵ from extended eigenstates in the center of the spectrum [59] (see Fig. 3.1 for an illustration of the phase diagram). MBL can be seen as a novel eigenstate quantum phase transition [69] in which eigenstates radically change their nature as a function of disorder strength (or energy), going from thermal

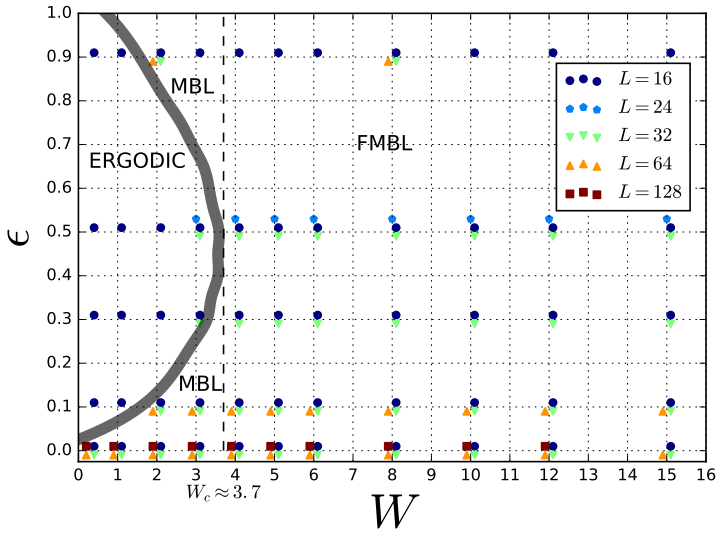

Figure 3.1: Phase diagram in the disorder strength W and energy density ϵ plane for the model in Eq. (3.1) with $t = V = 1$. The mobility edge is plotted from the results of Ref. [59]. In this work, we numerically access eigenstates at the depicted points.

eigenstates in the ergodic phase, which follow ETH and exhibit a volume law scaling of the entanglement entropy, to MBL eigenstates in the MBL phase, which violate ETH and exhibit an area law scaling of the entanglement entropy [12, 106].

For systems whose entire spectrum is MBL (fully MBL or FMBL), it is possible to find a complete set of local integrals of motion or l-bits [20,22,40–42,61,70,71,75,80,86,102] , which are responsible for a logarithmic growth of the entanglement entropy following a global quench in the MBL phase [10, 23, 60, 87, 89, 109, 110]. The emergent integrability as signaled by a complete set of l-bits of an FMBL system is lost below the critical disorder strength in the presence of a mobility edge, where the existence of thermal eigenstates prevents any set of integrals of motion from containing only local operators. Unfortunately, the numerical determination of the l-bit operators is very difficult and does not scale favorably for large system sizes. Therefore, a simplified proxy of l-bits is desirable and has been proposed earlier [13, 14, 53]: the one particle density matrix (OPDM) and its eigenvectors, the one particle orbitals (OPOs). The OPOs, which in the non-interacting limit become exact integrals of motion, have occupations in the MBL phase that are close to 0 and 1 [14]. They provide an effective first approximation to the l-bits and a well-defined, natural, continuous connection to the notion of integrability in the absence of interactions. Unlike the integrals of motion, the OPDM is defined over single eigenstates, which in the MBL phase are obtainable for large systems using DMRG-like methods [32, 39, 43, 45, 52, 107].

3.2 Summary of results

In this work we present a detailed numerical study of the behavior of the OPOs of the eigenstates of the model of Eq. (3.1) using shift-and-invert MPS (SIMPS) [107], an MPS-based algorithm that allows us to access excited MBL eigenstates for 1D systems of size much larger than those studied using exact diagonalization (ED) techniques. For systems of size up to at least $L = 64$, SIMPS can access eigenstates at low energy densities at disorder $W < W_c$ (see Figs. 3.1 and 3.2), which supplies evidence for the existence of the mobility edge.

In Section 3.6.1 we study the structure of the OPOs and their number operators as one particle approximations of the integrals of motion. We find that the OPOs of MBL eigenstates decay exponentially in real space. The OPOs' number operators, which encode the one particle content of the l-bits, have also an exponentially decaying weight in real space. Their correlation length (same in both cases) increases monotonically as the disorder is lowered, but does not obviously diverge. The correlation length is weakly system size dependent in the MBL phase and, as we can see for small systems, its dependence with energy density ϵ suggests the existence of the mobility edge. The number operators of the OPOs are defined by string operators of different ranges in real space whose coupling constants approach a "$1/f$" distribution (or equivalently a log-uniform distribution) for a fixed range at strong disorder and large ranges, similar to the distribution seen in Ref. [71]. This distribution follows naturally from the exponential decay of the OPOs. The OPOs and their number operators have a localized support at strong disorder. The distribution of supports decays exponentially fast away from weak disorder, but becomes flat and extensive when the disorder is small. The correlation length of this decay has several similarities with the one of the decay of the OPOs in real space.

In Section 3.6.2 we analyze the inverse participation ratio of the OPOs as a measure of their localization. Our results suggest that MBL eigenstates below a mobility edge in energy density ϵ reveal the presence of an ergodic phase at a higher ϵ. This makes it possible to estimate the critical value of the disorder strength W_c, typically determined for the ergodic-MBL transition at $\epsilon = 0.5$ (see Fig. 3.1), from MBL eigenstates at $\epsilon \ll 0.5$.

In Section 3.6.3 we find that the OPOs extracted from eigenstates at different values of ϵ have high overlap, and their occupations are correlated to the energy of the eigenstate. This provides the OPOs with a certain universality across the energy spectrum.

In Section 3.6.4 we analyze the occupation spectrum of the eigenstates obtained for large systems. Our results are in agreement with those of Refs. [13, 14]: the occupations present a gap for MBL systems that becomes smaller as the ergodic phase is approached. The ϵ dependence of the gap is the one expected in the

presence of a mobility edge. In addition, larger systems seem to have an ergodic region of the phase diagram that penetrates further into larger W values.

Finally, we study the standard deviation of the entanglement entropy of the MBL eigenstates at half-cut in Section 3.6.5. As is discussed in Ref. [47], it shows a peak at the critical disorder strength. Our results confirm that all eigenstates accessed by SIMPS are in the MBL region. Also, the location of the peaks at different energy densities indicate once again the presence of a mobility edge.

3.3 The model

We study spinless fermions with nearest neighbor repulsion V, a hopping matrix element t, subject to a random potential μ_i on an open chain with Hamiltonian:

$$\begin{aligned}\hat{H} = -\frac{t}{2}\sum_{i=0}^{L-2}\left(\hat{c}_i^\dagger \hat{c}_{i+1} + \hat{c}_{i+1}^\dagger \hat{c}_i\right) \\ +V\sum_{i=0}^{L-2}\hat{n}_i\hat{n}_{i+1} + \sum_{i=0}^{L-1}\mu_i\hat{n}_i.\end{aligned} \tag{3.1}$$

where $\hat{n}_i = \left(\hat{c}_i^\dagger \hat{c}_i - \frac{1}{2}\right)$ and the random potential is sampled from a uniform distribution of width $2W$, *i.e.* $\mu_i \in [-W, W]$, where W denotes the disorder strength. In this work, we let $t = V = 1$. The model in Eq. (3.1) has been extensively studied in the context of MBL [4,8,9,12,14,15,44,46,54,55,57,59,60,63,64,67, 85,99,106,110]. Among its characteristics, this model exhibits a mobility edge that separates the MBL phase (at low and high values of ϵ) from the delocalized phase (at intermediate values of ϵ) for $W < W_c$, where $W_c \approx 3.7$ (see Fig. 3.1 and Ref. [59]). In addition, eigenstates in the delocalized phase obey a volume law for the entanglement entropy as a function of subsystem size, while MBL eigenstates follow an area law [12]. Close to the transition, the subsystem entanglement entropies are described by a bimodal distribution [106], and the standard deviation of the distribution of half-cut entanglement entropies peaks at the transition value of W for each energy density [47].

Note that the Hamiltonian in Eq. (3.1) is connected to the random field Heisenberg chain through a Jordan-Wigner transformation and that the model is integrable at $W = 0$.

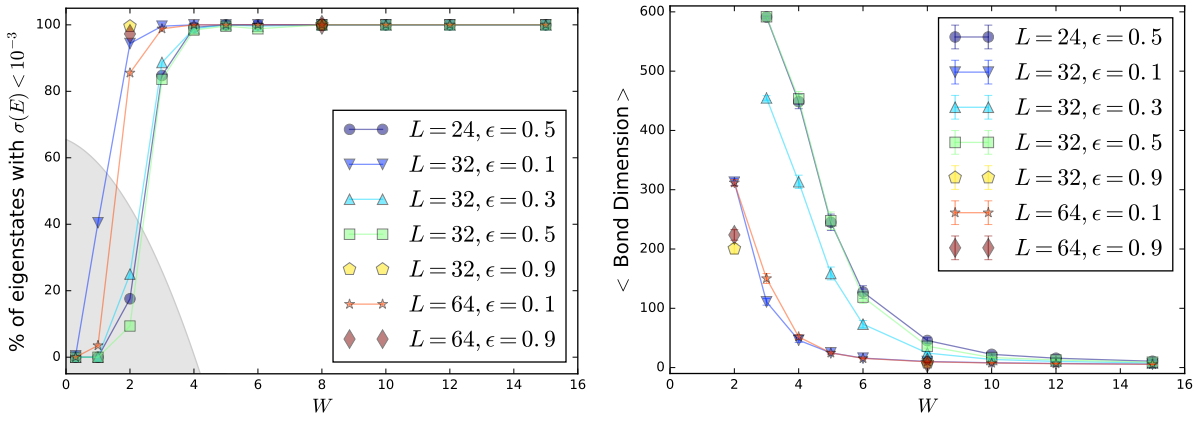

Figure 3.2: *Left:* percentage of eigenstates accessed by SIMPS that pass our filter for the standard deviation of the energy, $\sigma(E) < 10^{-3}$. Eigenstates in the MBL region are accessed successfully through SIMPS with a low value of $\sigma(E)$, whereas eigenstates in the ergodic region (see Fig. 3.1) fail to be represented accurately by the low bond dimension MPS ansatz. We neglect the eigenstates in the gray area due to the bias the strong filtering might introduce. *Right:* average bond dimension at half-cut of the eigenstates kept after filtering. As expected, the bond dimension diverges close to the transition, where it also becomes strongly system size dependent and it is eventually cutoff by the finite bond dimension used in SIMPS.

3.4 One Particle Density Matrix (OPDM)

Given a pure state $|\psi\rangle$ of a system, the OPDM ρ is defined as:

$$\rho_{ij} \equiv \langle\psi| \hat{c}_i^\dagger \hat{c}_j |\psi\rangle , \tag{3.2}$$

which was introduced in the context of Bose-Einstein condensation [73], and was studied in Ref. [13, 14] in the context of MBL. For a spinless, fermionic chain of length L, ρ is a matrix of size $L \times L$, while $|\psi\rangle$ is a vector of size 2^L.

We can diagonalize ρ as:

$$\rho_{ij} = U_{ik} n_k U_{kj}^\dagger, \tag{3.3}$$

where the eigenvalues n_k of ρ are the occupations of the number operators $a_k^\dagger a_k$, where $a_k^\dagger \equiv \sum_i U_{ki}^\dagger c_i^\dagger$. These rotated operators define the L one particle orbitals (OPOs) $|\phi_k\rangle \equiv \sum_i U_{ki}^\dagger |i\rangle$, where $|i\rangle$ is the one particle wave function with a single fermion on site i. For convenience, we will order the OPOs by increasing value of their occupation n_k, unless otherwise specified.

For a non-interacting system and a particular eigenstate $|\psi\rangle$, the set of eigenvalues of the OPDM ρ (or equivalently, the set of occupations of the OPOs) is highly degenerate, consisting only of the values 0 and

1. Furthermore, there is a set of OPOs which simultaneously diagonalizes the OPDM of all eigenstates. The number operators associated to these OPOs form a complete set of integrals of motion of the system and their occupations uniquely specify an energy eigenstate. For an interacting system there is no such set of OPOs. However, we show in Section 3.6.3 that the OPOs drawn from different eigenstates have a high overlap, and their occupations are correlated with the energy of the eigenstates.

In interacting systems, it has been shown that the spectrum of occupations $\{n_k\}$ of the OPDM contains a large gap for MBL eigenstates which gets smaller as the ergodic phase is entered, eventually closing for small values of the disorder strength [13, 14] When the gap is large, the spectrum of occupations is close to that of the non-interacting system; in the limit of infinite disorder the non-interacting picture is fully recovered. This one particle picture provides thus not only a heuristic to characterize MBL and ergodic phases, but also a powerful point of view on the emergence of integrability in the MBL phase, since the one particle orbitals may be interpreted as the one particle operator content of the l-bits, which makes them a very good approximation for l-bits at strong disorder.

While the occupations indicate the nature of the dynamical phase at the energy density and W corresponding to an eigenstate, we will see in Section 3.6.2 that the structure of the OPOs allows us to discern between an MBL eigenstate of an FMBL Hamiltonian from one that is located in energy below a many-body mobility edge. The OPDM encodes therefore two distinct pieces of information: while the occupations of the OPOs characterize the phase of an eigenstate, some properties of the OPOs themselves can signal the presence of a mobility edge.

3.5 Numerical simulations

We analyze the model from Eq. (3.1) by obtaining eigenstates in the half-filled sector at different energy densities, for systems of different sizes L and disorder strengths W. The energy density is defined as $\epsilon \equiv (E - E_{min})/(E_{max} - E_{min})$, where E is the energy of the eigenstate and E_{max} and E_{min} are respectively the maximum and minimum energies in the energy spectrum (in all sectors for finite energy density data and in the half-filled sector for ground state results). The phase diagram of this model (taken from Ref. [59]) and the points studied can be seen in Fig. 3.1. For each of the eigenstates accessed, the OPDM of Eq. (3.2) is computed and diagonalized, which leaves us with its OPOs and their occupations. Several disorder realizations are considered, and for each of them we obtain multiple eigenstates for each value of ϵ.

For the ground state ($\epsilon = 0$) we use Lanczos ED ($L = 16$) with 400 disorder realizations and DMRG constrained to the half-filled sector ($L > 16$) with 128 disorder realizations. For each value of $\epsilon > 0$ at finite

energy density, we use shift invert ED ($L = 16$) with 400 disorder realizations and SIMPS [107] ($L > 16$) with 128 disorder realizations. Two eigenstates are generated for every pair (W, ϵ). If SIMPS converges to the same eigenstate twice (which happens in less than 0.26% of the cases), the duplicate is removed [1]. SIMPS exploits the low entanglement of the MBL eigenstates to represent them efficiently using an MPS ansatz. For eigenstates accessed by SIMPS in the strong disorder limit, the standard deviation of the energy is as low as $\sim 10^{-8}$ (machine precision in the variance of the energy); the increase in entanglement as we approach the transition makes the algorithm obtain eigenstates with a lower precision for fixed bond-dimension. For this reason, we filter the ensemble of eigenstates by removing states whose standard deviation of the energy is higher than 10^{-3} (see Fig. 3.2). To minimize the possibility that either allowing states with a big standard deviation of the energy or restricting our results to only the eigenstates that have a very small standard deviation biases our results, we have tested different thresholds and find that 10^{-3} gives robust results against large changes in the threshold.

3.6 Results

3.6.1 Correlation length and support of the OPOs

At strong disorder, each OPO is centered around a single site with an exponentially fast decay (as will be discussed below). As the disorder is lowered, we occasionally see more than one center and slower decay. If we consider a single eigenstate, we can examine the probability density in real space of the set of OPOs (see Fig. 3.3 for a generic example). Notice that at moderate to large disorder, the OPOs are sharply localized at single sites. At small disorder, the OPOs primarily mix in small groups (3-5 OPOs) over a local set of sites which don't overlap each other. Moreover, OPOs primarily mix with other OPOs which are at similar occupation. Take for example the four sites 7 through 10 for $W = 3$ in Fig. 3.3, where all four OPOs which have non-negligible amplitudes over these sites mix. We speculate that OPOs that tunnel a certain distance over the chain are related to resonances in the eigenstate.

We now consider a definition of the "correlation length" which applies to operators and is in the spirit of the correlation lengths used for FMBL l-bits [2, 40] (often referred to as "localization length"). Each OPO

[1] Less than 0.54% of the runs were initialized on an eigenstate, preventing the algorithm from flowing to the desired energy density, and were therefore discarded. Less than 0.12% of the eigenstates were also removed because of code failure. Therefore, in addition to the subsequent energy standard deviation filter, there was a total discard rate of less than 0.91% due to technical reasons.

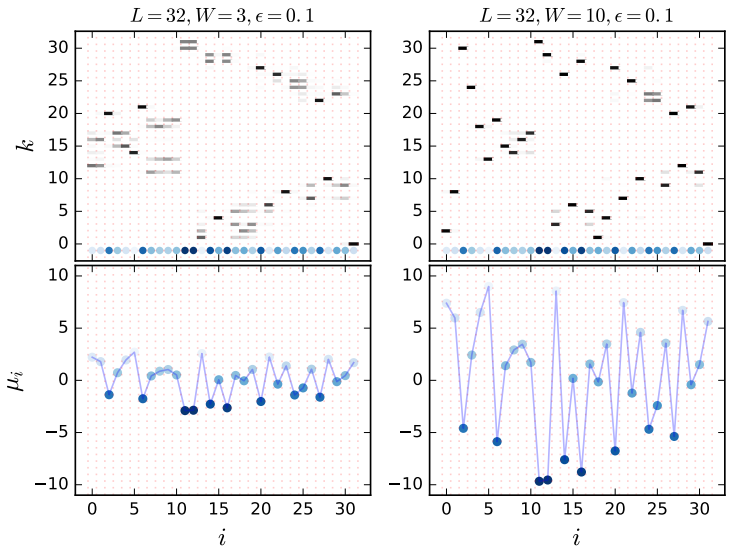

Figure 3.3: *Top:* Probability density $|U^\dagger_{ki}|^2$ in real space (i) of each OPO (k) of a particular eigenstate at $\epsilon = 0.1$ of a system of size $L = 32$ and $W = 3.0, 10.0$. *Bottom:* profile of the random chemical potential μ_i at $W = 3.0, 10.0$. At strong disorder (right), the OPOs are highly localized on one site. As the disorder is lowered, the OPOs start delocalizing, mixing over small non-overlapping subsystems of the chain. There is a high probability of mixing along sites with a similar μ_i, which occasionally gives rise to tunneling OPOs (see sites 14 and 16 at $W = 3.0$ for an example).

k has its maximum amplitude at some site m and has a number operator $a^\dagger_k a_k$ of the form:

$$a^\dagger_k a_k = \sum_{ij} f^k_{ij} c^\dagger_i c_j, \tag{3.4}$$

where $f^k_{ij} \equiv U^\dagger_{ki} U_{jk}$. We define the range R of the two-body strings $c^\dagger_i c_j$ relative to the localization center m as:

$$R \equiv \max\left(|i-m|, |j-m|\right) \tag{3.5}$$

(following the more general definition for l-bits of Ref. [2]; a different choice of a definition for the range R [40,71] has few practical consequences, and is discussed in Appendix F). We expect the total contribution to $a^\dagger_k a_k$ from operators $c^\dagger_i c_j$ of different ranges to decay exponentially fast as a function of their range at strong disorder. One way to quantify this is to define the contribution F^k_R from range R to OPO k as the sum of all coefficients $\left|f^k_{ij}\right|$ of a particular range:

$$F^k_R \equiv \sum_{\max(|i-m|,|j-m|)=R} \left|f^k_{ij}\right|. \tag{3.6}$$

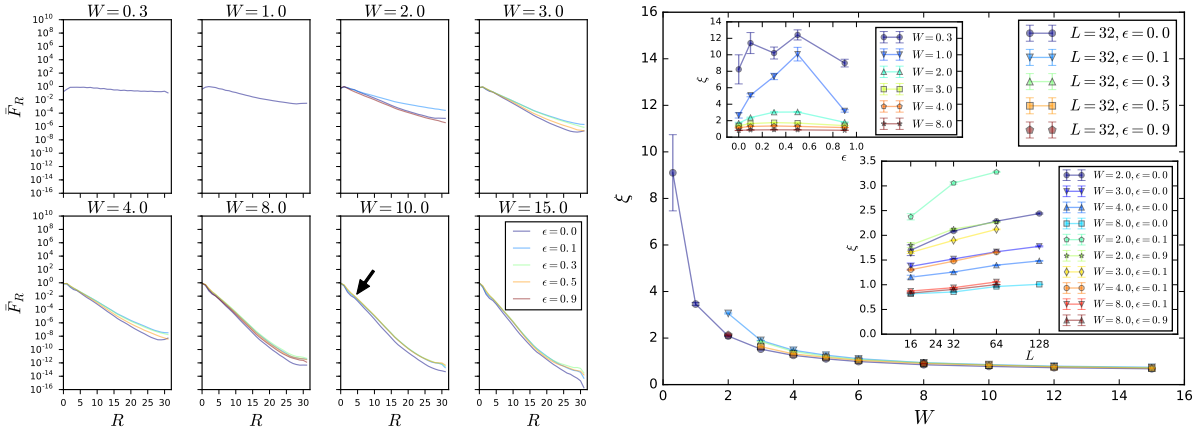

Figure 3.4: *Left:* total contribution F_R from string operators of range R to the definition of the OPO number operator $a_k^\dagger a_k$ (logarithmically) averaged over OPOs ($L = 32$). The average $\bar{F}_R$ decays exponentially with range R. *Right:* correlation length ξ extracted from the exponential decay of $\bar{F}_R$. *Insets*: system size and ϵ dependence of ξ ($L = 16$).

For simplicity, let's drop the OPO index k and simply refer to F_R^k of an OPO as F_R, unless otherwise specified. Fig. 3.4 presents the (logarithmic) average $\bar{F}_R$ across OPOs (within and across eigenstates) of F_R as a function of R for a system of size L=32 at different values of ϵ and W (left panel). Away from large R, where finite size effects are stronger, there is an exponential decay of $\bar{F}_R \propto e^{-R/\xi}$, with a characteristic correlation length ξ that is shown in the right panel of Fig. 3.4 (in fact, the exponential decay is not restricted to the average $\bar{F}_R$, but the raw distribution of F_R also follows this form, as can be seen in Fig. A.2 of Appendix A). As W gets smaller, ξ increases monotonically; interestingly, in the ground state, the correlation length seems to increase significantly at $W = 0.3$. The lack of any clear divergence at finite energy density is consistent with the fact that none of these points are in the ergodic phase. While at large disorder ξ is independent of energy density ϵ, at smaller disorder ($W \approx 2, 3$) ξ develops an energy density dependence, with larger values towards the middle of the spectrum; this dependence becomes strong in the weak disorder limit (see upper inset of Fig. 3.4); this is clearly suggestive of the mobility edge. The correlation length increases monotonically with system size (see lower inset of Fig. 3.4); although the precise functional form of the scaling is unclear, it is consistent with a logarithmically increasing correlation length within the MBL phase which might be the result of exponentially rare regions. See Appendix A for additional information on the correlation length ξ.

The exponential decay of $\bar{F}_R$ can be related to the exponential decay of the tails of the OPOs. Assuming that the average exponential decay of $\bar{F}_R$ is representative of a typical case, it can be argued (see Appendix B) that the decay of the tails of the OPOs is of the form $\left|U_{ki}^\dagger\right| \propto e^{-|i-m|/\xi}/\left(A + Bg(|i-m|)\right)$, where A and B are positive constants and $g(x)$ is a monotonically increasing function with limits $g(0) = 0$ and $g(\infty) = 1$. The decay of the number operator $a_k^\dagger a_k$ and that of the OPOs' tails therefore have the same asymptotic

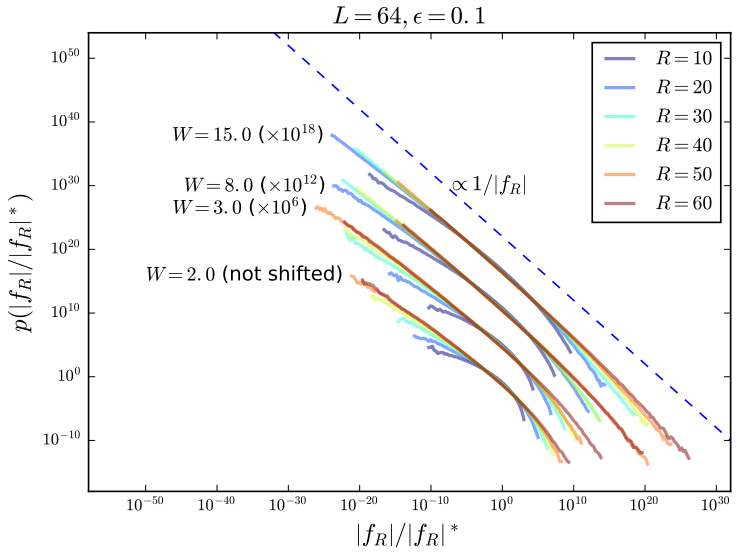

Figure 3.5: Probability distribution of the coupling constants $|f_R|$ divided by the typical coupling constant $|f_R|^* \equiv 10^{Mo(\log_{10}(|f_R|))}$ (where the mode $Mo\left(\log_{10}(|f_R|)\right) \equiv \text{argmax}\left[p\left(\log_{10}(|f_R|)\right)\right]$), $p\left(|f_R|/|f_R|^*\right)$, of the number operators of the OPOs at $\epsilon = 0.1$ for fixed W and range R, for systems of size $L = 64$. All curves, except for $W = 2$, have been shifted in the y axis for clarity; they would otherwise lay on top of each other and meet approximately at $|f_R| = |f_R|^*$ (where they are parallel to the $\propto 1/|f_R|$ reference line) and $p\left(|f_R|/|f_R|^*\right) \approx 10^{-1}$.

exponential behavior, with the same correlation length ξ. We verify this numerically (see Fig. B.1 in Appendix B).

Let $|f_R|$ be randomly sampled from the set of the magnitudes of the coefficients f_{ij}^k (from Eq. (3.4)) for fixed range R ($|f_R| \in \left\{\left|f_{ij}^k\right|\right\}_{R=const.}$) for fixed L, W and ϵ. The probability density of $|f_R|$, $p(|f_R|)$, decays as $\propto 1/|f_R|$ at large W and R, as shown in Fig. 3.5; note that $|f_R|$ has a lower cutoff, due to the finite size of the systems considered, and an upper cutoff, due to the normalization of the OPOs. This is the same behavior found in Ref. [71] for the coupling constants of the Hamiltonian written in the l-bit basis (although for a slightly different definition of the range; see Appendix F); the one particle approximation offers though a plausible explanation for this behavior, which arises directly from the exponential decay of the tails of the OPOs, and is discussed in Appendix F. In general, if the coupling constants of an l-bit decay exponentially at fixed range, in the sense that the probability density of the random variable $\log(|f_R|)$ is constant ($p\left(\log(|f_R|)\right) = const.$), which is the case here, then $p(|f_R|) \propto 1/|f_R|$, due to the identity $d\left(\log(|f_R|)\right)/dp(|f_R|) = 1/|f_R|$.

An alternative definition of the support of an OPO k is to let it be the size of the smallest region of the chain that contains 90% of the norm $\sum_i \left|U_{ki}^\dagger\right|^2$ of the OPO (the choice of a threshold of 90% is arbitrary). The effective support of the OPOs is representative of the localization of the system, and their distribution

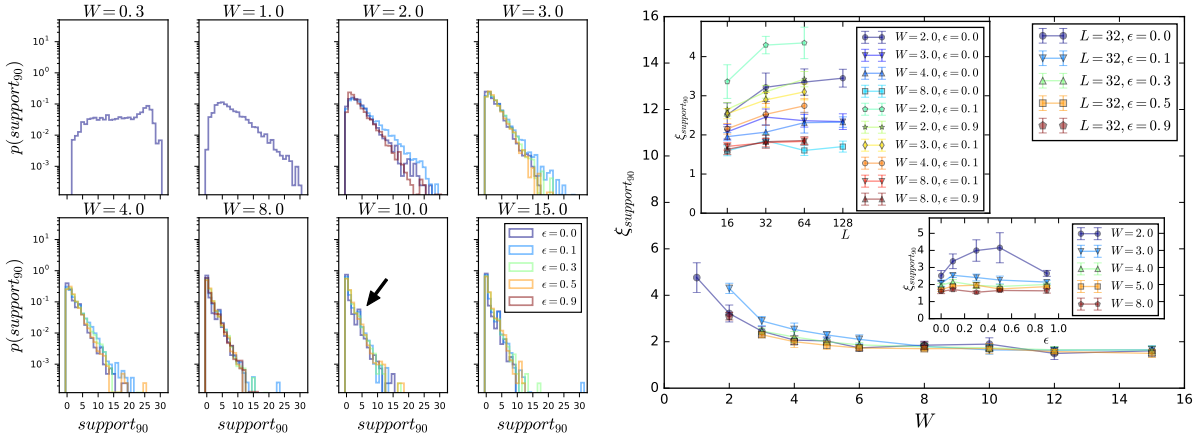

Figure 3.6: *Left:* distribution of the support of the OPOs for different energy densities as a function of W for $L = 32$. The $support_{90}$ is computed as the size of the region of that contains 90% of the norm L_2 of the OPOs. *Right:* correlation length $\xi_{support_{90}}$ corresponding to the exponential decay of the distributions in the left panel. *Insets*: system size and energy density dependence of $\xi_{support_{90}}$ ($L = 16$).

for several energy densities ϵ and disorder strengths W for systems of $L = 32$ is shown in the left panel of Fig. 3.6. The decay of the probability distribution is exponential at disorder strengths far from the weak disorder limit. At small disorder the distribution becomes flat; a system size dependence arises because the extent of the OPOs becomes longer than the system length. (see Fig. C.1 in Appendix C). For exponentially decaying distributions, $p(support_{90}) \propto e^{support_{90}/\xi_{support_{90}}}$, we define a correlation length $\xi_{support_{90}}$ (right panel of Fig. 3.6) [2]. At strong disorder, $\xi_{support_{90}}$ is effectively independent of ϵ and of system size. At $W < W_c$, an ϵ dependence arises, with higher values towards the middle of the energy spectrum (see lower inset of Fig. 3.6). Below $W \approx W_c$ the correlation length rises sharply (but does not obviously diverge) and might be weakly system size dependent. Note that at large disorder and low energy density there exists a kink (see arrow for an example) in the distribution for a support of length 4, which biases the probability of finding an OPO of $support_{90} = 4$. We think that this is related to the kink seen in Fig. 3.4 for the same cases (see arrow). This same effect is barely seen in the distribution of *support* of Fig. C.2 of Appendix C, but is visible in the distribution of $support_{90}$ of Fig. 3.6.

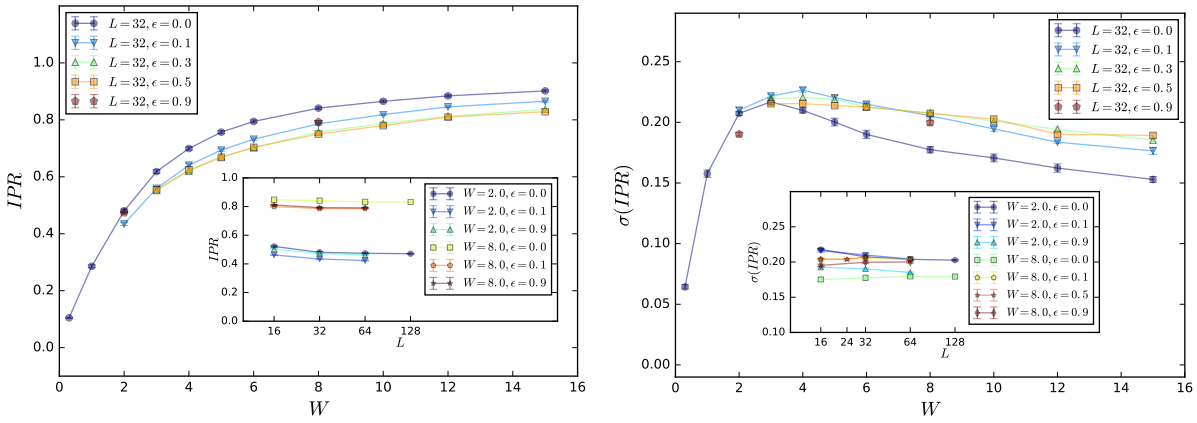

Figure 3.7: *Left:* IPR as a function of W for $L = 32$ averaged over OPOs and disorder. *Inset:* average IPR as a function of L. *Right:* standard deviation of the IPR of the OPOs for $L = 32$. *Inset:* standard deviation of the IPR as a function of L.

3.6.2 Inverse participation ratio of the OPOs

In this section we consider the inverse participation ratio (IPR), a measure of localization commonly used in Anderson localization. The IPR of the k'th OPO is defined as:

$$\text{IPR} = \sum_{i=0}^{L-1} |U^{\dagger}_{ki}|^4. \tag{3.7}$$

where $U^{\dagger}_{ki}$ is the matrix of OPOs that diagonalizes ρ, as defined in Section 3.4, and k labels the OPOs. The IPR of an OPO that is completely localized on one site is equal to 1, while a delocalized OPO that is evenly distributed among all sites of the chain has an IPR of $1/L$.

We study the distribution of IPRs of the OPOs obtained for different points in the phase diagram. Note that the average IPR increases monotonically with W (see left panel of Fig. 3.7), implying more localized orbitals at stronger disorder. Although this behavior is common to all values of the energy density, the curves depend slightly on ϵ, with lower values of the IPR towards the middle of the spectrum, and have a weak system size dependence at small disorder.

The standard deviation of the distribution of IPRs (across disorder realizations, eigenstates within each realization, and OPOs within each eigenstate), $\sigma(IPR)$, is presented in the right panel of Fig. 3.7. For all ϵ we find a peak of $\sigma(IPR)$. Like the peak seen in the standard deviation of the entanglement entropy at half-cut at the transition [47,106], the peak in $\sigma(IPR)$ can be viewed as identifying a transition between the

[2]Due to the difficulty of extracting $\xi_{support_{90}}$ from a single linear fit over the distributions of $p(support_{90})$, which are rather noisy, we compute their slope as the average of several linear fits performed over different ranges of the x-axis, weighted by the inverse of their standard errors. The error in the estimation of the slope is computed as the standard deviation of the weighted samples

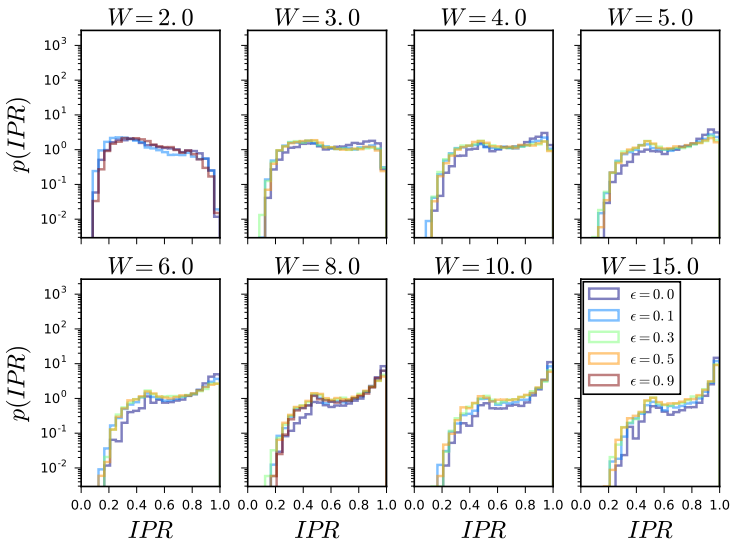

Figure 3.8: Distribution of IPR for $L = 32$.

ergodic and MBL phase. Interestingly, while the eigenstates we consider at low energy density ($\epsilon = 0.1, 0.3$) are in the MBL phase (see Fig. 3.1), we find a peak at $W \approx 4$ near the critical disorder strength W_c at the nose of the mobility edge. Furthermore, this peak is caused primarily by the standard deviation of the IPR within each eigenstate, rather than across eigenstates or disorder realizations. This result suggests the possibility that MBL eigenstates *know* whether they lie in the FMBL region of the phase diagram or instead lie below a mobility edge. The $\sigma(IPR)$ obtained from ground states also shows a peak, although at a lower value of W. $\sigma(IPR)$ at $\epsilon = 0.5$ is almost flat around the peak at W_c. Note also that the curves of $\sigma(IPR)$ are only weakly system size dependent for the disorder strengths considered, *i.e.* away from the $W = 0$ limit.

To better understand this peak in $\sigma(IPR)$ we can consider the full probability distribution of the IPR of the OPOs. As we see in Fig. 3.8, it follows a bimodal distribution. At large disorder, the distribution is peaked at 1.0 corresponding to most of the OPO's being highly localized; the secondary peak at 0.5 at large disorders corresponds to OPO's with their amplitude evenly distributed between two sites. At small disorder, for eigenstates in the MBL phase but deep below (or above) the mobility edge, there is a broad distribution of the OPO's with a maximum at small IPR; this suggests some orbitals are localized but the plurality of them are extended. The distribution presents its maximum spread (and most apparent bimodality) between $W = 3$ and $W = 4$, *i.e.* around W_c, in agreement with the peak in $\sigma(IPR)$ (Fig. 3.7). As with the averaged IPR and $\sigma(IPR)$, the distribution's behavior is independent of ϵ, although it slightly drifts towards higher values of the IPR for ground states. In addition, there is system size independence

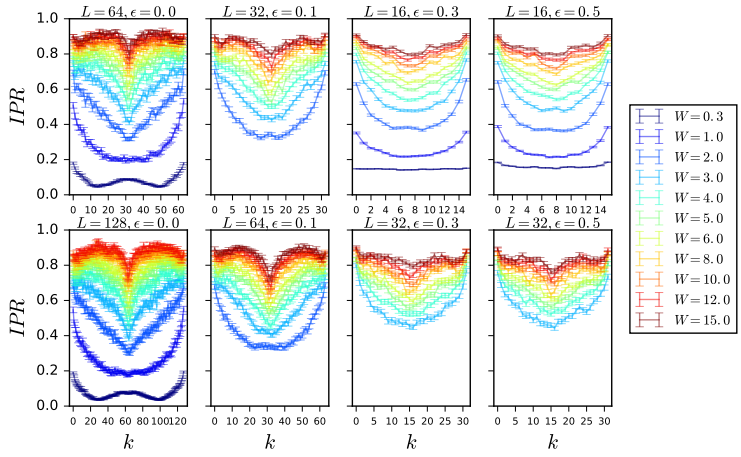

Figure 3.9: IPR as a function of k, *i.e.* as a function of OPOs ordered by occupation, averaged over OPOs. The shapes of the curves are characteristic of, respectively, strong disorder eigenstates, eigenstates around the critical disorder strength W_c and weak disorder, independent of ϵ.

(see Fig. D.1 in Appendix D) at the W's considered; presumably though, in the $W = 0$ limit, the IPR would collapse to $1/L$. The bimodality observed here is similar to the bimodality of the distribution of the entanglement entropy at half-cut around the transition found in Ref. [106]. Unlike in Ref [106], where the bimodality of the entanglement entropy is only studied at $\epsilon = 0.5$, here different values of ϵ are studied; because the distribution of the IPR is independent of ϵ, we can identify a transition from MBL eigenstates at small ϵ deep below the mobility edge and far from the transition (see Fig. 3.1).

The bimodality of the distribution of the IPR of the OPOs of Fig. 3.8 is not visible in the distribution of the support of Fig. 3.6 of Section 3.6.1, although the distributions are broad in the transition region. Indeed, the IPR and the support measure different things. The IPR is very sensitive to the broadening of an OPO, but it can be insensitive to the size of its support. Take for example an OPO with its amplitudes equally distributed between two nearest neighbor sites; while the support of this OPO is very small, its IPR is equal to 0.5 (we attribute the bump found in the IPR at 0.5 for strong W in Fig. 3.8 and 3.10 to this). At the same time, if the OPO's amplitudes are distributed evenly over two distant sites, its IPR is still 0.5, but its support is large. This explains why the bimodality found in the IPR does not imply a bimodal distribution of the support, however the broad distribution of the support confirms the coexistence of localized and extended OPOs in the transition region below the mobility edge.

We now analyze the correlation of the IPR of an OPO with its occupation. In Fig. 3.9 we present the average IPR of the OPOs as a function of OPO number k, which are ordered by increasing occupation n_k. We find curves have higher IPR at low and high occupations (close to 0 and 1) as compared to intermediate occupations (which are near the gap in the occupation spectrum). Both the very strong and very weak

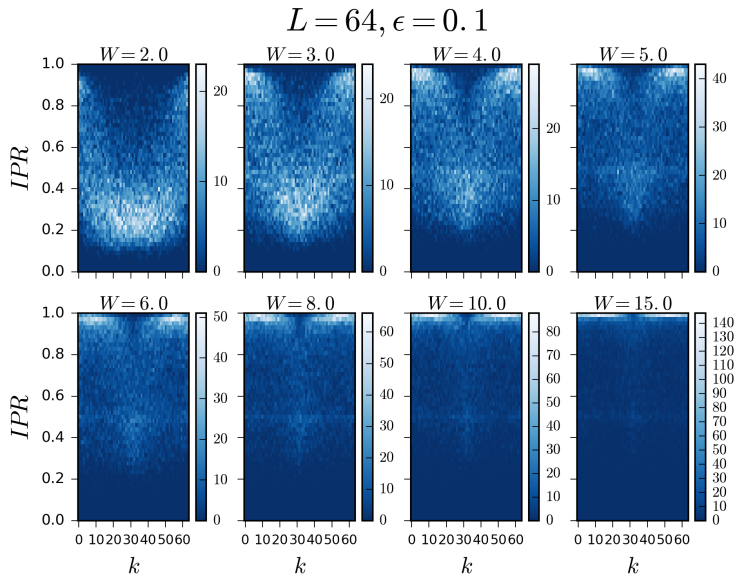

Figure 3.10: 2D histogram of the IPR of the OPOs vs. k for $L = 64$, $\epsilon = 0.1$. It is easy to see the emergence of the characteristic curves presented in Fig. 3.9. At strong disorder, intermediate values of k have an IPR close to 0.5 (see Fig. 3.8).

disorder IPR curve is largely flat with an exception at occupation near the very middle of the spectrum in large systems where there is an inverted peak. These OPOs in the middle of the spectrum have occupations away from 0 or 1, even for fairly strong disorder, as can be seen in Refs. [13, 14] and in Fig. 3.14. For intermediate disorder strengths there is significant curvature around the critical disorder strength W_c.

Fig. 3.10 shows the distribution of the IPR vs. k for a system of size $L = 64$ at an energy density $\epsilon = 0.1$. The appearance of the inverted peak at strong disorder results from the orbitals with an IPR of 0.5, which accounts for the secondary peak seen in Fig. 3.8 at strong disorder, and which correspond primarily to OPOs with amplitudes evenly distributed between two (usually nearby) sites. This correlation between the IPR and k will be discussed further in Section 3.6.3.

3.6.3 OPOs at different energy densities

Motivated by the suggestive picture that OPOs represent approximately the one particle operator content of the l-bits, we expect that the OPOs of different eigenstates are very similar, since they originate from the same set of l-bit operators. To test this simple picture, we compute the matrix of overlaps $M_{\text{overlap}} = |\langle \phi_k(\epsilon_1) | \psi_l(\epsilon_2) \rangle|$ between the OPOs of two different eigenstates of the same Hamiltonian at different energy densities $\{\epsilon_1, \epsilon_2\}$ (see Fig. 3.11 for a prototypical example). We find high overlap between OPOs drawn from different eigenstates. After ordering OPOs by their occupation, we can consider which OPO's of one

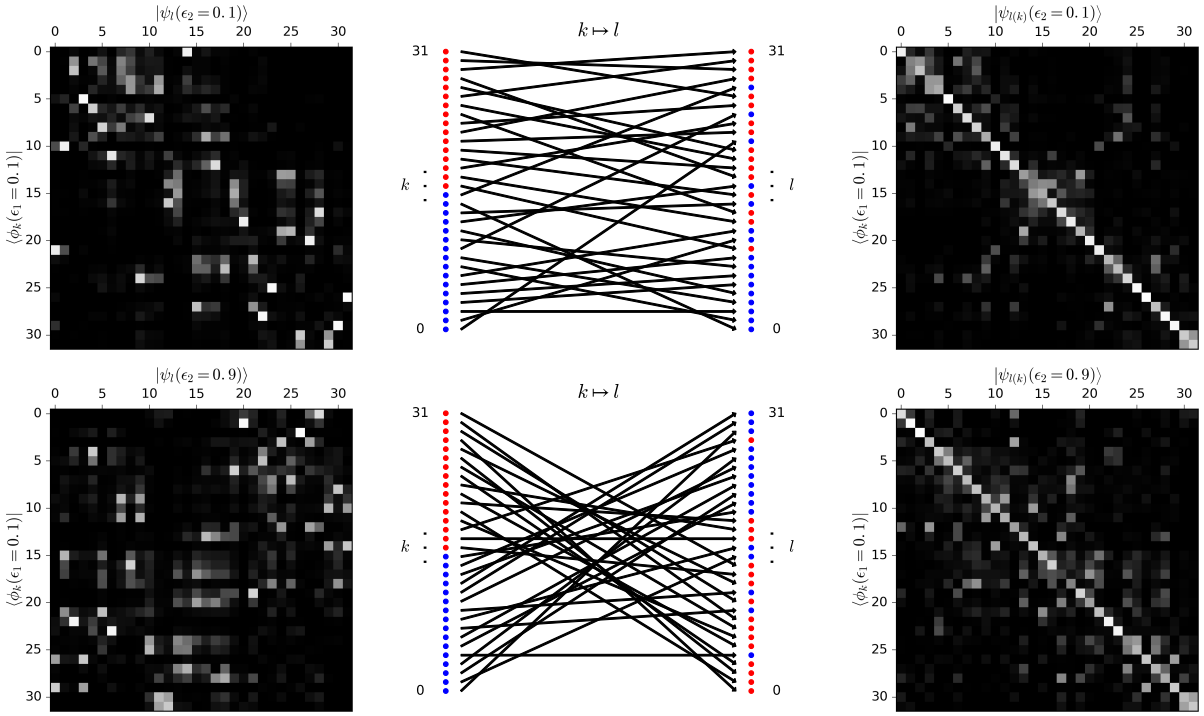

Figure 3.11: *Left:* matrix of overlaps $M_{overlap} = |\langle\phi_k|\psi_l\rangle|$ between the OPOs of two different eigenstates with $W = 2$ at energy densities ϵ_1 and ϵ_2, for a system of size $L = 32$. *Middle:* permutation between OPOs of the two eigenstates, $k \mapsto l$. The coloring on the left column is red for the half of the OPOs that have highest occupation and blue for the half with lowest occupation. The coloring on the right is inherited from the color of the OPO on the left to which it is mapped. *Right:* matrix of overlaps $M_{overlap}$ with the columns ordered after the permutation shown by the middle diagrams.

eigenstate map to OPO's of another eigenstate. This is accomplished by finding the permutation of columns of M_{overlap} which makes it maximally diagonal (see Fig. 3.11). Note that for two different eigenstates at a similar energy density, the permutation is close to the identity, with highly occupied orbitals mapping to other highly occupied orbitals. However, for eigenstates at opposite sides of the energy spectrum the permutation essentially swaps highly occupied and unoccupied orbitals. Fig. 3.12 shows a disordered average version of this behavior even from OPO's generated from the ground state.

The top panel of Fig. 3.13 shows the distribution of overlaps $\left|\left\langle\phi_k\left(\epsilon_1\right)|\psi_{l(k)}\left(\epsilon_2\right)\right\rangle\right|$ between matching pairs of OPOs for eigenstates at different pairs of energy densities $\{\epsilon_1, \epsilon_2\}$. At moderate disorder ($W = 8$) we find that the overlaps are extremely high and largely independent of ϵ_1 and ϵ_2. Note that in the strong disorder limit all overlaps should be 1. For $W = 2$, the magnitude of the overlaps decreases, but it is still surprisingly high; there is now a dependence on the energy densities, with better overlaps for $\epsilon_1 \approx \epsilon_2$. The typical overlap between matching pairs of OPOs is represented by the mode of the distribution, which is shown in the bottom panel of Fig. 3.13 to be extremely close to 100% at moderate and strong disorder as

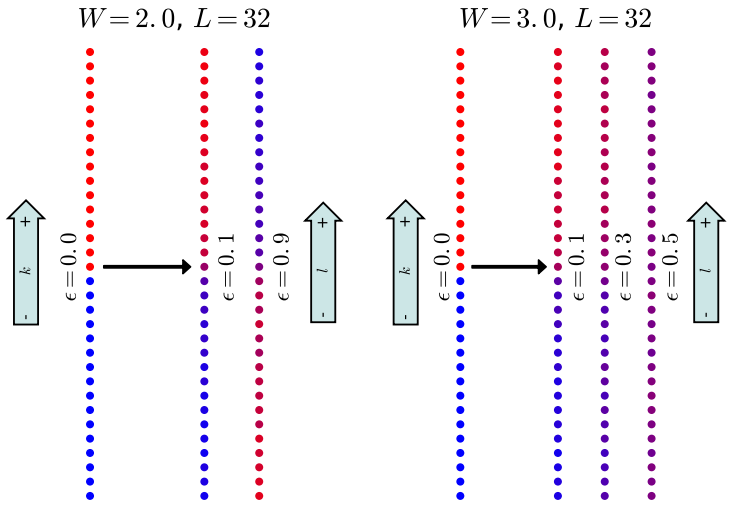

Figure 3.12: The coloring on the left column is red for the half of the OPOs that have highest occupation and blue for the half with lowest occupation. The coloring on the right is the disordered average of all colors inherited from the OPO on the left to which it is mapped (see Fig. 3.11 (middle) for a non-averaged version of this). The closer the eigenstate energies are to each other, the more likely the occupations of the OPOs of two eigenstates will be preserved, ranging from a few swaps in occupation when the energies are close in the spectrum to almost all swaps when the energies are in opposite sides of the spectrum.

well as small disorder when $\epsilon_1 \approx \epsilon_2$. At $W = 2$ it falls to 70% for ϵ_1 far from ϵ_2 and at $W = 1$ is drops below 70% for all $\{\epsilon_1, \epsilon_2\}$ and $L = 16$. It should be noted that this strong overlap is not just caused by the fact that OPO's are generally centered on a site (see Appendix E for further analysis and discussion). Notice also that the OPOs have high overlap even in the ergodic phase (for $L = 16$).

The OPOs can be regarded as an approximate version of a set of integrals of motion of the system: the high overlap between OPOs at different energy densities lets them acquire universality across the spectrum, and each eigenstate carries a particular permutation (correlated to its energy density) of the occupations of the OPOs. It is interesting that this occupation dependence doesn't seem to be apparent in the results of Fig. 3.9 of Section 3.6.2 where the behavior as a function of occupation order k is independent of energy density. This suggests that both metrics are probing different aspects of the OPOs: the IPR is sensitive to small broadening of the OPOs to which the overlap is primarily insensitive. Note also that those slightly broader OPOs are closer to the center of the occupation spectrum, and have therefore a less well defined occupation than the rest of the OPOs, contributing to the breakdown of the one particle approximation of the integrals of motion.

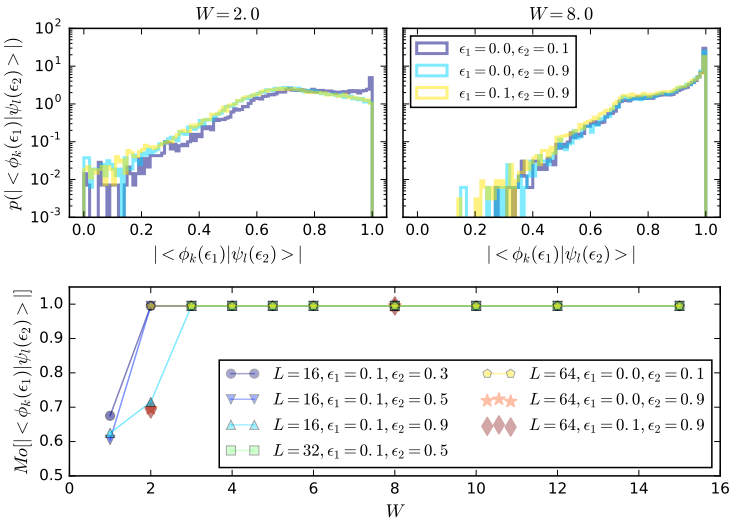

Figure 3.13: *Top:* distribution of overlaps $|\langle\phi_k(\epsilon_1)|\psi_{l(k)}(\epsilon_2)\rangle|$ between corresponding OPOs of eigenstates at energy densities ϵ_1 and ϵ_2 ($L = 64$). *Bottom:* mode of the distribution of overlaps of corresponding OPOs.

3.6.4 Occupations of the OPOs

The gap in the occupations of the OPOs, $\Delta n \equiv n_{L/2} - n_{L/2-1}$, serves as a proxy for the characterization of the ergodic and the MBL phases, as shown in Refs. [14] and [13]. An MBL system presents a large gap, which becomes smaller entering the ergodic phase and vanishes in the small disorder limit. This is in agreement with our results for large systems (see left panel of Fig. 3.14) in the MBL phase. Notice that for all values of W the gap is smaller closer to the middle of the spectrum for fixed L, which agrees with the existence of a mobility edge. In addition, for fixed W and ϵ, the gap decreases with system size, which is also in agreement with the usual numerical results, which point to the fact that the ergodic region of the phase diagram penetrates further into large disorder strengths for larger system sizes. It is still unknown whether the gap Δn closes at the transition in the thermodynamic limit, while remaining finite in the MBL phase; the right panel of Fig. 3.14 (which includes further ED data for small systems) is suggestive of this behavior.

3.6.5 Standard deviation of the entanglement entropy

At the MBL transition, the nature of many-body eigenstates changes radically, which is clearly signaled in the different scaling behavior of the entanglement entropy: while in the MBL phase almost all eigenstates have an area law entanglement entropy (EE), in the thermal phase, the EE is extensive. It has been demonstrated that the change of this behavior leads to a coexistence of area law and volume law states at the transition [44, 47, 60, 106], which is signaled by a bimodal distribution of the entanglement entropy S

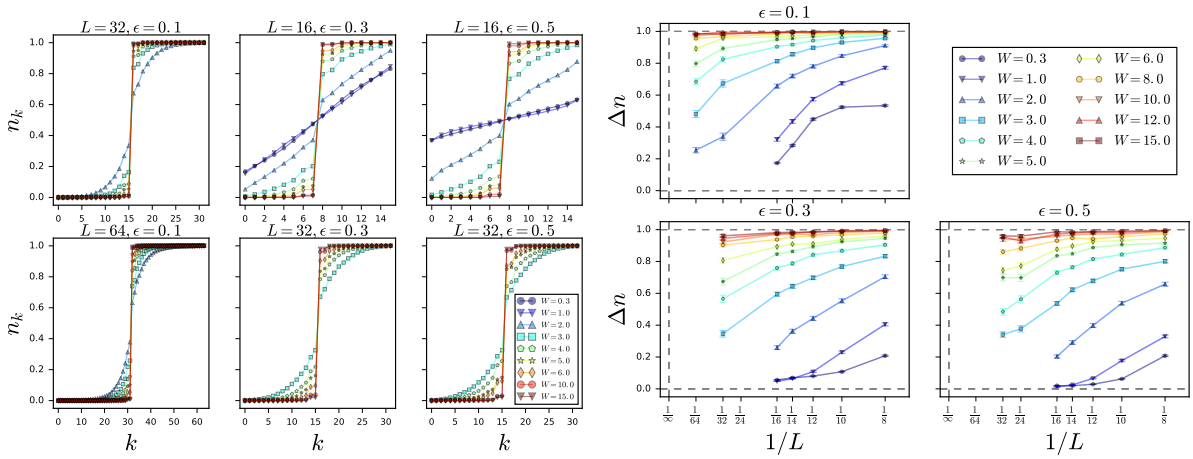

Figure 3.14: *Left:* average occupations n_k of the OPOs. The error bars have been removed for clarity; they are of the order of those of the gap Δn (Right). All eigenstates accessed by SIMPS are in the MBL phase, and so the occupation spectrum of the OPOs shows a finite gap [13, 14]. *Right:* scaling of the gap $\Delta n \equiv n_{L/2} - n_{L/2-1}$ as a function of $1/L$.

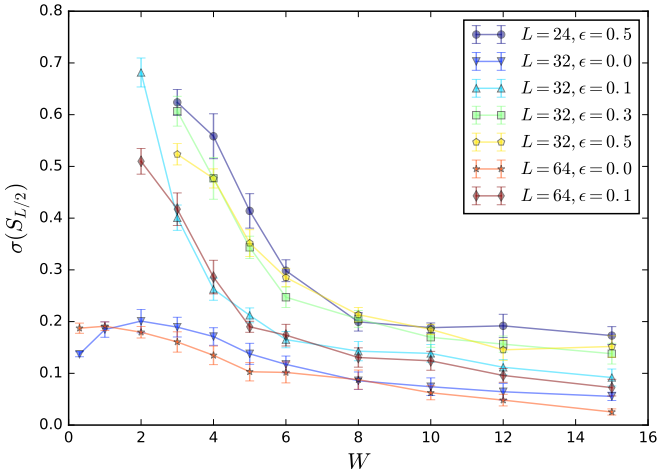

Figure 3.15: Standard deviation of the entanglement entropy of the half system $\sigma\left(S_{L/2}\right)$ as a function of disorder strength W for different system sizes and energy densities. $\sigma\left(S_{L/2}\right)$ exhibits a maximum at each energy density close to the transition point [47]. Our results for the finite energy eigenstates considered in this article accessed by SIMPS only show the approach to this maximum.

and, consequently by a peak of the standard deviation $\sigma(S)$ at the critical point. Using SIMPS, we only have access to eigenstates at the MBL side of the transition and therefore can only observe the approach to the peak in $\sigma(S_{L/2})$ (at half-cut) in Fig. 3.15. In addition, the EE, even for states of small $\sigma(E)$, is likely to be much more sensitive than other observables to the finite bond dimension used in the SIMPS calculations; this probably explains the inverted system size and energy density dependence of $\sigma(S_{L/2})$ at low W. Our results are consistent with the existence of a mobility edge, since it is apparent that the peak is located at

different disorder strengths for different energy densities.

3.7 Conclusion

In this work we study the properties of the eigenstates, particularly of their OPDM, of the model in Eq. (3.1) deep into the mobility edge using the SIMPS algorithm [107].

These SIMPS eigenstates give us various ways to probe the MBL transition. Interestingly enough, even the phase points at which SIMPS (restricted to small bond-dimensions) succeeds or fails (see Fig. 3.2) gives evidence for the location of the transition. We can even identify the mobility edge by noting the ϵ dependence of the rate of failure of SIMPS and of the apparent divergence of the bond dimension of the eigenstates, as well as seeing that SIMPS successfully computes eigenstates at $W < W_c$ for small and large ϵ (see Fig. 3.1). The location of the transition can further be bounded using the approach to the peak in $\sigma(S_L/2)$ (see Fig. 3.15) and the closing gap of the eigenvalues of the OPDM (see Fig. 3.14); both of these measures suggest that at low ϵ the transition happens at $W < W_c$. Using the decay of either the OPOs or the number operators $a_k a_k^\dagger$ generated from them, we can define a correlation length. As we approach the transition the correlation length gets larger but does not obviously diverge. For small systems, we could probe this correlation length even within the ergodic phase; we find that deep in the MBL or ergodic phase the correlation length has a little ϵ dependence, while there is significant dependence on ϵ in the mobility edge.

Beyond probing physics near the transition, we can also use the OPDM to further elucidate properties about the MBL phase itself. Within the MBL phase, we see a clear but small increase in the correlation length with system size (see inset of Fig. 3.4). Moreover, we consider the probability distribution of the magnitude of the coefficients f_{ij}^k (from Eq. (3.4)) and find that deep within the MBL phase and at large range R (defined in Eq. (3.5)) it approaches a "$1/f$" distribution (see Fig. 3.5). This behavior, which we observe for the coupling constants of the number operators of the OPOs, is the same one shown in Ref. [71] for the coupling constants of the Hamiltonian written in the l-bit basis.

Interestingly, we are also able to identify properties of the entire spectrum using MBL eigenstates at single points in the spectrum. This is possible because, surprisingly, a single MBL eigenstate provides a 'universal' set of OPOs (i.e. they have significant overlap with the OPOs generated from eigenstates at different energy densities (see Fig. 3.13)). While the OPOs at different energy densities have high overlap, the OPDMs are very different. This difference comes from a change in the occupations of the OPOs among the eigenstates. There is correlation between the energy of the eigenstates and which OPOs have high occupation; for

example, the set of high and low occupied OPOs at $\epsilon = 0.1$ and $\epsilon = 0.9$ are almost completely flipped (see Figs. 3.11 and 3.12).

We show that the $\sigma(IPR)$ has a peak, for multiple ϵ, at $W \approx 4$ (see Fig. 3.7), suggesting that even MBL eigenstates deep under the mobility edge are aware of the presence or absence of an ergodic phase at a higher value of ϵ.

The use of SIMPS allows us to access MBL eigenstates of systems of size beyond those accessible by other techniques, even deep into the mobility edge. By looking at the OPDM we are able to study the one particle approximation to the integrals of motion. Despite its approximate nature, and the limitations of working with an MPS approach (with difficulty in probing the ergodic region of the phase diagram), our study leads to phenomenological conclusions that are not accessible from exact diagonalization techniques or an exact treatment of the integrals of motion. We think that the study of the MBL transition, as well as other problems, can benefit greatly from this promising approach.

Chapter 4

Eigenstate collisions break down locality at the many-body localization transition

This chapter is mainly based on Ref. [96].

4.1 Introduction

Certain disordered interacting systems can support the many-body localized (MBL) phase. An ergodic system transitions to MBL under the presence of sufficiently large disorder, breaking ergodicity and defying thermalization in the process [11, 34, 35, 59, 63, 79]. An MBL Hamiltonian, such as the one-dimensional disordered Heisenberg model with large disorder, can be diagonalized by a unitary operator U which can be expressed as a low-depth quantum circuit. This implies that the eigenstates of the MBL phase have an area law of entanglement across the system, *i.e.*, they are disentangled and consequently brought back to product states through few local transformations. As the strength of the disorder W of the Hamiltonian is continually decreased, the system eventually transitions out of the MBL phase and back into the more generic ergodic phase, presenting a volume law of entanglement across the system, whose Hamiltonian can only be diagonalized through a unitary U which is now written as a quantum circuit whose depth grows linearly with the size of the system (L).

For a spin-$\frac{1}{2}$ system, the L two-level Hermitian operators $\tau_i^z \equiv U\sigma_i^z U^\dagger$ commute with the Hamiltonian and with each other; although this is true for any spin Hamiltonian H, in the case that H is MBL these operators have local support (and are called local bits, or l-bits) and can be interpreted as locally dressed spins, or pseudo-spins. L-bits have been a key quantity in understanding the phenomenology of the MBl phase [40, 70, 70, 75, 86]. As a prominent property of the l-bits, we can identify each eigenstate $|n\rangle$ of H by the L pseudo-spins corresponding to the eigenvalues of the L l-bits $\{\tau_z^i\}$. Alternatively, these eigenvalues correspond to the spin configuration of the product state generated by $U^\dagger |n\rangle$.

While many aspects of the MBL phase are well understood, much less is known about the transition. In this work, we will probe the hybridization of eigenstates into each other as the disorder strength W is tuned from large disorder, through the transition, and into the ergodic phase. As disorder is tuned, some

eigenstates will approach each other in energy, "colliding" amongst themselves. In this collision, eigenstates temporarily hybridize, inducing changes in their properties. This hybridization occurs over a region of a certain range, or size. Interestingly, the probability that hybridization occurs at a certain rate and over a particular range changes drastically between the MBL and the ergodic phases. Strikingly, this probability presents distinct behavior at the transition, where it becomes range independent. This range invariance ultimately allows us to observe a diverging localization length, ξ, which is otherwise finite in the MBL phase.

Deep in the MBL phase, it is relatively straightforward to understand this process through first-order perturbation theory. As we tune the disorder strength W by ΔW, the off-diagonal Hamiltonian term between two eigenstates (close in energy) $|m\rangle$ and $|n\rangle$ (H_{mn}) is only a small perturbation proportional to ΔW; for these two states to collide and hybridize strongly, the product $H_{mn}\Delta W$ must be comparable to the energy gap between them. Given that l-bits are exponentially localized, two eigenstates $|m\rangle$ and $|n\rangle$ that differ in l-bit eigenvalues over a region of range R provide an off-diagonal H_{mn} that is exponentially supressed with R, and collisions at large R are very rare events. This supression of long-range hybridization preserves localization of the eigenstates as they are driven within the MBL phase by tuning down the disorder strength. [1] Moreover, the rarity of collisions leads to infrequent level repulsion in MBL phases, inducing Poisson level statistics on the eigenenergies, which is a defining feature of MBL [59, 62, 64, 67, 85].

Deep in the ergodic phase, strong collisions must become much less rare, with continuous hybridization generating Gaussian Orthogonal Ensemble (GOE) level repulsion [59,62,64,67,85]; the absence of locality in the ergodic phase suggests there should be no reason for collisions of small range to be higher in probability. In fact, large range R collisions should be exponentially more likely, due to combinatorial counting. It turns out that a simple combinatorial argument precisely describes the scaling of the probability of strong collisions as a function of range.

The key result of this work is numerically demonstrating that strong collisions at the MBL-ergodic transition are range-invariant, *i.e.*, the probability that two eigenstates hybridize over a region of range R is constant across ranges. This differs from the MBL and the ergodic phases. In fact, this range invariance observed over several orders of magnitude in collision strength.

We also show that in MBL, the probability of colliding (at fixed R) with a given strength decays as a power law with strength. We show that this algebraic decay characteristic of the MBL phase comes from two-eigenstate avoided level crossings, suggesting that hybridization in the MBL phase is dominated by sporadic pair-wise collisions. On the contrary, ergodic eigenstates are continuously hybridizing through

[1] Note that every eigenstate is labelled by a bitstring with all eigenvalues of the l-bits, each taking the value $\uparrow$ or $\downarrow$. Given two states, it is straight forward to obtain the set of sites for which their eigenvalues disagree.

overlapping processes, which are due to weaker yet continuous collisions. The combination of both range independence and pair-wise collisions as eigenstates approach the transition from the MBL side suggests the transition coincides with the proliferation of resonating long-range cat states coming from the hybridization over regions of the system at all scales.

4.2 Model

In this work we focus on the so called standard model of MBL in one dimension, *i.e.*, a spin-$\frac{1}{2}$ nearest-neighbor antiferromagnetic Heisenberg chain with random onsite magnetic fields:

$$H = \frac{1}{4}\sum_{i=0}^{L-2} \vec{\sigma}_i \cdot \vec{\sigma}_{i+1} - \frac{W}{2}\sum_{i=0}^{L-1} h_i \sigma_i^z. \tag{4.1}$$

The on-site magnetic fields $\{h_i\}$ are sampled uniformly at random from $[-1, 1]$ and W is the disorder strength. The model of Eq. (4.1) has been studied extensively in the context of MBL [4, 8, 12, 14, 15, 30, 38, 44, 46, 54, 55, 57, 59, 60, 64, 67, 85, 106, 110], both in the form presented here as well as a chain of spinless fermions with nearest-neighbor repulsion. This model presents an ergodic-MBL transition at infinite temperature (middle of the energy spectrum) at a critical $W \approx 3.8$ [59]. The critical W_c is typically estimated numerically through different methods, all of them involving finite size scaling from small systems, where exact diagonalization is possible. Numerical simulations also suggest a transition W that varies with energy, forming a mobility edge [59, 97]. This Hamiltonian conserves total magnetization $\sum_i \sigma_i^z$; throughout this work we focus on the zero magnetization sector.

4.3 Local integrals of motion

Given a closed quantum system, it is always possible to find a complete set of commuting observables (CSCO), or integrals of motion, which commute with one another and with the Hamiltonian H. For MBL systems, there exists a CSCO of *local* integrals of motion [40, 71, 75]. These integrals of motion, which have the form of locally dressed spins, are usually referred to as l-bits, are denoted by $\{\tau_i^z\}_{i=0,\ldots,L-1}$, where L is the system size, and are defined by construction as:

$$\tau_i^z \equiv U \sigma_i^z U^\dagger, \tag{4.2}$$

where U is a unitary matrix that diagonalizes H. Eq. (4.2) guarantees all required commutation relations trivially. Note that given a unitary U that diagonalizes H, all unitaries generated by permuting the columns of U also diagonalize H. Making the right choice of U is essential to construct the most localized possible set of l-bits from Eq. (4.2). While finding the optimal U is not efficiently solvable, the Wegner-Wilson flow approach described in Ref. [71] gives good results in practice. In the present work, we always refer to the set of operators $\{\tau_i^z\}$ and to the unitary U found by this method.

Given a complete set of l-bits, a spin Hamiltonian H over L sites can be expanded as follows [40]:

$$H = \sum_{i_0=0}^{L-1} f_{i_0}^{(1)} \tau_{i_0}^z + \sum_{i_0,i_1=0}^{L-1} f_{i_0 i_1}^{(2)} \tau_{i_0}^z \tau_{i_1}^z + \sum_{i_0,\ldots i_{L-1}=0}^{L-1} f_{i_0,\ldots i_{L-1}}^{(L)} \tau_{i_0}^z \ldots \tau_{i_{L-1}}^z, \tag{4.3}$$

i.e., H is explicitly diagonal in the basis of l-bits. Any eigenstate of H is therefore a product state in the basis of l-bits and can be labelled as a string of up and down pseudo-spins: $|n\rangle = |\uparrow\downarrow \ldots \downarrow\uparrow\rangle_\tau$, where $|n\rangle$ is an eigenstate of H and the subscript τ denotes that the specified arrows refer to quantum numbers given by the eigenvalues of $\{\tau_i^z\}_i$.

4.4 Adiabatic evolution of $|n(W)\rangle$ and range R hybridization

Given a fixed disorder realization, *i.e.*, a set of randomly sampled magnetic fields $\{h_i\}$, the model of Eq. (4.1) defines a Hamiltonian with disorder strength W, $H(W)$. By varying W adiabatically, we can drive an eigenstate from an ergodic phase at weak disorder through the transition and into the MBL phase at strong disorder. We work in the zero-magnetization sector. In such an adiabatic evolution, the n^{th} eigenstate of $H(W)$ will remain in n^{th} position for all disorder strengths along the path; we denote this eigenstate $|n(W)\rangle$.

Given a differential change in W, $W \to arrow W + dW$, we induce the trajectory $|n(W)\rangle \to |n(W+dW)\rangle$, in which the eigenstate slightly rotates in Hilbert space. In the basis of eigenstates of $H(W)$, $\{|k(W)\rangle\}$, we can now write $|n(W+dW)\rangle = \sum_k^{\dim(H)} c_k^n |k(W)\rangle$, where $\sum_k^{\dim(H)} (c_k^n)^2 = 1$, due to normalization. Alternatively, $c_n^n = 1 - A_n^n (dW)^2$ and $c_k^n = A_k^n dW$ (for $k \neq n$), with $A_n^n = \sqrt{\sum_{k\neq n}^{\dim} (A_k^n)^2}$ up to second order in dW. We call A_k^n, with $k \neq n$, the *hybridization ratio* of $|n(W)\rangle$ with $|k(W)\rangle$. Note that $(A_k^n dW)^2$ could also be thought of as a transition probability from $|n(W)\rangle$ to $|k(W)\rangle$.

We now define the spatial range associated to a pair of eigenstates $|n(W)\rangle$ and $|k(W)\rangle$. To do so, we look at the difference in their quantum numbers, *i.e.* their eigenvalues with respect to the l-bit operators $\{\tau_i^z\}$. We say that two eigenstates of a spin Hamiltonian H, $|n\rangle$ and $|k\rangle$, have a difference of range R if the left-most and the right-most disagreeing quantum numbers between the two are R pseudo-sites away from each other. For example, eigenstates $|n(W)\rangle = |\uparrow\downarrow\downarrow\uparrow\downarrow\uparrow\rangle_\tau$ and $|k(W)\rangle = |\uparrow\uparrow\uparrow\downarrow\downarrow\downarrow\rangle_\tau$ differ on a region of range

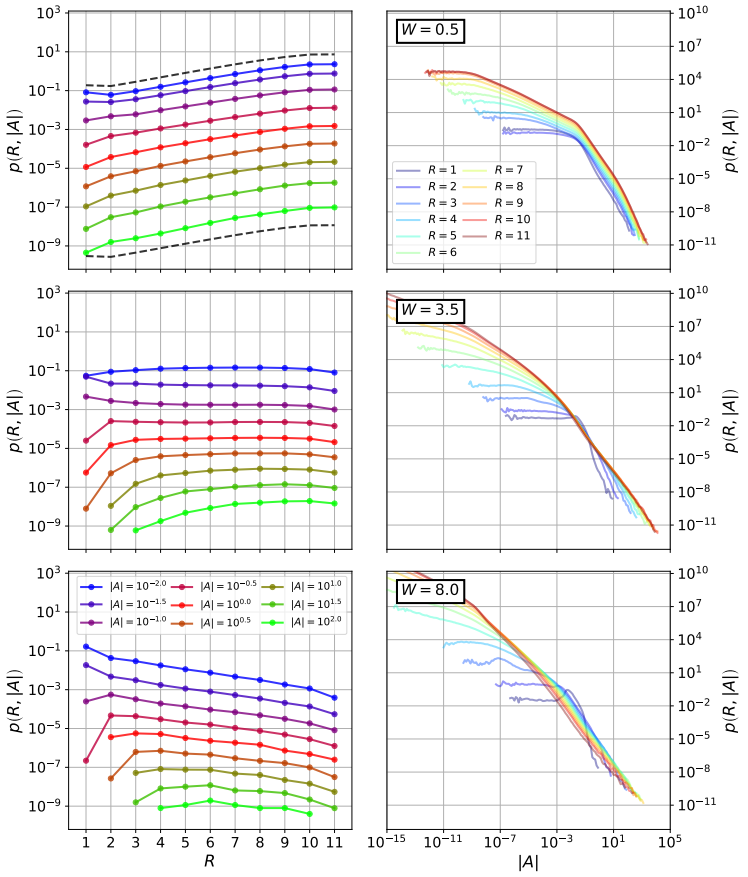

Figure 4.1: Probability $p(R, |A|)$ that two eigenstates hybridize over a region of range R with hybridization ratio $|A|$, for all pairs of eigenstates over 1024 different disorder realizations on a chain of size $L = 12$. We can observe three distinct behaviors. In the ergodic phase ($W = 0.5$) contributions from long ranges are dominant due to a simple combinatorial argument. At the transition ($W = 3.5$) all ranges contribute equally, and distributions collapse to a universal curve at large enough strength and range. In the MBL phase ($W = 8.0$), short range domininates, which is in line with the concept of localization.

$R = 4$ (between the second and the sixth pseudo-spins); for simplicity, we will say that the two states are a range $R = 4$ away from each other. While pseudo-spins are not exactly spins on real space, they are locally dressed spins in the MBL phase, and so the notions of distance in real space and in the space induced by l-bits are nearly identical.

When two eigenstates collide (*i.e.*, avoid a level crossing) with each other, it is their disagreeing pseudo-spins that hybridize, while all other pseudo-spins remain frozen in their configuration, which is common to both states. This hybridization drives them towards the formation of a cat state across a region of range R, which disentangles as the state collision passes. We are interested in the joint probability that a pair of eigenstates $|n(W)\rangle$ and $|k(W)\rangle$ hybridize over a region of range R with a hybridization ratio of magnitude $|A_k^n|$, $p(R, |A|)$.

Fig. 4.1 shows $p(R, |A|)$ obtained for all pairs of eigenstates $|n(W)\rangle$ and $|k(W)\rangle$ ($k \neq n$) in the zero-magnetization sector over 1024 disorder realizations, for a system of size $L = 12$. The left column of Fig. 4.1 shows slices of $p(R, |A|)$ at constant hybridization ratio $|A|$ as a function of range R, for moderate and strong values of $|A|$, while the right column shows slices at constant R as a function of $|A|$. In the ergodic phase ($W = 0.5$), the probability that a pair of eigenstates hybridizes strongly over a region of range R, $p(R, |A|)$, increases exponentially with R. This probability simply mimics the average number of zero-magnetization pseudo-spin configurations that, given a random configuration, differ from it on pseudo-spins over spanning a region of size R; in the thermodynamic limit, this scales as 2^R, while for finite systems the scaling is slightly different (see Appendix G). This suggests that the notion of locality is completely lost and hybridization occurs in a way that is independent of the details of each configuration and, in particular, of R. Deep in the MBL phase ($W = 8.0$), the probability $p(R, |A|)$ is suppressed exponentially for larger ranges; this is expected from the exponential localization of the l-bits, which leads to an off-diagonal (local) Hamiltonian term between the eigenstates ($\langle n(W)| H(W + dW) |k(W)\rangle$) that decays exponentially with the size of the region spanned by the disagreeing (hybridizing) l-bits. Around the transition ($W = 3.5$), surprisingly, strong hybridization is range independent, *i.e.*, $p(R, |A|)$ is range independent at strong values of $|A|$. There is a subtlety (see right columnn of Fig. 4.1 for reference) in this range independence: for each R, there is a cuttof in $|A|$ after which $p(R, |A|)$ drops the universal, range-independent behavior; the larger R, the larger the cutoff. We can now rephrase the range independence claim in a more precise way: given a value of $|A|$, there is a minimum range R above which the probability of hybridization is range independent. This range independence of strong hybridization processes requires of a non-trivial balance between (1) the exponential growth of $p(R, |A|)$ due to long range hybridization being combinatorially dominant in the ergodic phase and (2) the suppression of long-range hybridization which dominates the MBL phase.

4.5 The localization length ξ

The top panel of Fig. 4.2 shows the exponent α of the scaling of $p(R, |A|) \propto 2^{\alpha R}$ for fixed strength of the hybridization ratio $|A|$. As expected, the exponent α is positive in the ergodic phase, crosses zero around the transition (range invariance), and becomes negative in MBL. At weak disorder α approaches its theoretical combinatorial value (see Appendix G), which is represented for eac system size by a dashed line; in the thermodynamic limit, this value is equal to 1. We define the pseudo-critical disorder strength ($W_c(L)$) as the value of W for which $\alpha = 0$, *i.e.*, the disorder strength at which we find scale invariance; $W_c(L)$ is marked with stars. The inset shows α as a functin of W in a semi-log plot. We can see that for $W > W_c(L)$

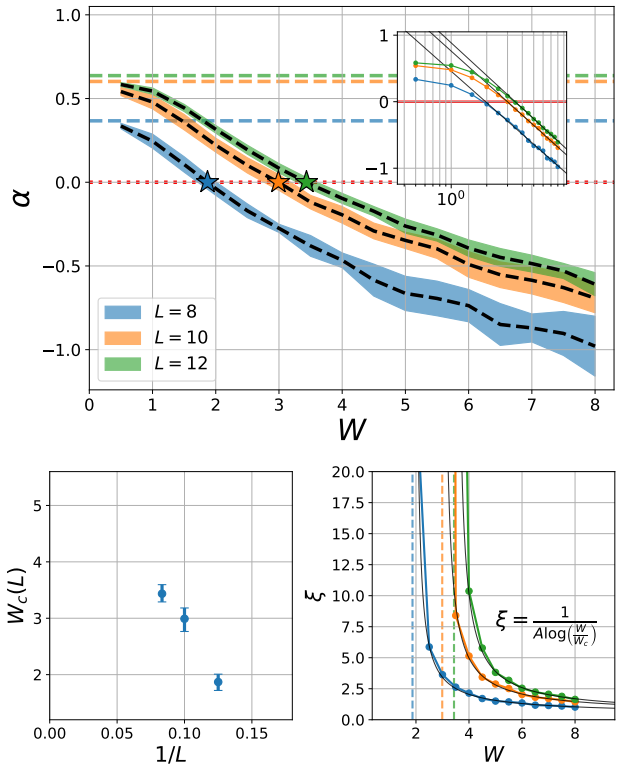

Figure 4.2: **Top:** exponent of the scaling of $p(R, |A|) \propto 2^{\alpha R}$ at constant $|A|$ (see left panel of Fig. 4.1) for systems of size $L = 8, 10, 12$. We compute α by averaging the slope obtained from a linear fit of $\log_2(p(R, |A|))$ as a function of R, for all values of $|A|$ in the interval $[10^{-3}, 10^1]$ ($[10^{-3}, 10^0.5]$ for $L = 8$); errorbars correspond to the standard deviation of this set of slopes. At the pseudo-critical point $W_c(L)$, $\alpha = 0$ due to range invariance. In the thermodynamic limit we expect $\lim_{L\to\infty} \alpha \to 1$ deep in the ergodic phase; at finite L, α approaches smaller values (dashed lines). The inset shows a fit to of the form $\xi = -A \log(\xi) + B$ for $W > W_c(L)$. **Bottom left:** W_c as a function of $1/L$. An extrapolation of these values would give a critical W_c in the thermodynamic limit which is slightly higher than typical estimates. **Bottom right:** localization length $\xi = \frac{1}{-\alpha}$. ξ diverges at W_c as $\xi = \frac{1}{A \log\left(\frac{W}{W_c}\right)}$.

the exponent α scales as $\alpha = -A \log\left(\frac{W}{W_c}\right)$; the linear fit is shown in black for all system sizes.

The bottom left panel of Fig. 4.2 shows the values of W_c as a function of $1/L$. We can see that a naive extrapolation of these values to the thermodynamic limit, $L^{-1} \to 0$, would provide a critical disorder strength higher than the estimates typically found in the literature ($W \approx 4$), and perhaps closer to that one of Ref. [36] ($W_c \gtrapprox 5$).

The exponent α has interpretation of an inverse localization (or correlation) length, $\xi = (-\alpha)^{-1}$. Interestingly, this localization length diverges as we approach W_c from the MBL phase: $\xi = \frac{1}{A \log\left(\frac{W}{W_c}\right)}$. The bottom right panel of Fig. 4.2 shows the divergence of ξ as a function of W; . Note that $W_c(L)$ (dashed vertical lines) drifts with L. The notion of a localization length that diverges at the transition has been elusive in the MBL literature. Here we grasp the concept of a diverging localization length by relying on

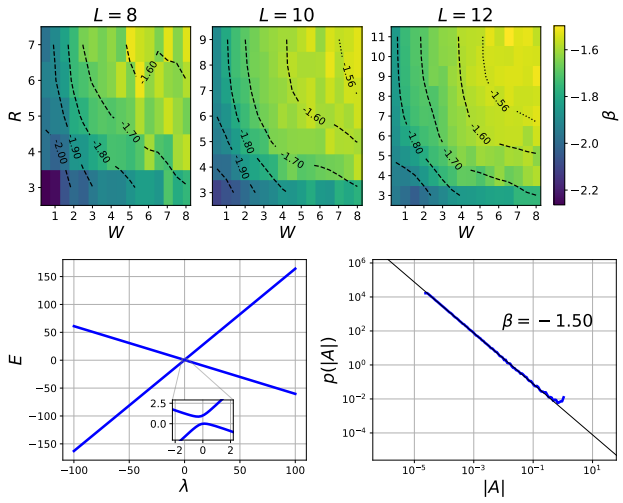

Figure 4.3: **Top:** colormap with the exponent β of the power law decay of $p(R, |A|) \propto e^{\beta|A|}$ strong $|A|$ for different values of R and W. We can see that $\beta \to -\frac{3}{2}$ at large R and strong W. **Bottom:** level collision of the two-level toy model $H_{\text{toy}}(\lambda) = H_0 + \lambda H_1$ and its corresponding $p(|A|)$. We recover the exponent $\beta = -\frac{3}{2}$, which suggests that strong, long-range hybridization in MBL are dominated by rare, pair-wise collisions.

a definition of range based on pseudo-spins, and therefore abandoning strict locality in favor a quasi-local, more convenient view of the system. Because we can approach the transition from the MBL side without ever abandoning quasi-locality, *i.e.* we can always find a complete set of l-bits while $W > W_c$, the interpretation of ξ as a localization length that diverges at the transition seems in place. After all, we are observing the divergence of ξ at $W = W_c$ form an quasi-local set of l-bits at $W + dW > W_c$.

4.6 Pair-wise collisions in MBL

We have already analyzed the exponential scaling of $p(R, |A|)$ for strong $|A|$ as a function of R. In this section we study its scaling with as a function of $|A|$ at strong disorder. In particular, we compute the exponent β of the power law decay of $p(R, |A|) \propto e^{\beta|A|}$, for large R, right before $p(R, |A|)$ hits the cutoff characteristic of each range R (see Fig. 4.1).

The top panel of Fig. 4.3 shows the values of β extracted from $p(R, |A|)$ for different as a function of W and R. We can see how at strong disorder W and larger range R $\beta \to -\frac{3}{2}$. This is indication that strong hybridization in the MBL phase are dominated by pair-wise collisions. In particular, $\beta = -\frac{3}{2}$ can be obtained from a toy two-level model $H_{\text{toy}}(\lambda) \equiv H_0 + \lambda$ for which two states $|1(\lambda)\rangle$ and $|2(\lambda)\rangle$ undergo a collision. As can be seen in the bottom panel of Fig. 4.3, by sampling hybridization ratios between $|1\rangle$ and $|2\rangle$, $|A| = |\langle 1(\lambda)|2(\lambda + d\lambda\rangle|$, uniformly uniformly at random over a large window in λ ($[-\lambda_m, \lambda_m]$), we precisely obtaine a probability distribution $p(|A|)$ that decays as a power law with exponent $\beta = -\frac{3}{2}$.

4.7 Conclusions

The key result of this work is the identification of range-invariant behavior at the ergodic-MBL transition. In particular, we have studied the hybridization of eigenstates of the model in Eq. 4.1 as we tune the disorder strength W from an MBL phase into an ergodic phase, therefore crossing the transition. More precisely, we have computed the probability that, given a pair of eigenstates, they hybridize with each other at a hybridization ratio $|A|$ over a subset of pseudo-spins (l-bits) that span a region of range R, $p(R, |A|)$. We find that strong hybridization happens in a range-invariant fashion. This is in contrast with the exponential suppresion of hybridization with range in the MBL phase, which preserves locality. Deep in the ergodic phase, hybridization is more likely at larger ranges; we explain this with a simple combinatorial argument: at large ranges there are exponentially more ways of hybridizing between two bit-strings.

Importantly, we define the localization length ξ as the inverse of the exponent $-\alpha$ that suppreses long-range hybridization in MBL. ξ diverges at the pseudo-critical point $W_c(L)$, which drifts with L. Our results suggest that $W_c \gtrapprox 5$ in the thermodynamic limit, in agreement with Ref. [36].

Finally, in MBL the probability $p(R, |A|)$ decays, at strong $|A|$ and large R as a power law in $|A|$ with an exponent $\beta = -\frac{3}{2}$. This indicates that strong, long-range hybridization in the MBL phase is dominated by rare pair-wise collisions. This is in agreement with the Poisson statistics found in the distributions of eigenenergies of an MBL system, which comes from the lack of level repulsion in such systems.

Chapter 5

Typical and extremal correlations in the many-body localization transition

This chapter is mainly based on Ref. [95].

5.1 Introduction

In this work we study the typical and extreme (atypically strong) correlations across a one-dimensional system in over the ergodic-MBL phase diagram, which give rise to different, but complementary phenomenology. We use the standard disordered Heisenberg model:

$$H = \frac{1}{4}\sum_{i=0}^{L-2} \vec{\sigma}_i \cdot \vec{\sigma}_{i+1} - \frac{W}{2}\sum_{i=0}^{L-1} h_i \sigma_i^z, \tag{5.1}$$

which has been extensively studied in the literature [4, 8, 12, 14, 15, 30, 38, 44, 46, 54, 55, 57, 59, 60, 64, 67, 85, 97, 106, 110]. As a probe of the correlations across the system we use the two-site quantum mutual information (QMI), which was introduced in the context of MBL in Ref. [30].

The structure of the distributions of the logarithm of the two-site QMI gives us insight into the typical behavior of the correlations between different regions of the chain. In particular, we study the mean, the standard deviation, and higher-order statistical moments of these distributions. We find that the mean decays exponentially with range at large disorder, consistent with the phenomenology of the MBL phase, and is constant at weak disorder, in line with the loss of locality characteristic of the ergodic phase (see Fig. 5.1). Interestingly, from moderate to strong disorder we find stretched exponential decay of correlations. Our observations suggest that at the ergodic-MBL transition typical correlations decay as a strenched exponential of the form $e^{-A\sqrt{r}}$, where r is the range of the correlations (distance between two sites). This is precisely the typical decay of correlations in the random singlet phase, which is a fixed point of the strong disorder renormalization group (SDRG), typically used to study disordered spin systems [33, 49, 88, 94, 99]. To our knowledge, our results present the first evidence of such behavior.

The width of these distributions shows distinct behavior in the ergodic and MBL phases. In the ergodic

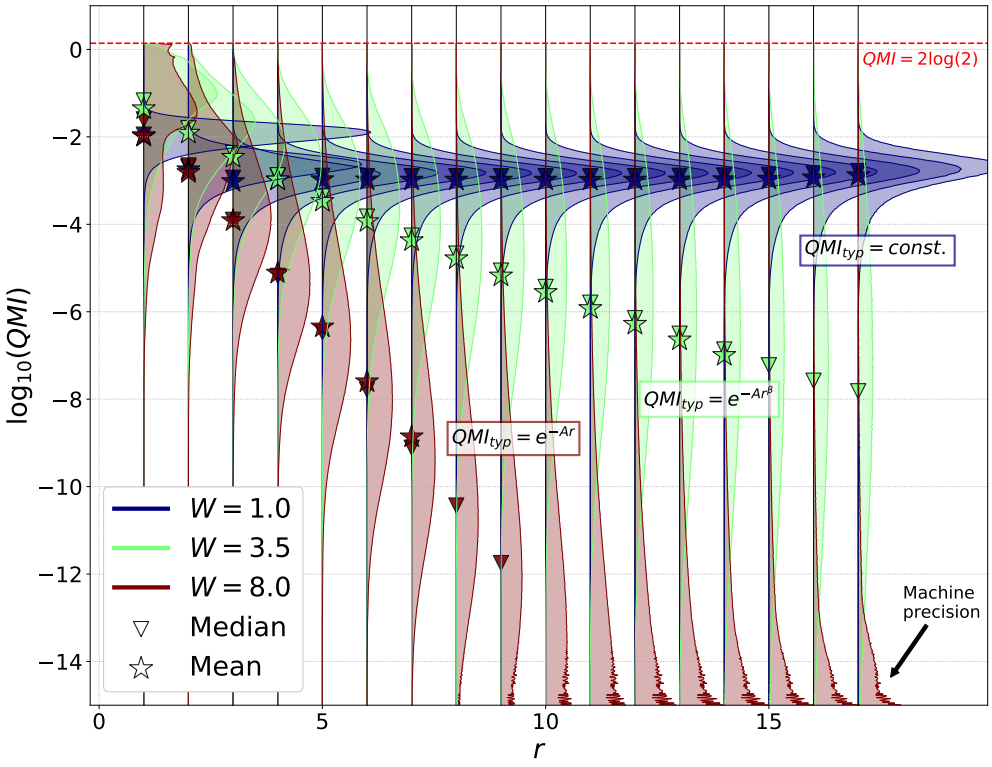

Figure 5.1: Probability distribution of logarithm of the two-site QMI for a system of size $L = 18$ for all ranges $r = |i - j|$ (between sites i and j) in the ergodic phase ($W = 1$), around the transition ($W = 3.8$), and deep in the MBL phase ($W = 10$). The stars indicate the mean of the distributions and the triangle indicate the median, which shows similar behavior. While the log-averaged QMI is constant with range in the ergodic phase, it decays exponentially deep in the MBL phase, and as a stretched exponential of the form $e^{-\beta r}$ at moderate values the disorder strength on the MBL side of the phase diagram. At the transition, the decay follows a stretched exponential with $\frac{\beta=1}{2}$, *i.e.*, $\log(QMI) = e^{-\sqrt{r}}$.

phase, the standard deviation of the distribution remains constant, as does the mean, consistent with the idea that there is no notion of range in this phase. At moderate and strong disorder, the standard deviation of the distributions increases linearly, with a rate of change that increases with disorder strength.

These distributions are skewed in opposite directions in the MBL and ergodic phases. At the transition, the skewness of the distributions seems to be range invariant. This is also the case for higher-order moments. Furthermore, *even* excess higher-order moments vanish at the transition, while *odd* excess moments take on non-trivial values.

In this work we also study the structure of the atypically strong correlations (or QMI bonds) formed across long-range regions of the chain, *i.e.*, the strong tail of the distributions of Fig. 5.1 for large range. In MBL, long-range bonds are extremely rare, due to the localization of correlations. At the same time, deep in the ergodic phase these bonds are also rare; this is due to the monomamy of the QMI and the fact that in the ergodic phase all regions are entangled with one another, leaving no room for the formation of a strong

singlets across the chain. Interestingly, these strong bonds proliferate around the transition in what seems to be a scale invarant fashion at large range. This suggests the proliferation of strong resonances at different length scales across the system.

Finally, we analyze the extremal statistics of the second singular value of the bipartite entanglement entropy in both phases and at the transition, which has been proposed recently as a robust order parameter in the ergodic-MBL phase diagram [82]. We find that the probability of finding an extremal second singular does not provide a robust order parameter for the transition. Instead, this probability vanishes as a power law *both* in the erogdic phase and for moderately disordered MBL phases, and only becomes finite deep in the MBL phase. The exponent of this power law varies smoothly at the transition, in contrast with the sharp change we would expect from an order parameter.

In Section 5.2 we analyze the structure of the typical correlations. In Section 5.3 we show our results on the extremal values of the QMI and their relation to scale invariant resonances. In Section 5.4 we discuss the extremal statistics of the second singular value of the bipartite entanglement entropy. Finally, in Section 5.5 we summarize our findings and discuss their implications.

For $L = 18$, we obtain 100 eigenstates close to $\epsilon \approx 0.5$ per disorder realization, over 10^4 disorder realizations, obtaining a total of 10^6 eigenstates. For $L = 14, 16$, we obtain 5 eigenstates close to $\epsilon \approx 0.5$ per disorder realization, over a total of 2×10^5 disorder realizations, obtaining also a total of 10^6 eigenstates per system size. We do this for different values of the disorder strength W. All calculations in this work are thus performed at an energy density of $\epsilon = 0.5$, *i.e.*, in the middle of the Hamiltonian spectrum.

5.2 Typical correlations

In this section we look at the typical values of the correlations across a system in an eigenstate of the Hamiltonian of Eq. (5.1) across the ergodic-MBL phase diagram. We use the QMI between all pairs of sites in a one-dimensional spin chain as a measure of the strength of their correlation that is agnostic to the choice of any particular correlation function. The QMI measures all correlations, both classical and quantum, between subregions in a system. The QMI between subregions A and B is defined as:

$$QMI_{AB} \equiv S_A + S_B - S_{AB}, \tag{5.2}$$

where S_A is the Von Neumann entanglement entropy between subsystem A and its surroundings; we will always work with the QMI between pairs of sites, which for sites i and j we denote QMI_{ij}. The two-site QMI has a maximum value of $2\log(2)$, which occurs when two sites form a singlet. However, in many-body

systems it is very rare for two sites to form a singlet without being entangled to other site; in the case of a multi-site singlet, the QMI between two sites is upper bounded by log(2). We define r as the distance between two sites, *i.e.*, $r \equiv |i - j|$. Ref. [30] finds that the typical values of the QMI decay exponentially with range in the MBL phase and slower than exponentially in the ergodic phase. Here we elaborate on the question of the behavior of the typical correlations along a one-dimensional system in the ergodic-MBL phase diagram.

In this section we work with the distributions of the $\log(QMI)$ (see Fig. 5.1, where, for readability, the $\log_{10}(QMI)$ is presented), as opposed to the distributions of the QMI. We consider the distributions of $\log(QMI)$ for each range r separately. In Section 5.2.1 we study the decay of the typical correlations with r; surprisingly, we find a region in the MBL side of the phase diagram with a stretched exponential decay at moderate values of the disorder strength W; this has similarities with the random singlet phase that arises as a fixed point in renormalization group studies of disordered systems [33, 88, 99]. In Section 5.2.2 we look at the standard deviation of these distributions, which cover several orders of magnitude, as a measure of their spread. Next, in Section 5.2.3, we study the higher-order statistical moments of the distributions; our results show that they are range invariant at the transition, and that higher-order *even* excess moments (as compared to a Gaussian distribution) likely vanish at the transition for large ranges. Finally, in Section 5.2.4 we summarize and discuss our findings on the typical correlations. As we can see in Fig. 5.1, the QMI reaches machine precision at large range r and large disorder strength W; we neglect those points (*i.e.* the triplet (L, W, r)) for which the distribution of the $\log(QMI)$ has a large part of its support under the machine precision threshold ($\approx 10^{-15}$). This is done by visual inspection.

5.2.1 The decay of $\mathbf{QMI_{typ}}$

The typical values of the QMI are defined as the log-average of the QMI:

$$QMI_{\text{typ}} \equiv \langle QMI \rangle_{\log} = e^{\langle \log(QMI) \rangle}, \tag{5.3}$$

i.e., it is computed by exponentiating the mean of the distributions of Fig. 5.1. Fig. 5.1 shows $\langle \log_{10}(QMI) \rangle$ (marked as stars; triangles show the median of the distributions, which follows similar behavior) as a function of range r for three different disorder strengths: $W = 0.5$ (ergodic), $W = 3.5$ (close to the transition), and $W = 8.0$ (MBL). In MBL, the decay of QMI_{typ} with range r is exponential. Around the transition, a detailed analysis shows that the decay does not follow an exponential, but rather a stretched exponential. Deep in the ergodic phase, there is no decay of QMI_{typ}.

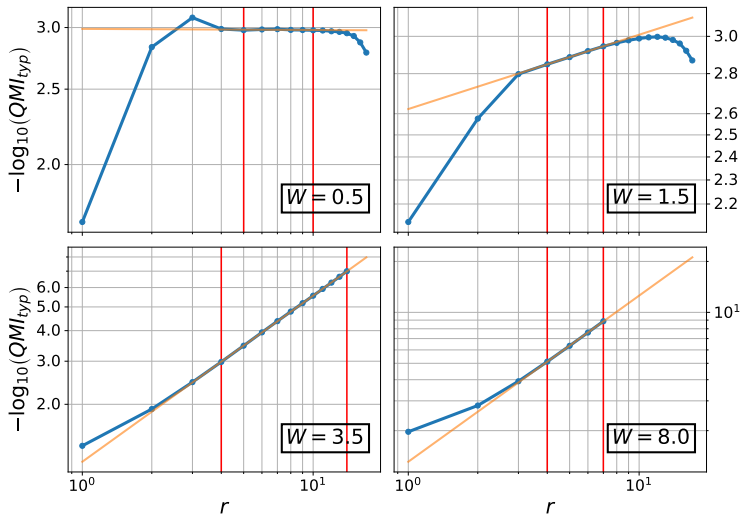

Figure 5.2: Log-log plot of $-\log(QMI_{\text{typ}})$ as a function of r for a system of size $L = 18$. We can see that for moderate and large disorder strength ($W = 3.5$ and 8.0 in the plots) the stretched exponential ansatz ($QMI_{\text{typ}} = e^{-Ar^{\beta}}$, with $B = 0$) fits well the data at large r. A linear fit to the curves is shown, as well as the interval of data taken for the fit (red vertical lines). Deep in the ergodic phase ($W = 0.5$), QMI_{typ} is constant. At slightly higher values of ($W = 1.5$), it is unclear what the functional form of the curve is, since the fit to a stretched exponential is not reliable. Note that finite size effects are more prominent at low disorder strength. This is due to long-range correlations being more characteristic of the ergodic phase.

We use the ansatz

$$QMI_{\text{typ}} = e^{-Ar^{\beta}} \tag{5.4}$$

and fit it to the decay of QMI_{typ}. Fig. 5.2 shows that a log-log plot of $-\log(QMI_{\text{typ}})$ is in good agreement with a linear fit at moderate and large disorder strengths ($W = 3.5$ and 8), while at lower values of the disorder strength ($W = 1.5$) the fit is of poor quality, and we simply find a constant scaling deep in the ergodic phase ($W = 0.5$). This suggests that the ansatz of Eq. (5.4) is a reasonable assumption for the decay of QMI_{typ} at moderate and large disorder strengths W. We can extract the exponent β from the slope of the fit to the log-log plot. The values of β are presented in the top panel of Fig. 5.3 (confidence intervals are defined by the maximum (minimum) β found over all linear fits of three or more consecutive points in the region fitted). As discussed above, the values of β are not reliable al low disorder strength; however, we present all values of β, even when not reliable. By visual inspection we consistently find across different system sizes L that the fits from which we extract β are of good quality above $W_{1/2}$, which we define as the value of W at which $\beta = 1/2$ [1] . Therefore, the stretched exponential behavior seems to be valid above

[1]Interestingly, the data on the log-log plots from which β is extracted fall below the linear fit at low ranges for weak disorder, while it lays above the linear fit at large values of W. The low range data falls exactly on top of the linear fit precisely when $\beta = 1/2$.

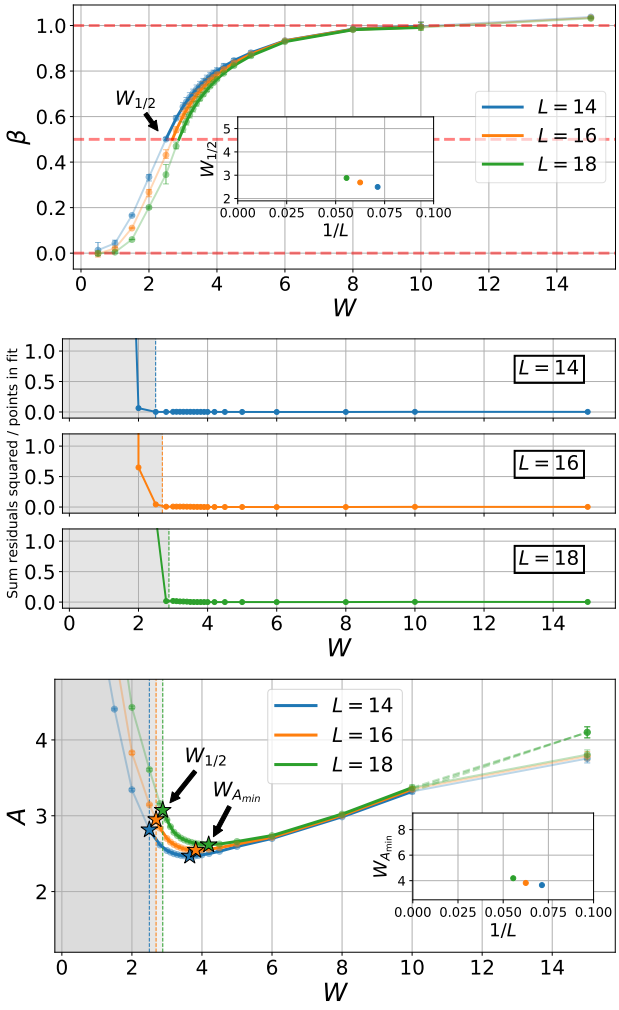

Figure 5.3: **Top:** exponent β of the stretched exponential of the decay of the typical QMI, $QMI_{typ} = e^{-Ar^{\beta}}$. **Middle:** average residual squared per point in the linear fit $QMI_{typ}^{1/\beta} = -A + B$. The y-intercept is zero if the stretched exponential assumption was correct, which is the case for $W > W_{1/2}$. **Bottom:** coefficient A as a function of W.

$W_{1/2}$ up to a value of W for which $\beta = 1$. At $W = 15$, we obtain a value for β larger than 1. We believe this estimate is not reliable, since only very few ranges at this disorder strength are considered due to the fact that the distributions of $\log(QMI)$ find machine precision limitations already at $r = 6$; however, we cannot rule out the validity of this result. The inset of Fig. 5.3 shows $W_{1/2}$ as a function of $1/L$ for the three values of L available. A naive extrapolation to $L \to \infty$ seems consistent with $W_{1/2}$ coinciding with the critical value of W in the thermodynamic limit, *i.e.*, $W_{1/2}(L \to \infty) = W_c$.

In order to back our observation that the decay of QMI_{typ} follows a stretched exponential (Eq. 5.4) down to the value of W for which $\beta = 1/2$ ($W_{1/2}$), we present in the middle panel of Fig. 5.3 the average residual squared per point in the fits from which β was extracted, *i.e.*, log-log plots alike those of Fig. 5.2. We can see

that the residuals are consistent with high-quality fits above $W_{1/2}$, where they are practically zero. Below $W_{1/2}$, which has been shaded out, the residuals per point rapidly increase. This is in great agreement with our observations.

Finally, the bottom panel of Fig. 5.3 shows the values of A in the stretched exponential as a function of W for different system sizes. We extract A from the slope of a linear fit of $\log(QMI_{typ})^{1/\beta}$ as a function of r, where β takes the empirically obtained value of the top panel of Fig. 5.3. These fits give a y-intercept of practically zero (within error bars; not shown) for $W > W_{1/2}$, which is an excellent *a posteriori* consistency check for our ansatz. On the contrary, the y-intercept is non-zero below $W_{1/2}$. As in the case of β, we show all values of A found, regardless of their reliability. In addition, we show the value of A at $W = 15$ that we would have gotten in the case that $\beta = 1$ (dashed line), as opposed to the slightly larger value that we empirically obtained; this value of A presents arguably a smoother curve, and we let the reader interpret this as a sign of $\beta(W = 15) = 1$ being a more reasonable value. We have highlighted two sets of points in this panel (marked as stars). First, the values of $A(W_{1/2})$ show an increasing trend as $W_{1/2}$ shift towards higher values of W with system size; we will revisit this in Section 5.2.4. Second, we point the reader to the points at which A is minimal, $W_{A_{min}}$. If the QMI decays exponentially deep in the MBL phase, *i.e.*, $QMI_{typ} = e^{-Ar}$, the reasonable assumption that a system becomes more localized as W increases would imply that A increases with W, since $1/A$ can be interpreted as a localization length. For this reason, $W_{A_{min}}$ is a good lower bound for the point where the stretched exponential decay region meets the exponential decay region of the phase diagram, which we denote W_1. A simple naive extrapolation of the points in the inset is consistent with a value of $W_1 \approx 8$, which leaves open the questions of whether $W_{1/2}$ is strictly lower than W_1 in the thermodynamic limit or not, and whether W_1 approaches a finite value in this limit. Our data suggests that that $W_{1/2} < W_1$ and $W_1 < \infty$ in the thermodynamic limit, case in which the stretched exponential decay region is stable, as well as the exponential decay region. However, we cannot rule out two other scenarios in which either $W_{1/2} \to W_1$ in the thermodynamic limit, or $W_1 \to \infty$ [2] . Slightly below $W_{1/2}$ we cannot find a simple functional form for the decay of QMI_{typ}. However, deep in the ergodic region $QMI_{\text{typ}} = \text{const.}$.

5.2.2 The standard deviation

We use the standard deviation of the distributions of $\log(QMI)$ as a measure of their width. It is already apparent from Fig. 5.1 that the width of the distributions deep in the ergodic phase is constant. Around the transition and deep in the MBL phase, the width increases with r.

[2] We are assuming here that $\beta \leq 1$, which we have not ruled out either.

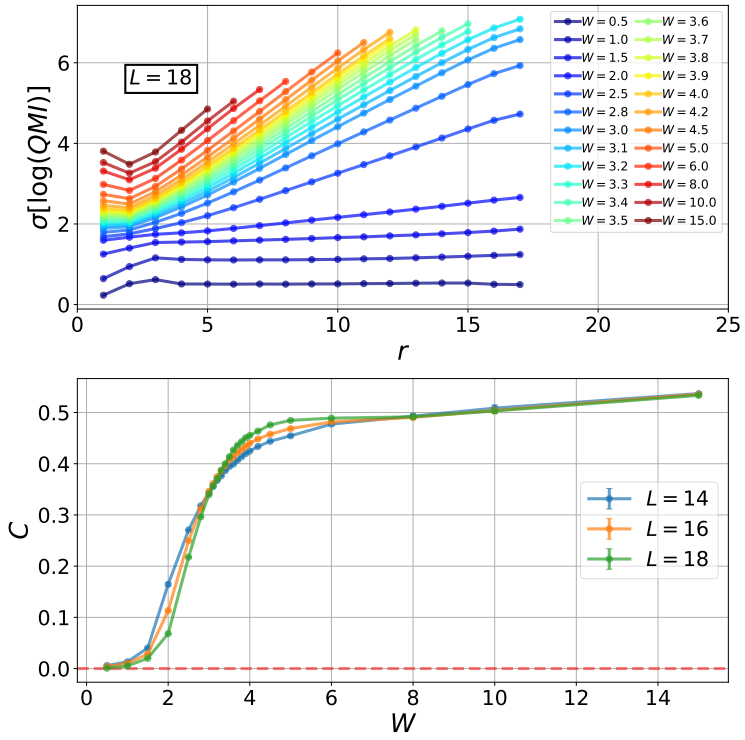

Figure 5.4: **Top:** standard deviation of $\log(QMI)$ as a function of range r for different values of the disorder strength W, for systems of size $L = 18$. We can see at sufficiently large r that the scaling is linear with r. Note that points affected by the finite machine precision have been removed and that finite size effects are present at the largest values of r. As in the case of β, confidence intervals are defined by the maximum (minimum) value of β found over all linear fits of three or more consecutive points in the region fitted. **Bottom:** slope C of the linear fit of $\sigma\left[\log(QMI)\right] = C \cdot r + D$ for different system sizes. The transition region from range-invariant $\sigma\left[\log(QMI)\right]$ to a slope of $C = 0.5$ seems to be consistent with the estimates of the critical disorder strength of Section 5.2.1.

We present $\sigma\left[\log(QMI)\right]$ as a function of r in the top panel of Fig. 5.4. Surprisingly, after eliminating distributions affected by machine precision, and ignoring finite size effects at large range r, all curves follow linear scaling as a function of r of the form $\sigma\left[\log(QMI)\right] = Cr + D$. As expected, we find constant $\sigma\left[\log(QMI)\right]$ deep in the ergodic phase, and the distributions broaden with r otherwise, with a larger coefficient C as the disorder strength W increases. The lower panel of Fig. 5.4 shows the values of C as a function of W for different system sizes. There is a rapid increase in C from $C \approx 0$ to $C \approx 0.5$, which gets sharper at larger system sizes L. The curves cross at values of W that are consistent with typically extimated values of the critical W_c for the model of Eq. (5.1), *i.e.*, $W_c \approx 4$. As opposed to the case of β of Section 5.2.1, for which $\beta(W = 15)$ was likely to be an unreliable outlier, the values of C at large W seem to follow an increasing trend with disorder strength W over many points.

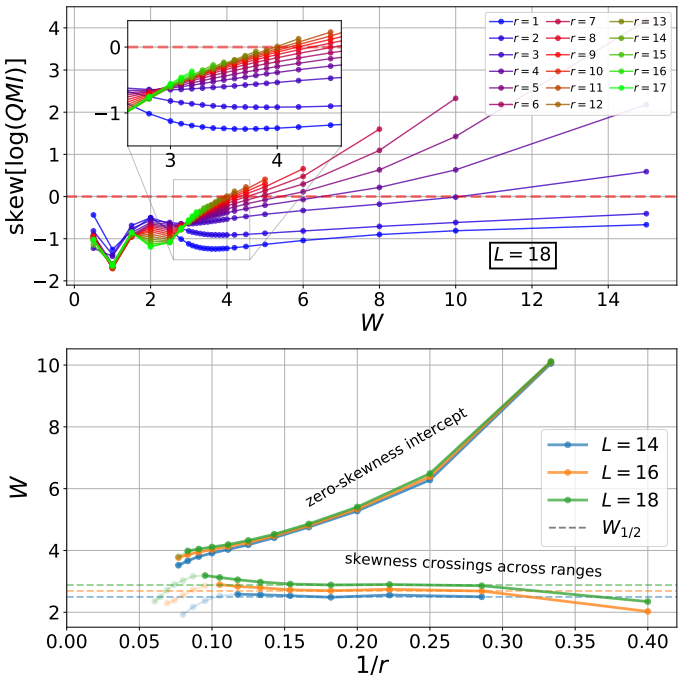

Figure 5.5: **Top:** skewness of the distributions of $\log(QMI)$ as a function of range r for a system of size $L = 18$. We can see that at large W the distributions are positively skewed (except for the smalles ranges $r = 1, 2$) and that at weak disorder they are negatively skewed, as is apparent from Fig. 5.1. Around the transition and for large enough ranges, the skewness crosses zero, a necessary condition for the distributions to look symmetric around their mean. **Bottom:** the upper curves show the value of W at which the skewness is zero as a function of $1/r$ for different system sizes; note that the largest ranges do not cross the zero skewness line because of eliminating points due to machine precision issues, as explained in Section 5.2.1. The lower curves show the value of W at which the skewness crosses for consecutive ranges r and $r + 1$; for each pair $(r, r + 1)$ we consider the range $\frac{r+(r+1)}{2}$ as its x-coordinate; the largest ranges have been shaded out, since we believe are strongly affected by finite size effects. Dashed lines represent the values of $W_{1/2}$ for in Section 5.2.1 for each system size L. We can see that both sets of curves are compatible with convergence in the limit $r \to \infty$, and that their trend with system size L suggests a transition zero skewness transition point.

5.2.3 The skewness and higher-order statistical moments

In Fig. 5.1 we can appreciate that the distributions of $\log(QMI)$ are skewed negatively deep in the ergodic phase, and positively deep in the MBL phase, with perhaps a more symmetric, unskewed shape around the transition. In this section we study the skewness of these distributions, as well as higher-order statistical moments.

The *excess* standardized moment of order n of a distribution over a random variable x is defined as:

$$\mu_n^{\text{excess}} \equiv \mu_n - \mu_n^{\text{normal}} = \frac{\mathbb{E}\left[(x - \langle x \rangle)^n\right]}{\sigma^n} - \mu_n^{\text{normal}}, \tag{5.5}$$

where μ_n is the standardized moment of order n of the distirbution and μ_n^{normal} is the standardized order

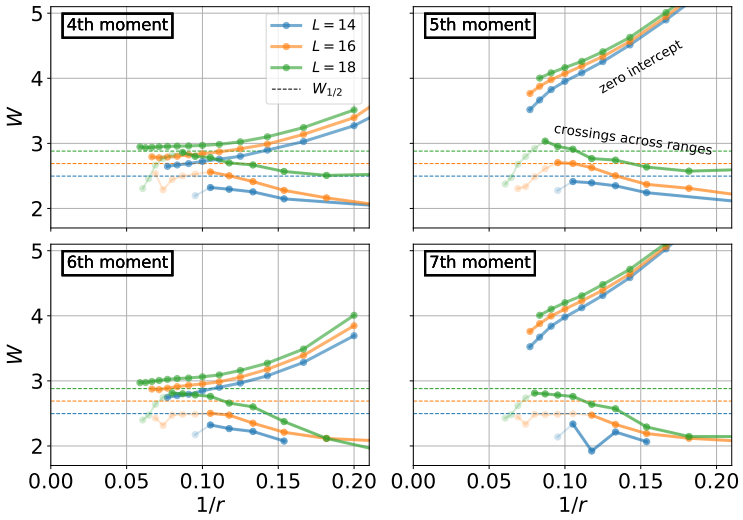

Figure 5.6: The behavior of the excess statistical moments with respect to a Gaussian distribution of the distributions of $\log(QMI)$ suggests they are range invariant at the transition. Similar to the case of the skewness and Fig. 5.5, we show those values of W at which the nth moment is zero for each range and system size, as well as those values for which the moments consecutive ranges coincide. Only crossings between ranges in the interval $W \in [2, 5.5]$ are presented, and points that we believe are strongly affected by finite size effects are shaded out. These results suggest the *even* excess moments of the distributions of $\log(QMI)$ vanish at the transition for large L and r, while *odd* moments take on non-trivial values. Note that for the highest order moments we study the signal becomes fairly nosiy.

n moment of a Gaussian distribution, which has therefore zero excess moments of all orders. A normal distribution has zero odd moments, and strictly positive even moments, which are equal to $n!!\sigma^n$. The third standardized moment of a distribution is called its *skewness*.

We present the skewness of $\log(QMI)$ as a function of W for each range r for a system os size $L = 18$ in the top panel of Fig. 5.5. As expected, the skewness is negative at low disorder strength W and positive for sufficiently large ranges r at large values of W. Interestingly, as seen more clearly in the inset of the figure, the curves of different ranges cross at a point that is close to $W_{1/2}$ for $L = 18$. Furthermore, the point at which the skewness vanishes drifts with r and seems to converge at large r close to $W_{1/2}$. As customary in this section, we have eliminated the (L, W, r) points that correspond to distributions that hit machine precision.

The bottom panel of Fig. 5.5 shows the values of W at which the skewness of consecutive ranges cross each other, as well as those values of W at which the skewness vanishes for each range; in both cases, we plot the crossings as a function of $1/r$, where for each L, $r < L$. In both cases we interpolate linearly in order to find these crossings. [3] As a guide to the eye we show horizontal lines at $W_{1/2}$ for each system size (dashed lines). Our results are compatible with a skewness that vanishes at $W_{1/2}$ at sufficiently large range

[3] As mentioned, machine precision affected points have been eliminated. Furthermore, for the crossings across consecutive ranges, we only include those found above $W = 1.9$.

r. We have shaded out those points at large range for which we believe there are strong finite size effects.

We now analyze in a similar manner the higher-order excess standardized moments of $\log(QMI)$. Odd moments follow a similar trend as that one of the top panel of Fig. 5.5. Even moments have slightly different curves. In both cases we can keep track of the zero-skewness intercept, as well as the consecutive-range crossings. Fig. 5.6 shows these crossing curves as a function of $1/r$, in a similar way to the lower panel of Fig. 5.5. In all cases, the results are consistent with excess moments vanishing at $W_{1/2}$. For very high order moments we find larger noise in the data.

5.2.4 Putting all together

In summary, the typical correlations in a one-dimensional spin chain of the model in Eq. (5.1) decay exponentially deep in MBL. Deep in the ergodic region, correlations are constant with range r. At moderate disroder strength, and above W_c, ($W_c \leq W \lessapprox W_1$), typical correlations decay as a stretched exponential, which takes the form $QMI_{\rm typ} = e^{-A\sqrt{r}}$ at the transition (*i.e.*, $W_{1/2} = W_c$). Our results suggest that this stretched exponential decay region of the phase diagram is stable in the thermodynamic limit, as well as the exponential decay region. [4]

The distributions of $\log(QMI)$ have constant spread (standard deviation) deep in the ergodic phase. At moderate and strong disorder strengths, they broaden linearly with range r.

Our results suggest range-invariant skewness and higher-order moments that vanish at $W_{1/2}$. In addition, *even* higher-order moments vanish at the transition. This indicates that at the transition the distribution of $\log(QMI)$ is range invariant (except for its standard deviation) with a mean that decays as a stretched exponential with $\beta = 1/2$, $QMI_{typ} = e^{-A\sqrt{r}}$. Such a decay of the typical correlations is found in the random singlet phase, which emerges as a fixed point in strong disorder renormalization group studies of disordered systems.

There is a paradox in the fact that at $W_{1/2}$ the distribution of $\log(QMI)$ has range-invariant higher-order statistical moments with a mean that decays with $\sqrt{r}$, while its standard deviation increases as $Cr+D$. Such family of distributions would quickly (as r increases) have half of their weight above $QMI_{max} = 2\log(2)$, which is a hard upper bound for the QMI. In order for these scalings (mean and standard deviation) to be compatible with range-invariant higher-order statistical moments, the area under the distribution that lays above QMI_{max} has to vanish with r, or at least stay constant. The only way out of this paradox is a coefficient $A(W = W_{1/2}, L)$ that increases at least as fast as $L^{1/2}$ with system size, but not with a smaller

[4] We can however not rule out scenarios in which: (1) $W_1 \to \infty$ in the thermodynamic limit, (2) $\beta > 1$ (compressed exponential decay) for $W > W_1$, (3) $W_{1/2} \to W_1$ in the thermodynamic limit, (4) $W_{1/2} \neq W_c$, or compatible combinations of them.

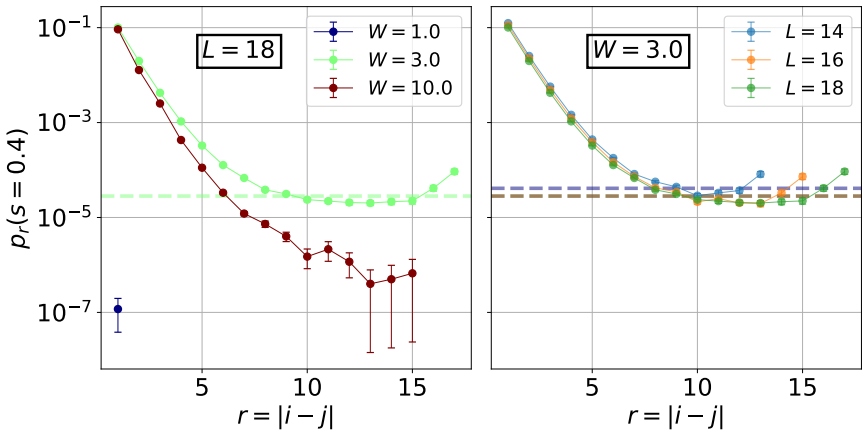

Figure 5.7: Probability $p_r(s)$ that, given a pair of sites i and j a range r apart from each other, their QMI_{ij} is larger than s, for $s = 0.4$, as a function of r for different disorder strengrths W. Deep in the MBL phase ($W = 10$), $p_r(s)$ decays with r, in line with the localization of correlations. Deep in the ergodic phase ($W = 1$), the order of magnitude of the correlations is typically small and has small spread (see Section 5.2, which means that it is very unlikely to find a value of the QMI that exceeds s. For this reason, we do not have enough data compute $p_r(s)$. Around the transition ($W = 3$), the probability of finding strong two-site QMI bonds becomes range invariant, *i.e.* is constant as a function of r at sufficiently large r (and away from finite size effects at very large r.

exponent. This way, larger values of r are only encountered for large values of L, which guarantee a large enough coefficient A, and thus enough room for the distribution to broaden while staying mostly below the $2\log(2)$ threshold. Our results (see lower panel of Fig. 5.3, $W_{1/2}$ stars) are compatible with this scaling; however, given the small amount of data (only three small values of L), we cannot make any reliable claim. In general, in the stretched exponential decay region, we require $A(W, L)$ to scale at least as $L^{1-\beta}$.

5.3 Extreme correlations

In this section we study the strong tail of the distributions of the QMI, *i.e.*, the probability that a pair of sites a range r apart has a very large QMI. This study, therefore, refers to the upper end of the distributions of Fig. 5.1. This is in contrast with the study of the typical values of the QMI, which focus on the highly likely values of these distributions.

While the maximum theoretical value of the QMI between two sites is $QMI_{max} = 2\log(2)$, this value is only achieved if those sites are completely disentangled from any other subsystem, while forming a strong singlet between them. This is the case when pairs of sites resonate in non-interacting systems. In many-body systems (as the one we study here), however, the typical scenario is that one of multi-site resonances; single pairs resonating isolated from the rest of the system are possible, but they are exponentially rare for large ranges. In the many-body, multi-site resonance case, the maximum QMI is $\text{QMI}_{\text{max, many-body}} \approx \log(2)$,

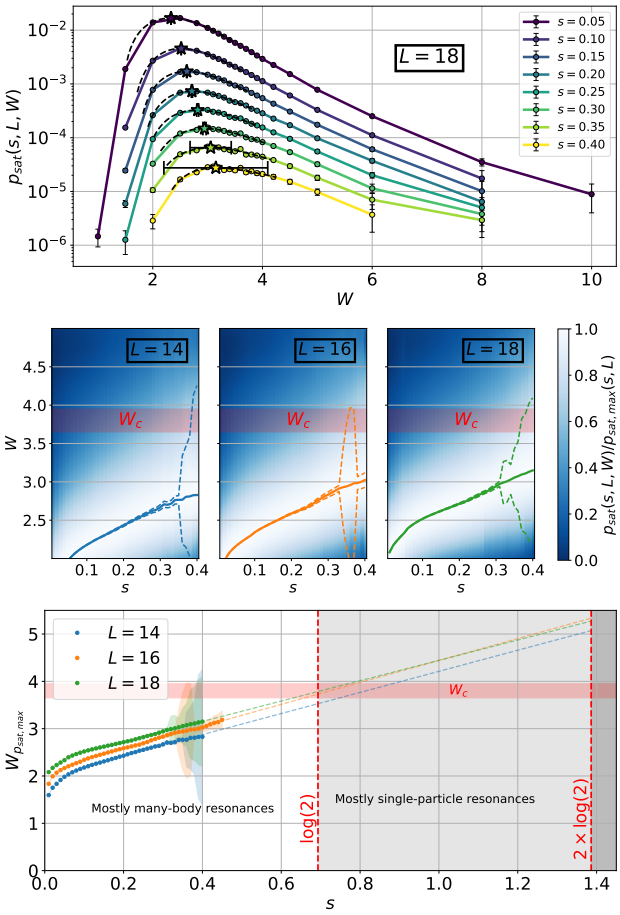

Figure 5.8: **Top:** probability that a pair of sites a large range r away from each other have a two-site QMI exceeding s, $p_{sat}(s, L, W)$, as a function of W. The position of the maxima, p_{sat} (stars), is obtained from a high-order polynomial fit. Error bars are derived from bootstrap resamples over disorder realizations. **Middle:** colormap with the high-order polynomial fits of the top panel, normalized by the maximum value of p_{sat}. $W_{p_{sat,max}}(s)$ is plotted, which is compatible with the maximum probability of finding strong, long-range QMI bonds at the critical disorder strength W_c in the thermodynamic limit. **Bottom:** linear extrapolation of $W_{p_{sat,max}}(s)$ for larger values s. The extrapolations are compatible with $W_{p_{sat,max}} \approx W_c$ when $s = \log(2)$.

which is the QMI between each pair of sites in the cluster. [5] .

In order to systematically study the strong tail of the distributions of the QMI, we define $p_r(s)$, *i.e.*, the probability that a pair of sites i and j range r apart from each other have a QMI larger than a threshold s. We then increase the threshold s as much as we numerically can, without incurring in really poor statistics; note that the number of samples decreases quickly as s increases. We present in Fig. 5.7 the decay of $p_r(s)$ as a function of r, for fixed s ($s = 0.4$ in the figure); errors represent the standard deviations of the distribution of $p_r(s)$ over 200 bootstrapping resamples. On the left panel we can see that, for high enough values of the threshold s, $p_r(s)$ becomes range invariant around the transition $W = 3$, *i.e.*, for large enough r (but away

[5] This value is exact when the spin at each site is an exact integral of motion, and is subject to fluctuations when the integrals of motion are locally dressed spins, which is the case in MBL

from the largest values of r, in order to avoid finite size effects), the probability of finding a strong QMI bond saturates at a value which $p_{sat}(s, L, W)$, which is a function of s, L, and W, shown as a dashed line. In practice, we estimate p_{sat} as the mean of $\{p_r(s)\}_{r \geq 9}$, and only compute this quantity when $p_r(s)$ is non-zero at all reanges. Deep in the MBL phase, our data shows a probability that decays with r up to the ranges that we have access to. In the ergodic phase, the probability decays very rapidly with r as well, and we do not have enough samples analyze the decay. The right panel of Fig. 5.7 shows the range-invariant curves of $p_r(s)$ for different system sizes L. We can see that p_{sat} at this value of W decays slightly with L.

5.3.1 Proliferation of strong long-range correlations around the transition

It is interesting to analyze the saturation values of $p_{sat}(s, L, W)$. While the range-invariant probability of finding a strong QMI between pairs of sites is presumably seen only at the transition in the thermodynamic limit, for the small system sizes we study here, we find this behavior over a region of intermediate disorder strengths. In this region, however, we find that the maximum value of $p_{sat}(s, W, L)$ is achieved at a disorder strength W close to the transition.

The top panel of Fig. 5.8 presents the values of p_{sat} as a function of W for different thresholds s for a system of size $L = 18$. The error bars on p_{sat} represent the standard deviation of the distribution of p_{sat} for 200 bootstrap resamples of the disorder realizations of the model in Eq. (5.1). The maximum of each curve is computed through a local, high-order polynomial fit, and is shown with a star [6] . The error bar on the position of the maximum is estimated also from bootstrapping. As we can see, at large threshold s, the position of the maximum is very unstable, due to the small number of samples past that threshold, as well as the curves being flatter around the maximum.

For convenience, the middle panel of Fig. 5.8 shows a colormap with all fitted curves of $p_{sat}(s, W, L)$ obtained for thresholds between $s = 0$ and $s = 0.4$ and for three different system sizes. The curves shown in the colormap have been normalized by their maximum value, $p_{sat,max}$, so that they are all visible in the plot. The values of W at which p_{sat} is maximum, $W_{p_{sat,max}}$, are plotted as a curve, with error intervals derived from bootstrapping (dashed lines). Typically, numerical studies find a critical disorder strength of about $W_c \approx 3.8$; as a visual guide, we have shaded in red the region where W_c is thought to be in the thermodynamic limit. We can see that the trend of $W_{p_{sat,max}}$ is compatible with it achieving W_c at large s and L.

The bottom panel of Fig. 5.8 elaborates more on the observation that $W_{p_{sat,max}}$ flows in the direction of W_c as s and L increase. The same curves as in the middle panel are plotted (with the same bootstrap error

[6] We find good results fitting to a polynomial of degree seven for all points available in the interval $W \in [0, 6.2]$.

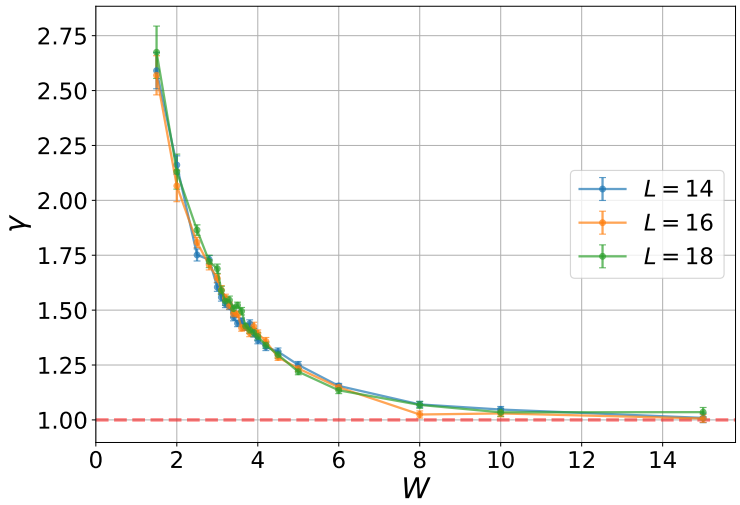

Figure 5.9: Exponent γ of the scaling of the CDF of the second entanglement eigenvalue of the half cut bipartite entanglement entropy as it approaches its minimum value as a power law, *i.e.*, $\mathrm{CDF}(\lambda_2) \propto [\lambda_2 - \log(2)]^{\gamma}$, for $\lambda_2 \to \log(2)^{+}$. Confidence intervals correspond to the standard deviation of γ from 200 bootstrap resamples over the original disorder realizations. As we can see, $\gamma = 1$ deep in the MBL phase, which is compatible with a non-zero value of the $p(\lambda_2 \to \log(2)^{+}$ of finding a singlet across half cut in the chain. At moderate disorder strengths and close to the transition, $\gamma > 1$, which implies a vanishing probability of finding a singlet across the chain. Deep in the ergodic phase we do not have enough extremal data close to log(2) a power law as the CDF approaches zero.

bars as above), together with a naive linear extrapolation for larger s. While these naive extrapolations hit $s = 2\log(2)$ at a value of W at that is to be larger than typically extimated W_c, the extrapolation up to $s = \log(2)$ seems to be more consistent with a proliferation of resonances at the critical point. As discussed above, a maximum value of the QMI (and thus of the threshold s) of about log(2) is more reasonable for a many-body system, like the one we study in this work.

5.4 Extreme entanglement eigenvalues

In this section we study the strong tail of the distributions of the singular values of the reduced density matrix of a subsystem, which have been proposed recently as yielding a robust order parameter for the ergodic and MBL phases [82]. In particular, Ref. [82] suggests that the second largest singular value of the bipartite reduced density matrix, ρ_2, has a logarithmic probability distribution ($p(\lambda_2)$, where $\lambda_2 \equiv -\log(\rho_2)$, *i.e.*, the so-called second entanglement eigenvalue of the system) that reaches a finite value in the strong end of the distribution [7] . In mathematical terms, $p* \equiv \lim_{lambda_2 \to \log(2)^{+}} p(\lambda_2)$ is finite in MBl and vanishes in the ergodic phase. The limit $p*$ hence has the potential of providing an order parameter for the ergodic

[7]Note that the definition of λ_2 is here different from the one we have usually referred to across this thesis. We are now taking the logarithm of the square of what the schmidt singular values across a cut.

and MBL phases. Morever, the authors of Ref. [82] find that the values of this limit are robust to finite size effects, showing negligible variations across different values of L for small system sizes.

We argue here that the probability of finding values of λ_2 close to its minimum value, $p*$, does become finite only deep in the MBL phase, but vanishes however at moderate values of W, still in the MBL phase. In particular, the CDF of the distribution vanishes as a polynomial of degree γ:

$$\lim_{\lambda_2 \to \log(1/2)^+} CDF(\lambda_2) \propto [(\lambda_2 - \log(1/2)]^\gamma. \tag{5.6}$$

Fig. 5.9 shows the empirical values of γ we find. Error bars represent standard deviations of γ from 200 bootstrap resamples over disorder realizations. The PDF of the distribution of λ_2, after integration of the CDF, follows a power law of exponent $(\gamma - 1)$, which is compatible with a non-zero probability $p*$ only if $\gamma = 1$. On the contrary, $\gamma > 1$ implies that $p* = 0$. See Appendix H for more details on the extraction of γ and its error bars.

Our results suggest that $p*$ is only non-zero deep in the MBL phase, and vanishes at moderate disorder well above the transition. We argue that the CDF of the distribution of λ_2 in the limit of small values is a more robust presents a more robust method to estimate the behavior of the distribution in this limit and than the direct estimation of the PDF. The reason for this is that the estimation of the PDF is done numerically by histogramming samples of λ_2. In the case that the PDF of λ_2 vanishes in the limit of small λ_2, the finite size of the bins of the histogram will mask this effect, giving the illusion that $p*$ is indeed finite. The estimated value of $p*$ will then depend on the chosen bin size. Changing the size of the bins of the histogram will indirectly move the transition point drawn from $p*$ as an order parameter. The CDF, on the contrary, lets us devise the funcional form of the PDF in a more controlled way.

Nevertheless, it is important to emphasize that the model studied in Ref. [82] is similar to the one in Eq. (5.1), but the random magnetic fields are sampled from a Gaussian distribution, rather than from a uniform distribution, as is in this work and in most other studies. We also emphasize that we have worked with the bipartite reduced density matrix of a sybsystem after a cut through the middle of the system; in Ref. [82] a subsystem of only five spins is always considered, regardless of the system size. We do however find γ to be very robust to changes in the system size, at least for moderate and strong values of W. This is presumably due to the fact that strong values of the second singular value of the bipartite reduced density matrix are found when a single bit of entanglement (and only one) is shared across the two halves of the system. In the MBL phase, this is indeed common across neares neighbors, and so the formation of such singlets is presumably reobust against the total size of the system, whose boundaries are tipycally far away

from these neighboring pairs of sites. For this reason, we believe the exact location of the cut that divides the system into two subsystems is not relevant.

5.5 Conclusions

In this work we have studied both the typical and extremal values of the correlations across a system in an eigenstate of the Hamiltonian of Eq. (5.1). As a probe of the correlations across the system we have extensively used the two-site QMI.

The main contribution of our work is identifying a region at moderate disorder strength that shows a stretched exponential decay of the typical correlations as a function of the range r. At the transition, this decay takes the form $e^{-A\sqrt{r}}$, which is also found in the random singlet phase, which represents a fixed point of the strong disorder renormalization group, often used to study disordered systems. A second key result of our work is showing that the distributions of the $\log(QMI)$ between pairs of sites far from each other approach a range-invariant distribution (in the skewness and higher-order statistical moments) in the thermodynamic limit, which broadens as a function of the range, and which has vanishing *even* excess moments. We therefore find a distinct behavior of the correlations at the transition, which contrasts with an exponential decay of the typical correlations in the MBL phase and typical correlations that are range invariant in the ergodic phase.

We have also studied the atypically strong correlations across the system, which can be regarded as signs of the existence of resonances. Our results show that resonances proliferate at the transition, where the probability of two sites resonating with each other becomes range invariant. In contrast, in the MBL phase resonances become extremely rare at long ranges. Similarly, in the ergodic phase, correlations entangle all regions of the system, and so rare resonances in an otherwise localized system just do not exist.

Finally, we have studied the extremal values of the second entanglement eigenvalue, λ_2, which signal the presence of a single bit of entanglement across a bipartition of the system. The probability of λ_2 approaching its minimal value, $p*$, was recently proposed as a robust order parameter for the ergodic-MBL transition, which vanishes in the ergodic phase and is finite in the MBL phase [82]. Our results show that this probability is only finite deep in the MBL phase, and vanishes as a power law at moderate values of the disorder strength and in the ergodic phase. We therefore argue that $p*$ is not a good order parameter of the ergodic-MBL transition.

Chapter 6

Outlook and future work

In Chapter 1 we have discussed the main motivations behind the study of MBL, as well as some of its most prominent challenges. Some of these challenges were consequences (sometimes subtle) of the ideas presented in Chapter 2, which discussed the numerical methods used in the field of MBL and gave some insight on the difficulty to develop tools to dive into the study of the ergodic-MBL transition. Moreover, Chapter 2 also gave some insight on the fact that the MBL phase is numerically accessible, both through eigenstates of the Hamiltonian, as well as through its local integrals of motion, or l-bits. This optimistic results do not extrapolate to the ergodic phase and to the transition.

The main contributions of the work presented in this thesis are related to efforts aiming at approaching the ergodic-MBL transition from a numerical point of view, in order to gain insight on its nature. On the one hand, in Chapter 3 we confirmed for large (but still finite) systems the existence of the mobility edge; here we used matrix product states to access MBL eigenstates of large systems, sacrificing our ability to access eigenstates on the ergodic side of the phase diagram. The mobility edge is present at moderate values of the disorder strength W, and it separates ergodic and MBL eigenstates by energy. Despite numerical evidence (we observe a mobility edge over the largest system sizes studied in the literature) its existence is still controversial. Interestingly, through the study of approximate integrals of motion drawn from single MBL eigenstates, we observed that eigenstates below the mobility edge are aware of the existence of ergodic eigensates at higher energies. This shows a difference in behavior between MBL eigenstates in a fully MBL phase and those laying under a mobility edge.

On the other hand, in Chapters 4 and 5 we tackled the ergodic-MBL transition directly through exact diagonalization methods, which constrained us to small system sizes, but gave us the ability to cross the transition into the ergodic phase. Both studies show results that are compatible with the proliferation of strong, long-range resonances at the transition. Chapter 4 does so in an unconventional way: looking at the system from a basis of dressed spins (pseudo-spins) which form a complete set of integrals of motion and which, in MBL, act as frame from which we can observe the system without losing the notion of locality and, with it, of real space. We then analyze the hybridization processes that an eigenstate undergoes

as it is evolved adiabatically from a disorder strength W to a disorder strength $W + dW$. Surprisingly, strong hybridization with other eigenstates becomes range-invariant at the transition. The notion of range invariance has been an elusive one in the ergodic-MBL transition. This allowed us to define a localization length that diverges at the transition, another feature that has proven difficult to find.

In Chapter 5, scale invariance manifests in a slightly different way. We now stick to real space; we use real spins as opposed to pseudo-spins, or dressed spins. We study the correlations between pairs of sites and find that strong correlations (so strong that the subset of sites that are correlated with each other cannot be strongly correlated with third parties, as can be understood from the notion of monogamy of the quantum mutual information, which is the quantity that lets us measure correlations in the first place) appear with equal probability over all ranges when the system approaches the transition. These strong correltions can be interpreted as part of a many-body resonance across the system.

Most interestingly, Chapter 5 gave us insight on the structure of the typical correlations across the system, rather than the strongest ones. From here we drew phenomenology that is distinct to the ergodic-MBL transition, setting it apart from either the ergodic or MBL phases: typical correlations approach a Gaussian distribution over their log for large enough ranges over large enough systems. The typical value of the correlations (rather than their full distribution, which is Gaussian) decays as $e^{-\sqrt{r}}$ with range r. This decay is reminiscent of the decay of the typical correlations with range of the random singlet phase, which is a fixed point of the strong disorder renormalization group, usually used in the study of disordered systems [33]. Moreover, there seems to be a region at moderate disorder, and lower bounded in W by the transition, at which typical correlations decay as a stretched exponential, a result that is also contribution of this work.

More insight into the MBl problem will require work in different directions. After several years attracting substantial attention, the progress in understanding the MBL has slowed down. Most obvious ways to study this problem, as well as other not-so-obvious ones, have already been carried out, both analytically and numerically. Perhaps the experimental perspective is the one which will shine more light into this field. With the advent of high quality analog and digital quantum simulations, the ergodic-MBL transition in both one and higher dimensions might turn into a less elusive problem.

That said, the study of MBL has sparked the design of a plethora of numerical techniques, which, beyond MBL, have found application elsewhere. Moreover, the particularities inherent to the MBL phase and its complexity from a classical computational point of view have trained a subset of computational quantum physicists to think in a way that blends well with the tensor network and the quantum computing fields, which are currently very active. Given this prolific record, the numerical study of MBL has the potential to

keep making substantial progress.

Appendix A

Supplementary data on the correlation length of the OPOs

The SIMPS algorithm does not allow us to access the weak disorder limit at finite energy density, due to the transition to an ergodic phase. However, it is possible to access this limit at $\epsilon = 0.0$ using DMRG, and it is interesting to see the system size dependence of the the decay of $\bar{F}_R$ and its associated ξ for ground states. We can see in Fig. A.1 that the decay is seemingly exponential well into the weak disorder limit, where ξ becomes large and increases strongly with L.

The exponential decay of the total contribution F_R from the string operators of range R to the number operator of the OPOs is not only seen in average ($\bar{F}_R$), but also in the 2D histogram of F_R vs. R. We demonstrate in Fig. A.2 for $\epsilon = 0.0, 0.1$ and systems of size $L = 64$ that at all disorder strengths F_R presents a signal that decays exponentially with R away from long ranges, for which the finite size effects (and possibly noise due to the numerics) are stronger.

The correlation length ξ increases monotonically with L, as mentioned in Section 3.6.1 (see Fig. 3.4). The precise functional form of the scaling is not determined due the few data points available, but at $W \lessapprox W_c$ the points align suggesting a logarithmic scaling of the form $\xi = \log(\beta \cdot L^{\alpha})$. Assuming this form is correct, we can estimate the value of α as a function of W (see Fig. A.3). It is interesting to see that α increases as the disorder is lowered, implying a faster increase in ξ with system size as W gets smaller.

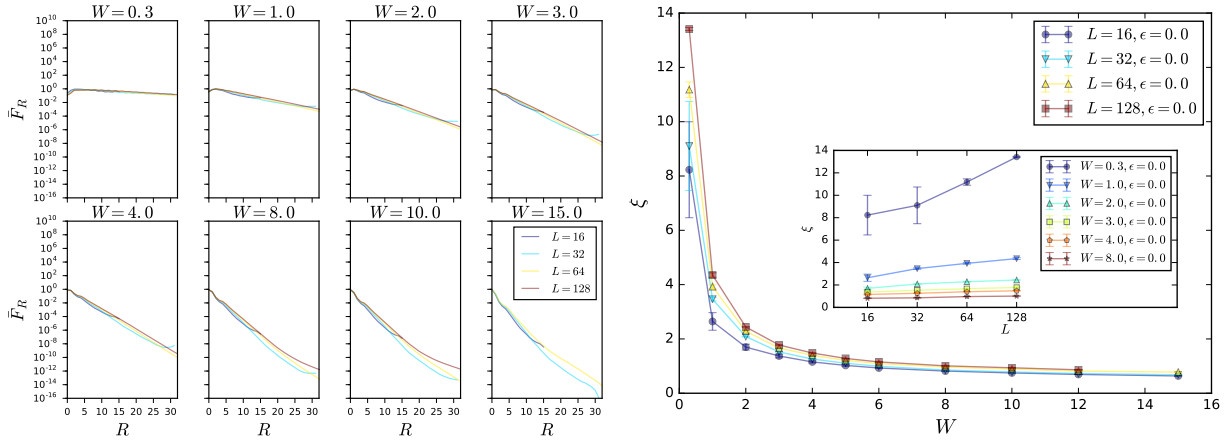

Figure A.1: *Left:* exponential decay of $\bar{F}_R$ for ground states. *Right:* correlation length ξ for ground states. ξ is a monotonically increasing function of the system size L at small disorder.

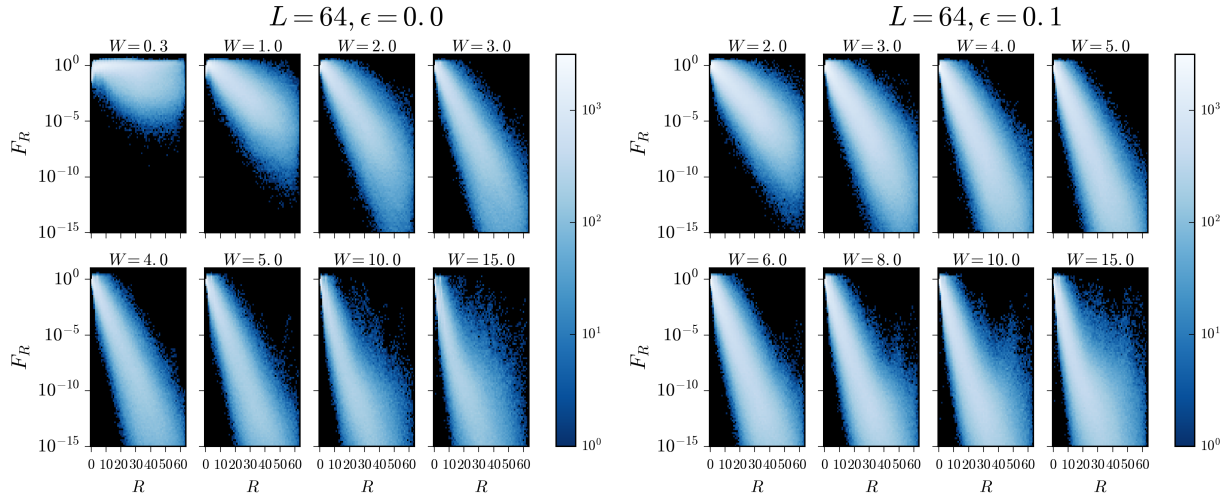

Figure A.2: Histogram of F_R vs. R for systems of size $L = 64$ at different values of W and eigenstates at $\epsilon = 0.0, 0.1$.

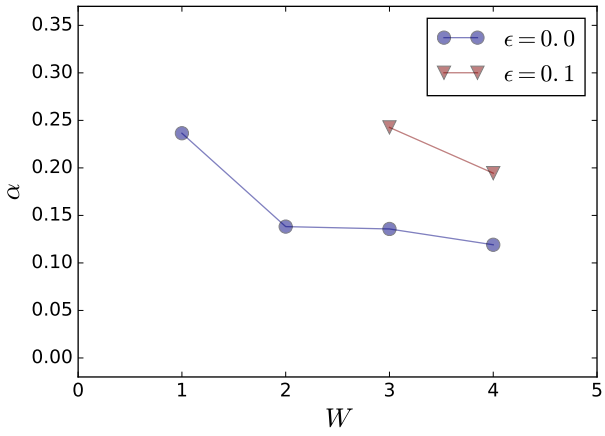

Figure A.3: Exponent α of the scaling law $\xi = \log(\beta L^{\alpha})$ for the correlation length of the OPOs.

Appendix B

Exponential decay of the OPOs

Assuming that the asymptotic exponential decay of the averaged $\bar{F}_R$ is representative of a typical OPO, we have $F_R \propto e^{-R/\xi}$ for a particular OPO k, where $R \equiv \max(|i-m|, |j-m|)$ and m is the localization center, *i.e.* the site with the maximum amplitude $\left|U^\dagger_{km}\right|$. F_R is defined as the total contribution from range R to the definition of $a^\dagger_k a_k$:

$$F_R \equiv \sum_{\max(|i-m|,|j-m|)=R} \left|f^k_{ij}\right|, \tag{B.1}$$

where $f^k_{ij} \equiv U^\dagger_{ki} U_{jk}$. Using the fact that f^k_{ij} is a hermitian matrix in indices i and j, Eq. (B.1) can be rewritten as:

$$\begin{aligned} F_R = 2 \times \sum_{i\in(m-R,m+R)} \left|f^k_{m-R,i}\right| + 2 \times \sum_{i\in(m-R,m+R)} \left|f^k_{m+R,i}\right| + 2 \times \left|f^k_{m-R,m+R}\right| \\ + \left|f^k_{m-R,m-R}\right| + \left|f^k_{m+R,m+R}\right|. \end{aligned} \tag{B.2}$$

Furthermore, if we assume that the decay of the OPO is symmetric to both sides of site m, Eq. (B.2) becomes:

$$F_R = 4 \times \sum_{i\in(m-R,m+R)} \left|f^k_{m-R,i}\right| + 4 \times \left|f^k_{m-R,m-R}\right|, \tag{B.3}$$

which is expressed in terms of $U^\dagger$ (note that in our case $U^\dagger = U^T$, since U has only real coefficients) as:

$$\begin{aligned} F_R &= 4 \times \sum_{i\in(m-R,m+R)} \left|U^\dagger_{k,m-R} U^\dagger_{k,i}\right| + 4 \times \left|U^\dagger_{k,m-R} U^\dagger_{k,m-R}\right| \\ &= 4 \left|U^\dagger_{k,m-R}\right| \times \sum_{i\in[m-R,m+R)} \left|U^\dagger_{k,i}\right| \\ &= 4 \left|U^\dagger_{k,m-R}\right| \times \left(\left|U^\dagger_{k,m-R}\right| + \left|U^\dagger_{k,m}\right| + 2 \times \sum_{i\in(m-R,0)} \left|U^\dagger_{k,i}\right| \right), \end{aligned} \tag{B.4}$$

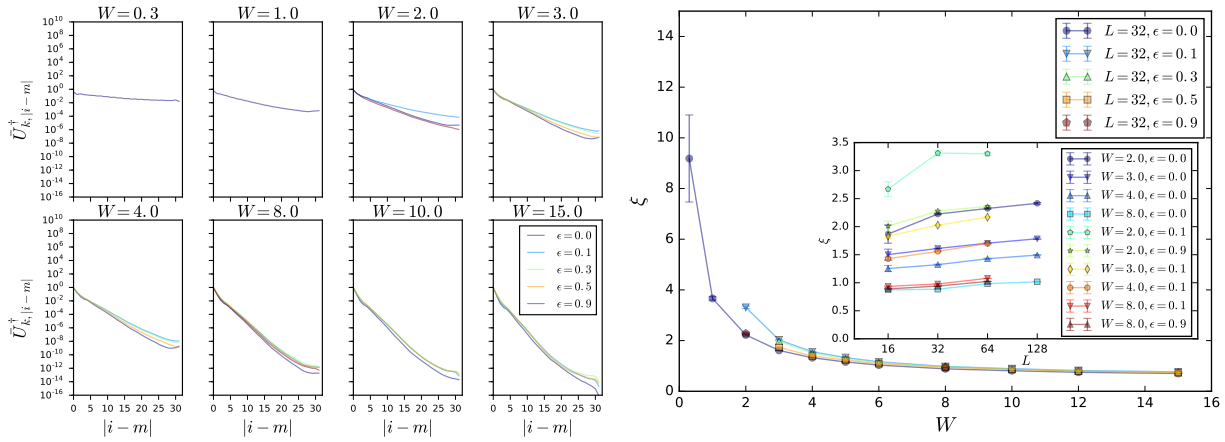

Figure B.1: Average decay of the OPOs' tails ($L = 32$). The asymptotic behavior of the tails is equal to the one of $\bar{F}_R$ presented in Fig. 3.4.

which by assumption has to decay as $e^{-R/\xi}$. Solving for the decay of $\left|U^{\dagger}_{(k,m-R)}\right|$ as $m - R$ gets away from m we get:

$$\left|U^{\dagger}_{k,m-R}\right| \propto e^{-R/\xi} \left(\left|U^{\dagger}_{k,m-R}\right| + \left|U^{\dagger}_{k,m}\right| + 2 \sum_{i \in (m-R,0)} \left|U^{\dagger}_{k,i}\right| \right)^{-1}. \tag{B.5}$$

It is clear from Eq. (B.4) (third line) that $\left|U^{\dagger}_{k,m-R}\right|$ decays at least as fast as $e^{-R/\xi}$ as a function of R, and so the sum $2\sum_{i\in(m-R,0)} \left|U^{\dagger}_{k,i}\right| + \left|U^{\dagger}_{k,m-R}\right|$ is convergent (in the limit $R \to \infty$). We end up with the functional form:

$$\left|U^{\dagger}_{k,m-R}\right| \propto \frac{e^{-R/\xi}}{A + B \cdot g(R)}, \tag{B.6}$$

where A and B are positive constants and $g(R)$ is a monotonically increasing function with the limits $g(0) = 0$ and $g(\infty) = 1$. Therefore, the weight of the number operators of the OPOs (F_R) and the OPOs themselves (as one particle wave functions) have the same asymptotic exponential behavior, with the same correlation length ξ.

As we can see in Fig. B.1, the (logarithmically) averaged decay of the tails of the OPOs is extremely similar, and equal asymptotically, to the one of $\bar{F}_R$ presented in Fig. 3.4.

Appendix C

Supplementary data on the support of the OPOs

Here we consider the distribution of the $support_{90}$ of the OPOs at different system sizes (see Fig. C.1). While at strong disorder the distributions are pretty much system size independent and decay exponentially with $support_{90}$, at small disorder they clearly suffer from finite size effects and collapse to the system size. Also, in the weak disorder limit the exponential decay seems to be lost, although it might be masked by the finite size effects on the distributions.

The definition of the support ($support_{90}$) involves the arbitrary choice of a region containing 90% of the norm of the OPO. An alternative way of defining the support of an OPO, which is less intuitive but does not depend on an arbitrary choice of some sort of threshold, is by considering its number operator $a_k^\dagger a_k$. We define its *support* as the average range R weighted by F_R:

$$support \equiv \frac{\sum_R F_R R}{\sum_R F_R}, \tag{C.1}$$

which is equivalent to the average range of the string operators that define the number operator $a_k^\dagger a_k$ (see Eq. (3.4)) weighted by their amplitude $\left|f_{ij}^k\right|$; this is analogous to the definition for l-bits from Ref. [40], but our range R always includes the distance to the center, as is presented in Ref. [2] (see Appendix F for more details). Both Figs. C.2 and C.3 show that the already discussed phenomenology captured by the $support_{90}$ is extremely similar to the one captured by the *support* of Eq. (C.1). For a given OPO, its *support* is usually smaller than its $support_{90}$ due to the fact that the average over ranges will make the *support* take roughly half of the value of the $support_{90}$; we can easily see this trend in the figures.

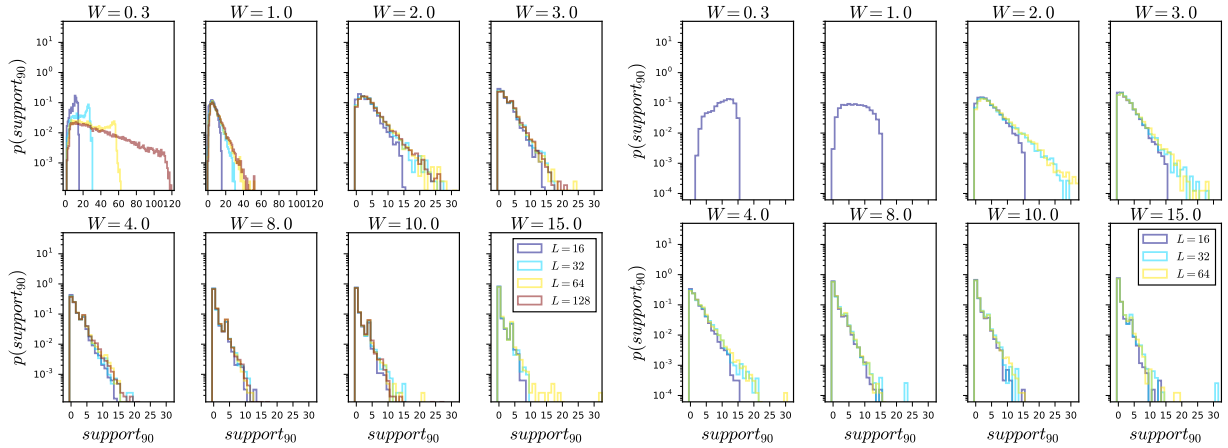

Figure C.1: Distribution of the $support_{90}$ of the OPOs of eigenstates at $\epsilon = 0.0$ (left) and $\epsilon = 0.1$ (right) of systems of different sizes L. At strong disorder the distribution decays exponentially and is largely system size independent, while it collapses to the system size at weak disorder, where the exponential decay is lost.

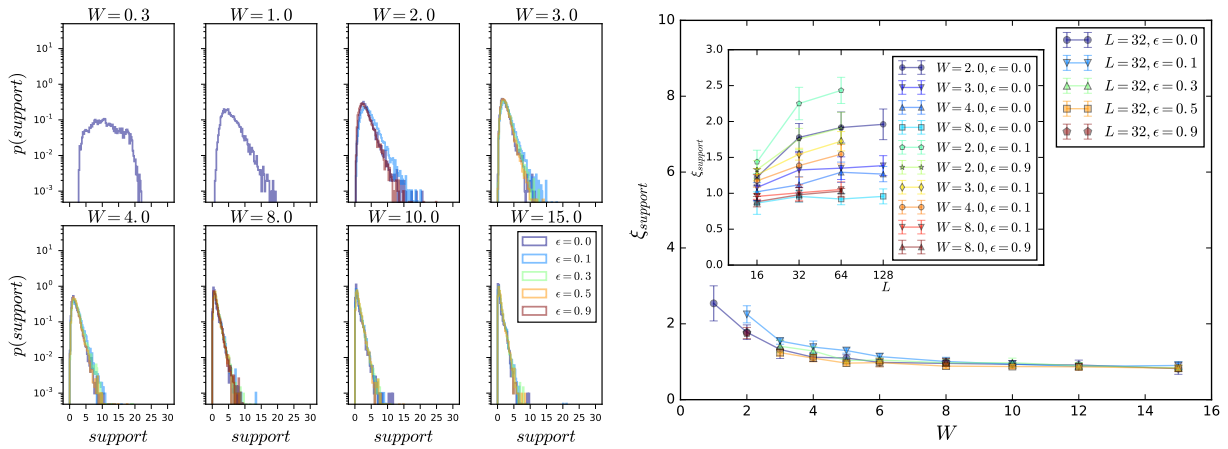

Figure C.2: Equivalent to Fig. 3.6 ($L = 32$ is considered in the left panel). The support ($support$) is now computed for the number operator of the OPO $a_k^\dagger a_k$ as the average range R weighted by F_R. The phenomenology is extremely similar to the one found for the $support_{90}$ in Fig. 3.6 in Section. 3.6.1.

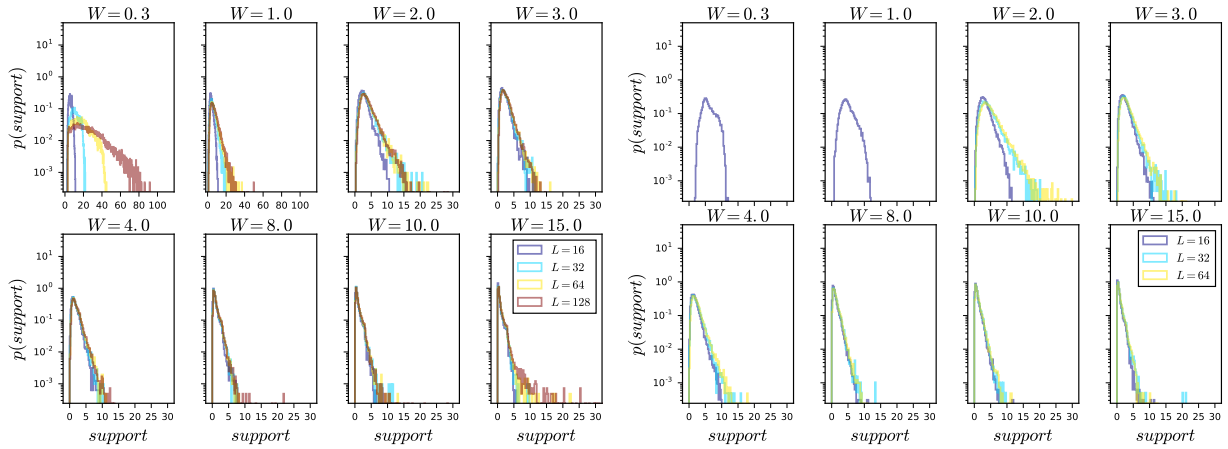

Figure C.3: Distribution of the *support* of the OPOs of systems of different size L at $\epsilon = 0.0$ (left) and $\epsilon = 0.1$ (right). The phenomenology is extremely similar to the one found in Fig. C.1.

Appendix D

System size independence of the distribution of the IPR

In Fig. D.1 we see that the distribution of the IPR is system size independent for $W \gtrapprox W_c$ and very slightly system size dependent at small disorder, where the OPOs delocalize and are affected by finite size effects, with a slight drift towards larger IPR for smaller systems.

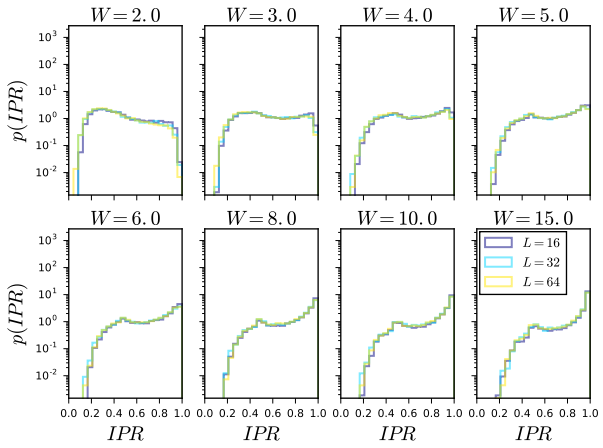

Figure D.1: Histogram of the distribution of IPR for different system sizes at $\epsilon = 0.1$. The distribution is system size independent for almost all values of W, with only a slight drift towards high IPR for small systems at $W = 2$.

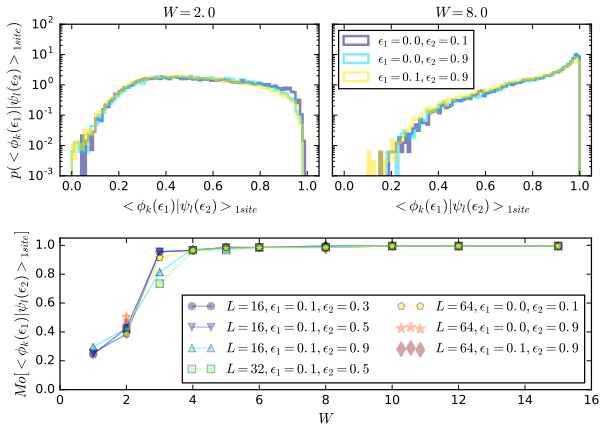

Figure D.2: *Top:* distribution of the biggest one site contribution to the overlaps between corresponding OPOs ($k \leftrightarrow l(k)$) obtained from pairs of eigenstates of the same Hamiltonian at two particular energy densities ϵ_1 and ϵ_2 ($L = 64$). *Bottom:* mode of the distribution of the one site contributions to the overlaps for different pairs of energy densities as a function of W. The one site overlap is lower than the total overlap between the OPOs.

Appendix E

Supplementary data on the OPOs' overlaps

The high overlap between OPOs at different energy densities could be due to the localized form of the OPOs, which might match trivially with one another at their center. However, we show in this appendix that their overlap is benefited from the particular shape of OPOs' tails, and is not only due to the overlap coming from two OPOs centered at the same site. To study this we define the leading one site contribution to the overlap between two OPOs at different energy densities ϵ_1 and ϵ_2 as:

$$\langle \phi_k(\epsilon_1) | \psi_l(\epsilon_2) \rangle_{1site} \equiv \max \left\{ \left| U(\epsilon_1)_{ik} U^\dagger(\epsilon_2)_{li} \right| \right\}_{i \in [0, L-1]} \tag{E.1}$$

where $|\phi_k(\epsilon_1)\rangle = \sum_i U^\dagger(\epsilon_1)_{ki} |i\rangle$ and $|\psi_l(\epsilon_2)\rangle = \sum_i U^\dagger(\epsilon_2)_{li} |i\rangle$. We can see in the top panel of Fig. D.2 that the distribution of the main one site contribution to the overlaps between corresponding OPOs ($k \leftrightarrow l(k)$) is always substantially lower than the total overlap over the entire chain (compare with Fig. 3.13 in Section 3.6.3). The pairs of OPOs match therefore both at their center and throughout their tails in a non-trivial way. The bottom panel of Fig. D.2 shows the mode of the distribution of overlaps as a function of W. We see that for all pairs of energy densities depicted, and for all disorder strengths, the typical overlap is higher than or equal to the typical best one site contribution. This is particularly noticeable at low disorder, where the mode of the one site overlaps drops substantially below 100% at $W = 3$, to 40.49% at $W = 2$ (as opposed to about 70% when the tails are considered for ϵ_1 far from ϵ_2) and below 30% at $W = 1$ and $L = 16$ (as opposed to $60 - 70\%$).

Appendix F

The different definitions of the range of the string operators of the OPOs

In this appendix we will discuss two different definitions of the range R. In either case, we will show how the "$1/f$" distribution of the coupling constants of the number operators of the OPOs is a consequence of the exponential decay of the OPOs in real space. We will also show the robustness to the two definitions of R of our results from Section 3.6.1 on the correlation length and the support of the OPOs.

In Section 3.6.1 we defined the range associated to the string of operators $c_i^\dagger c_j$ that contributes to the definition of the number operator of an OPO with its maximum amplitude at site m (see Eq. (3.4)) as $\max(|i-m|, |j-m|)$, in the spirit of the one for l-bits of Ref. [2]; we will call this the "centered" definition of the range. An alternative definition of the range is $R \equiv |i-j|$, which is considered in Refs. [40] and [71] for l-bits; we will call this the "uncentered" definition. The centered range takes into account the notion of an l-bit being localized around a site m in real space, and acting non-trivially mainly in a small region around this site. The uncentered range ignores this notion of a center, and relates the concept of localization to the idea of an l-bit acting non-trivially between sites contained in small regions in real space, but these regions can be many and lay anywhere on the chain. Both definitions are interesting in slightly different ways due to their different points of emphasis, but in practice they give rise to a very similar phenomenology. Their relation with the matrix f_{ij}^k of coupling constants of the number operator of an OPO is better understood graphically, with the aid of Fig. F.1, where only the elements of a range $R(i,j) = const.$ are shown (left panel for centered range and right panel for uncentered range). Let's first focus on the centered range, and leave the discussion of the uncentered range for later. It is easy to see that the elements of a constant range R correspond to squares of side $2R$ centered at (m,m). In addition, the elements within a particular square decay exponentially on each one of its four sides as either $\left|f_{ij}^k\right| \propto e^{-|i-m|/\xi}$ or $\left|f_{ij}^k\right| \propto e^{-|j-m|/\xi}$. As a consequence, the elements of constant R (that we denote by $|f_R|$) follow a distribution $p\left(\log|f_R|\right) = const.$, but that implies $p(|f_R|) = const./|f_R|$ due to $d\left(\log|f_R|\right)/d\left(p(f_R)\right) = 1/|f_R|$. If we consider an ensemble of exponentially decaying OPOs, the combined $p(|f_R|)$ will drop towards the ends, due to the individual distributions spanning different regions of the $|f_R|$ axis; we can see this in Fig. 3.4. We can see that the "$1/f$" distribution of the coupling constants of $a_k^\dagger a_k$ can be derived from the exponential decay of the OPOs

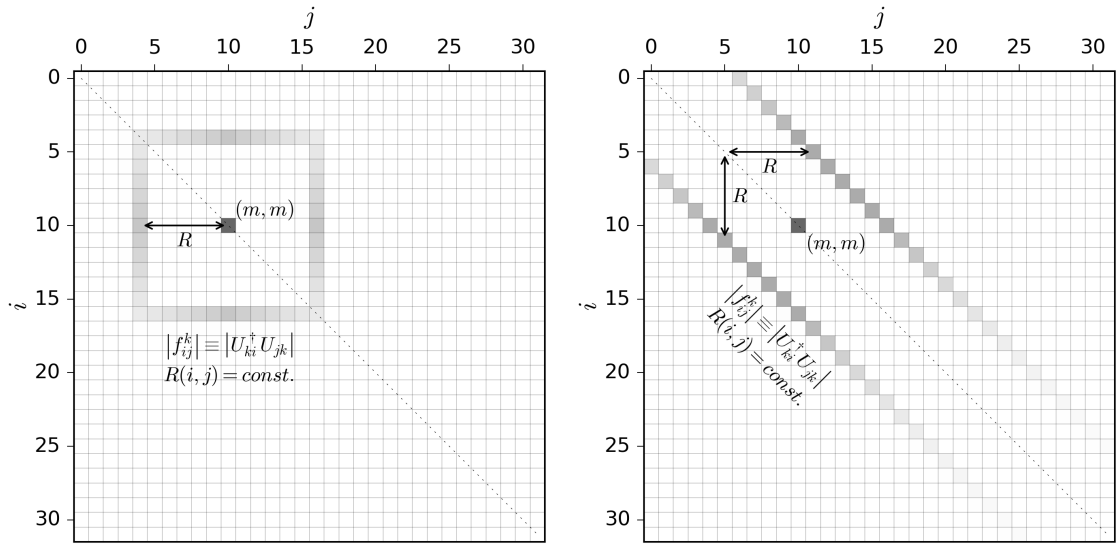

Figure F.1: Matrix $\left|f^k_{ij}\right| = \left|U^\dagger_{ki} U_{jk}\right|$ for a generic OPO with exponentially decaying $\left|U^\dagger_{ki}\right| \propto e^{-|i-m|/\xi}$ centered at site m. Only the elements for which the range $R(i,j) = const.$ are represented, where $R(i,j) \equiv \max(|i-m|, |j-m|)$ (centered) applies to the *left* panel, and $R(i,j) \equiv |i-j|$ (uncentered) applies to the *right* panel. In both example, $m = 10$ and $R = 6$ for a system of $L = 32$.

in real space. Finally, at small disorder the supports of the distributions $p(|f_R|)$ get narrower as a natural consequence of the slower decay of the OPOs in this limit (see Fig. 3.4).

Let's now focus on the uncentered range (right panel of Fig. F.1). The elements within the secondary diagonals of the matrix are now those with a constant R and decay exponentially as $e^{-(|i-m|+|j-m|)/\xi}$, which drops twice as fast as the OPO's amplitudes due to the simultaneous change of i and j along the diagonal. The distribution $p(|f_R|) \propto 1/|f_R|$ for a fixed R still holds (see Fig. F.2) due to the same argument discussed for the centered range case, although now the tails of the $|f_R|$ diagonals get shorter as R is increased, due to the finite size of the system (as opposed to the squares of the centered range, which did grow in size with R). This causes the supports of the distributions $p(|f_R|)$ to become narrower as the range R is increased, contrary to the expectations for the centered range.

It is easy to see that the total contribution F_R of a particular (uncentered) range to $a^\dagger_k a_k$ (see Eq. (3.6)), *i.e.* the sum of all elements in the diagonals shown in the right panel of Fig. F.1, decays exponentially with R as $e^{-R/\xi}$ for big enough systems, as was the case with the centered range. This is demonstrated for the (logarithmic) average $\bar{F}_R$ in Fig. F.3, where little difference is found as compared to Fig. 3.4 of Section 3.6.1 (where the centered range is used). The $\bar{F}_R$ curves are slightly concave at large R, which we think is due to the shortening of the tails of the $|f_R|$ diagonals with R.

The *support* (see Eq. (C.1)) is also robust to the change in the definition of the range. We demonstrate

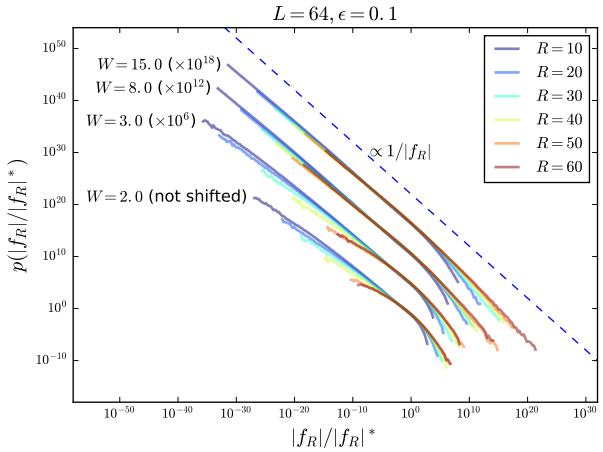

Figure F.2: Equivalent to Fig. 3.5, but computed using the uncentered range. Contrary to Fig. 3.5, the distributions of $|f_R|$ are broader and flatter at small ranges, as discussed in Appendix F.

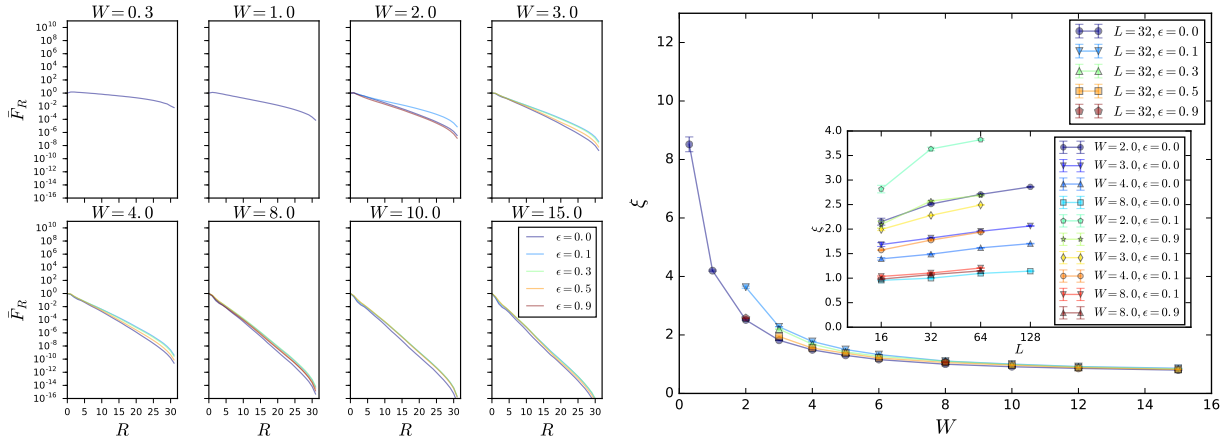

Figure F.3: Equivalent to Fig. 3.4, although the uncentered definition of the range R is used ($L = 32$ is considered in the left panel).

in Figs. F.4 and F.5 that the phenomenology (using the uncentered range) is similar to the one found with the centered definition of the range in Figs. C.2 and C.3, and hence to the one discussed in Section 3.6.1 for the simpler $support_{90}$ (see Fig. 3.6 and Fig. C.1 of Appendix. C).

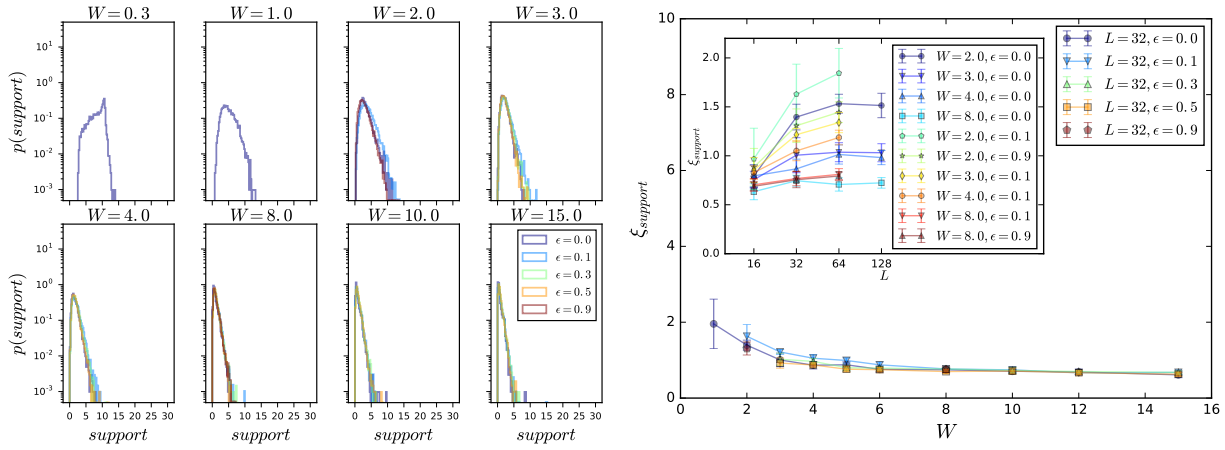

Figure F.4: Equivalent to Fig. C.2, although using the uncentered definition for the range R ($L = 32$ is considered in the left panel).

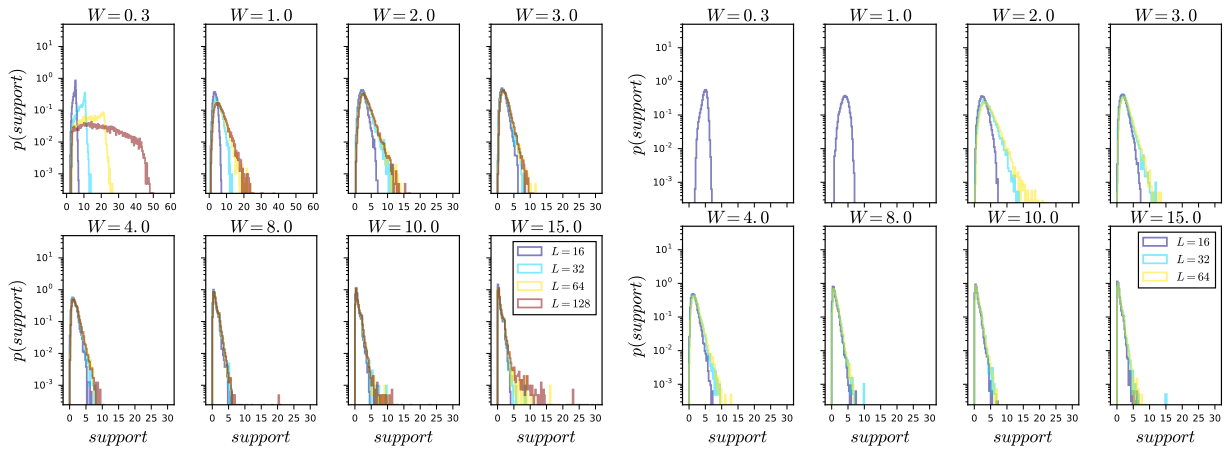

Figure F.5: Equivalent to Fig. C.3, but using the uncentered definition of the range R. $\epsilon = 0.0$ (left) and $\epsilon = 0.1$ (right) are considered.

Appendix G

Combinatorial counting of subsets of pseudo-spins as a function of range

In Section 4.4 we argued that the scaling of the $p(R, |A|)$ at strong $|A|$ as a function of range R was exponential in the ergodic phase, and well in agreement with a simple counting argument. Here we derive such combinatorial scaling by counting the possible pairs of sets of quantum numbers for each value of R.

First, note that two sets of quantum numbers have to disagree on an even number of sites, given the fact that we are working on the zero magnetization sector. Furthermore, the magnetization of the subset of disagreeing quantum numbers must also be zero, *i.e.*, have an equal number of up and down pseudo-spins. We can now proceed with the counting.

For a fixed range R, subsets can take any order $o = 2, 4, 6, \ldots R$, *i.e.*, they can involve an even number of pseudo-spins. For each order (number of sites involved), and ignoring cyclic permutations of the bit-strings, two of the disagreeing pseudo-spins have to be "pinned" at the left and right ends of the range R interval, leaving only freedom to the inner $o-2$ pseudo-spins to be placed at different intermediate sites; there are therefore $\binom{R-2}{o-2}$ ways to place them. This yields:

$$\sum_{\text{even } o}^{R} \binom{R-2}{o-2} \tag{G.1}$$

ways to place disagreeing pseudo-spins while forming a range R subset. There is another factor to take into account: once the o disagreeing pseudo-spins are place, now their orientations have to be chosen. Given that the magnetization of the o pseudo-spins is zero, there are $\binom{o}{o/2}$ ways to arrange them, multiplied by the possibilities over the agreeing pseudo-spins, which are $\binom{L-o}{(L-o)/2}$, and where L is the total number of sites in the system. We then get that the scaling is:

$$\propto \sum_{\text{even } o}^{R} \binom{R-2}{o-2}\binom{o}{o/2}\binom{L-o}{(L-o)/2}. \tag{G.2}$$

Finally, we have to account for tranlations of the bitstrings on the chain. Given open boundary conditions, the number of cyclic permutations allowed for a particular subset of range R is equal to $L-1-R$. We

finally have the right scaling:

$$\begin{aligned} &\propto \sum_{\text{even } o}^{R} \binom{R-2}{o-2}\binom{o}{o/2}\binom{L-o}{(L-o)/2}(L-1-R) \\ &\approx C2^R, \end{aligned} \tag{G.3}$$

for some constant C. This scaling formula was plotted in Fig. 4.1 for convenient comparison with the scaling of the contributing terms as a function of R in the ergodic phase. Note that, even though the exponent, α, of this expression tends to $\alpha \to 1$, where the counting is proportional to $2^{\alpha R}$, α is strongly dependent on L for small system sizes, and it can be measured numerically by a simple linear regression for the system sizes studied in this work. Fig. 4.1 plots the theoretical scaling for the ergodic phase (dashed lines) taking the finite size into account, *i.e.*, taking Eq. (G.3) exactly.

Appendix H

CDF of the second singular value of the bipartite reduced density matrix

Here we present data related to the extractin of the exponent γ for the CDF of the second entanglement eigenvalue, λ_2, when it approaches $\lambda_2 \to \log(2)^+$, which was discussed in Section 5.4. In particular, Figs. H.1, H.2, and H.3 linear regression results of the fit on a log-log plot to the left-side tails of $p(\lambda_2)$ as a function of $\lambda_2 - \log(2)$. The slope of this fit is equal to γ. In order to estimate the error bars for γ, we perform a bootstrapping analysis with 200 resamples over disorder realizations. The inset of the figures provides the distribution of γ from bootstrapping; its standard deviation is taken as an estimate of the error on the estimation of γ.

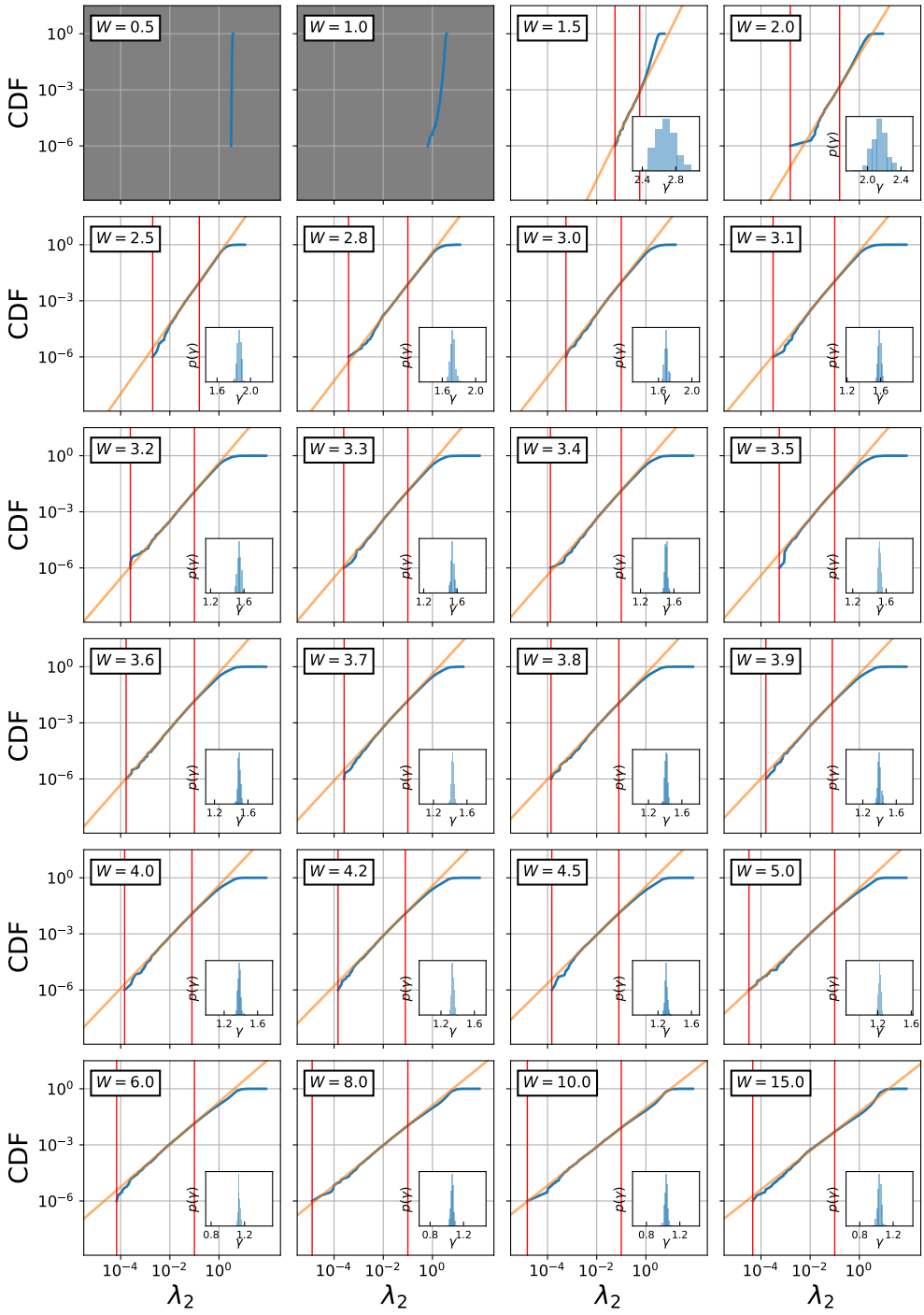

Figure H.1: Linear fits of the log-log representation of the left-side tail of the CDF of the second eigenvalue of the bipartite reduced density matrix of a system os size $L = 18$. Red vertical lines denote the ends of the interval that contains the points used in each case to make the fit. The slope of the fit gives us the exponent γ in the relation $CDF(\lambda_2) \approx (\lambda_2 - \log(2))^{\gamma}$, or equivalently $PDF(\lambda_2) \approx (\lambda_2 - \log(2))^{\gamma-1}$. Below $W = 1.5$, the low λ_2 data is inexistent and we do not attempt to extract an exponent γ from a linear fit. **Inset:** probability distribution of γ extracted from 200 bootstrap resamples over the 10K disorder realizations. Bootstrapping was used in order to compute conficence intervals for γ, shown in Fig. 5.9.

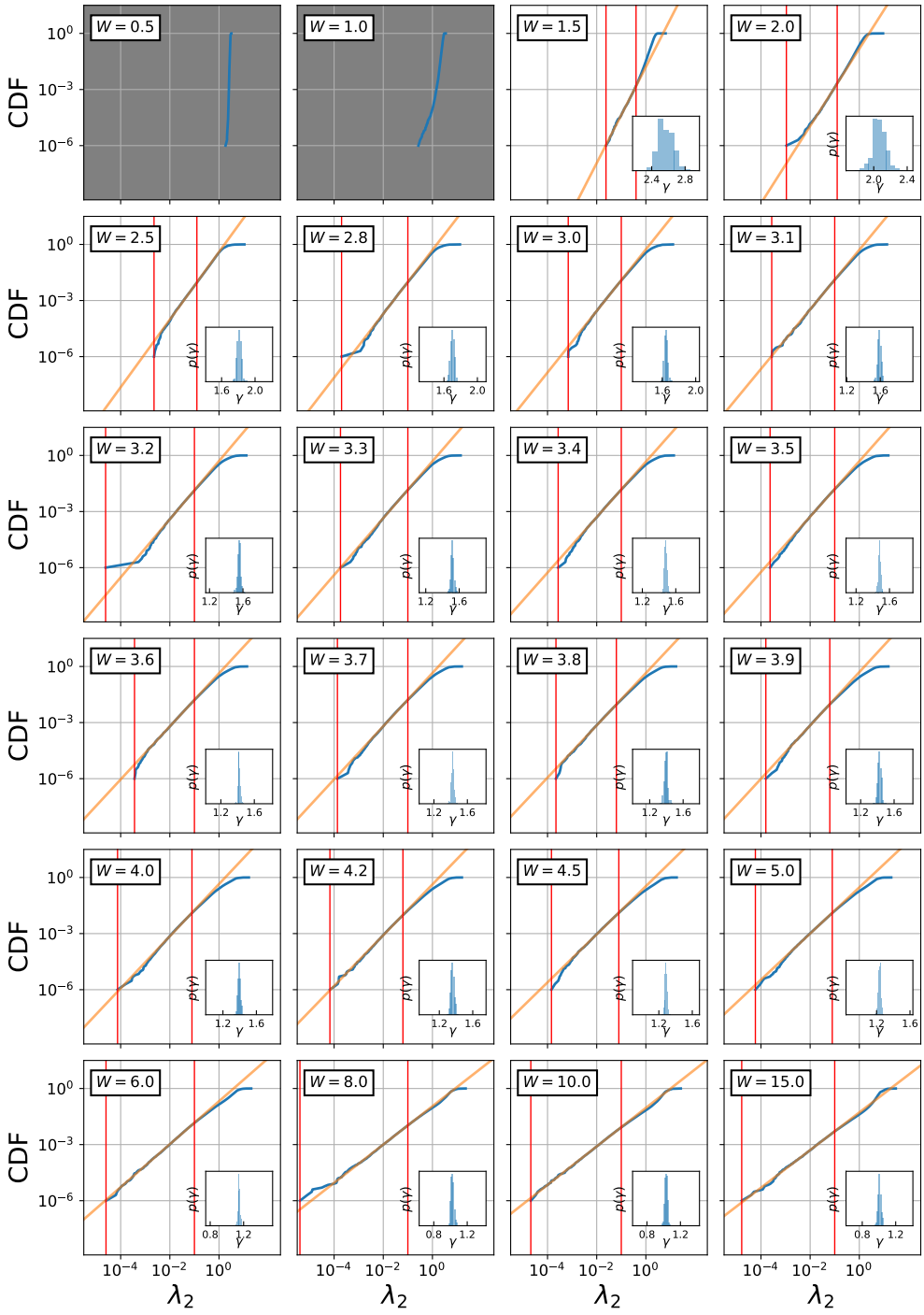

Figure H.2: Same as Fig. H.1 for systems of size $L = 16$. **Inset:** probability distribution of γ extracted from 200 bootstrap resamples over the 200K disorder realizations.

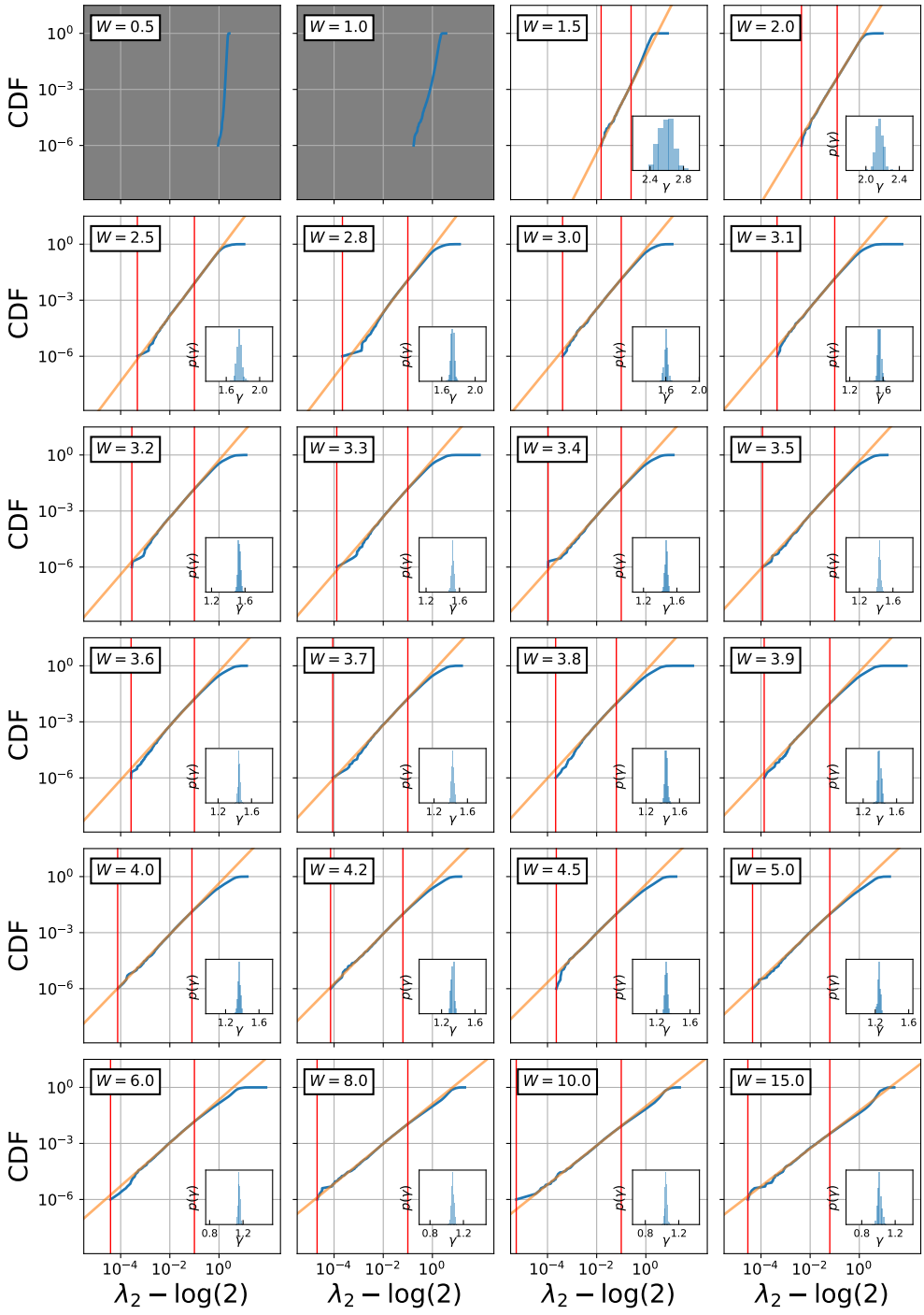

Figure H.3: Same as Fig. H.1 for systems of size $L = 14$. **Inset:** probability distribution of γ extracted from 200 bootstrap resamples over the 200K disorder realizations.

Bibliography

[1] D. A. Abanin, J. H. Bardarson, G. De Tomasi, S. Gopalakrishnan, V. Khemani, S. A. Parameswaran, F. Pollmann, A. C. Potter, M. Serbyn, and R. Vasseur. Distinguishing localization from chaos: challenges in finite-size systems. *arXiv:1911.04501 [cond-mat]*, November 2019. arXiv: 1911.04501.

[2] Dmitry A. Abanin and Zlatko Papić. Recent progress in many-body localization. *Annalen der Physik*, 529(7):1700169, July 2017.

[3] Kartiek Agarwal, Ehud Altman, Eugene Demler, Sarang Gopalakrishnan, David A. Huse, and Michael Knap. Rare-region effects and dynamics near the many-body localization transition. *Annalen der Physik*, 529(7):1600326, July 2017.

[4] Kartiek Agarwal, Sarang Gopalakrishnan, Michael Knap, Markus Müller, and Eugene Demler. Anomalous Diffusion and Griffiths Effects Near the Many-Body Localization Transition. *Physical Review Letters*, 114(16):160401, April 2015.

[5] Fabien Alet and Nicolas Laflorencie. Many-body localization: An introduction and selected topics. *Comptes Rendus Physique*, 19(6):498–525, September 2018.

[6] Ehud Altman and Ronen Vosk. Universal Dynamics and Renormalization in Many-Body-Localized Systems. *Annual Review of Condensed Matter Physics*, 6(1):383–409, 2015.

[7] P. W. Anderson. Absence of Diffusion in Certain Random Lattices. *Physical Review*, 109(5):1492–1505, March 1958.

[8] Yevgeny Bar Lev, Guy Cohen, and David R. Reichman. Absence of Diffusion in an Interacting System of Spinless Fermions on a One-Dimensional Disordered Lattice. *Physical Review Letters*, 114(10):100601, March 2015.

[9] Yevgeny Bar Lev and David R. Reichman. Dynamics of many-body localization. *Physical Review B*, 89(22):220201, June 2014.

[10] Jens H. Bardarson, Frank Pollmann, and Joel E. Moore. Unbounded Growth of Entanglement in Models of Many-Body Localization. *Physical Review Letters*, 109(1):017202, July 2012.

[11] D. M. Basko, I. L. Aleiner, and B. L. Altshuler. Metal–insulator transition in a weakly interacting many-electron system with localized single-particle states. *Annals of Physics*, 321(5):1126–1205, May 2006.

[12] Bela Bauer and Chetan Nayak. Area laws in a many-body localized state and its implications for topological order. *Journal of Statistical Mechanics: Theory and Experiment*, 2013(09):P09005, 2013.

[13] Soumya Bera, Thomas Martynec, Henning Schomerus, Fabian Heidrich-Meisner, and Jens H. Bardarson. One-particle density matrix characterization of many-body localization. *Annalen der Physik*, 529(7):1600356, July 2017.

[14] Soumya Bera, Henning Schomerus, Fabian Heidrich-Meisner, and Jens H. Bardarson. Many-Body Localization Characterized from a One-Particle Perspective. *Physical Review Letters*, 115(4):046603, July 2015.

[15] Timothy C. Berkelbach and David R. Reichman. Conductivity of disordered quantum lattice models at infinite temperature: Many-body localization. *Physical Review B*, 81(22):224429, June 2010.

[16] Jacob Biamonte. Lectures on Quantum Tensor Networks. *arXiv:1912.10049 [cond-mat, physics:math-ph, physics:quant-ph]*, December 2019. arXiv: 1912.10049.

[17] Jean-Paul Blaizot and Georges Ripka. *Quantum theory of finite systems*, volume 3. MIT press Cambridge, 1986.

[18] Pranjal Bordia, Henrik Lüschen, Sebastian Scherg, Sarang Gopalakrishnan, Michael Knap, Ulrich Schneider, and Immanuel Bloch. Probing slow relaxation and many-body localization in two-dimensional quasiperiodic systems. *Physical Review X*, 7(4):041047, 2017.

[19] F. Borgonovi, F. M. Izrailev, L. F. Santos, and V. G. Zelevinsky. Quantum chaos and thermalization in isolated systems of interacting particles. *Physics Reports*, 626:1–58, April 2016.

[20] A. Chandran, J. Carrasquilla, I. H. Kim, D. A. Abanin, and G. Vidal. Spectral tensor networks for many-body localization. *Physical Review B*, 92(2):024201, July 2015.

[21] A. Chandran, A. Pal, C. R. Laumann, and A. Scardicchio. Many-body localization beyond eigenstates in all dimensions. *Physical Review B*, 94(14):144203, October 2016.

[22] Anushya Chandran, Isaac H. Kim, Guifre Vidal, and Dmitry A. Abanin. Constructing local integrals of motion in the many-body localized phase. *Physical Review B*, 91(8):085425, February 2015.

[23] Gabriele De Chiara, Simone Montangero, Pasquale Calabrese, and Rosario Fazio. Entanglement entropy dynamics of Heisenberg chains. *Journal of Statistical Mechanics: Theory and Experiment*, 2006(03):P03001, 2006.

[24] B. Chiaro, C. Neill, A. Bohrdt, M. Filippone, F. Arute, K. Arya, R. Babbush, D. Bacon, J. Bardin, R. Barends, S. Boixo, D. Buell, B. Burkett, Y. Chen, Z. Chen, R. Collins, A. Dunsworth, E. Farhi, A. Fowler, B. Foxen, C. Gidney, M. Giustina, M. Harrigan, T. Huang, S. Isakov, E. Jeffrey, Z. Jiang, D. Kafri, K. Kechedzhi, J. Kelly, P. Klimov, A. Korotkov, F. Kostritsa, D. Landhuis, E. Lucero, J. McClean, X. Mi, A. Megrant, M. Mohseni, J. Mutus, M. McEwen, O. Naaman, M. Neeley, M. Niu, A. Petukhov, C. Quintana, N. Rubin, D. Sank, K. Satzinger, A. Vainsencher, T. White, Z. Yao, P. Yeh, A. Zalcman, V. Smelyanskiy, H. Neven, S. Gopalakrishnan, D. Abanin, M. Knap, J. Martinis, and P. Roushan. Growth and preservation of entanglement in a many-body localized system. *arXiv:1910.06024 [cond-mat, physics:quant-ph]*, October 2019. arXiv: 1910.06024.

[25] Jae-yoon Choi, Sebastian Hild, Johannes Zeiher, Peter Schauß, Antonio Rubio-Abadal, Tarik Yefsah, Vedika Khemani, David A. Huse, Immanuel Bloch, and Christian Gross. Exploring the many-body localization transition in two dimensions. *Science*, 352(6293):1547–1552, June 2016.

[26] Luca D'Alessio, Yariv Kafri, Anatoli Polkovnikov, and Marcos Rigol. From quantum chaos and eigenstate thermalization to statistical mechanics and thermodynamics. *Advances in Physics*, 65(3):239–362, May 2016.

[27] Wojciech De Roeck, Francois Huveneers, Markus Müller, and Mauro Schiulaz. Absence of many-body mobility edges. *Physical Review B*, 93(1):014203, January 2016.

[28] Wojciech De Roeck and François Huveneers. Stability and instability towards delocalization in many-body localization systems. *Physical Review B*, 95(15):155129, April 2017.

[29] Wojciech De Roeck and John Z. Imbrie. Many-body localization: stability and instability. *Philosophical Transactions of the Royal Society A: Mathematical, Physical and Engineering Sciences*, 375(2108):20160422, December 2017.

[30] Giuseppe De Tomasi, Soumya Bera, Jens H. Bardarson, and Frank Pollmann. Quantum Mutual Information as a Probe for Many-Body Localization. *Physical Review Letters*, 118(1):016804, January 2017.

[31] J. M. Deutsch. Quantum statistical mechanics in a closed system. *Physical Review A*, 43(4):2046–2049, February 1991.

[32] Trithep Devakul, Vedika Khemani, Frank Pollmann, David Huse, and Shivaji Sondhi. Obtaining highly excited eigenstates of the localized XX chain via DMRG-X. *arXiv:1702.07721 [cond-mat, physics:quant-ph]*, February 2017. arXiv: 1702.07721.

[33] Daniel S. Fisher. Random antiferromagnetic quantum spin chains. *Physical Review B*, 50(6):3799–3821, August 1994.

[34] L. Fleishman and P. W. Anderson. Interactions and the Anderson transition. *Physical Review B*, 21(6):2366–2377, March 1980.

[35] I. V. Gornyi, A. D. Mirlin, and D. G. Polyakov. Interacting Electrons in Disordered Wires: Anderson Localization and Low-T Transport. *Physical Review Letters*, 95(20):206603, November 2005.

[36] Johnnie Gray, Sougato Bose, and Abolfazl Bayat. Many-body localization transition: Schmidt gap, entanglement length, and scaling. *Physical Review B*, 97(20):201105, May 2018.

[37] Qiujiang Guo, Chen Cheng, Zheng-Hang Sun, Zixuan Song, Hekang Li, Zhen Wang, Wenhui Ren, Hang Dong, Dongning Zheng, Yu-Ran Zhang, Rubem Mondaini, Heng Fan, and H. Wang. Observation of energy resolved many-body localization. *arXiv:1912.02818 [cond-mat, physics:quant-ph]*, December 2019. arXiv: 1912.02818.

[38] Loïc Herviou, Soumya Bera, and Jens H. Bardarson. Multiscale entanglement clusters at the many-body localization phase transition. *arXiv:1811.01925 [cond-mat]*, November 2018. arXiv: 1811.01925.

[39] Weifeng Hu and Garnet Kin-Lic Chan. Excited-State Geometry Optimization with the Density Matrix Renormalization Group, as Applied to Polyenes. *Journal of Chemical Theory and Computation*, 11(7):3000–3009, July 2015.

[40] David A. Huse, Rahul Nandkishore, and Vadim Oganesyan. Phenomenology of fully many-body-localized systems. *Physical Review B*, 90(17):174202, November 2014.

[41] John Z. Imbrie, Valentina Ros, and Antonello Scardicchio. Local integrals of motion in many-body localized systems. *Annalen der Physik*, 529(7):1600278, July 2017.

[42] Stephen Inglis and Lode Pollet. Accessing Many-Body Localized States through the Generalized Gibbs Ensemble. *Physical Review Letters*, 117(12):120402, September 2016.

[43] D. M. Kennes and C. Karrasch. Entanglement scaling of excited states in large one-dimensional many-body localized systems. *Physical Review B*, 93(24):245129, June 2016.

[44] Vedika Khemani, S. P. Lim, D. N. Sheng, and David A. Huse. Critical Properties of the Many-Body Localization Transition. *Physical Review X*, 7(2):021013, April 2017.

[45] Vedika Khemani, Frank Pollmann, and S. L. Sondhi. Obtaining Highly Excited Eigenstates of Many-Body Localized Hamiltonians by the Density Matrix Renormalization Group Approach. *Physical Review Letters*, 116(24):247204, June 2016.

[46] Vedika Khemani, D. N. Sheng, and David A. Huse. Two universality classes for the many-body localization transition. *Physical Review Letters*, 119(7), August 2017. arXiv: 1702.03932.

[47] Jonas A. Kjäll, Jens H. Bardarson, and Frank Pollmann. Many-Body Localization in a Disordered Quantum Ising Chain. *Physical Review Letters*, 113(10):107204, September 2014.

[48] S.Go S. Kondov, W. R. McGehee, W. Xu, and B. DeMarco. Disorder-Induced Localization in a Strongly Correlated Atomic Hubbard Gas. *Physical Review Letters*, 114(8):083002, February 2015.

[49] Nicolas Laflorencie. Scaling of entanglement entropy in the random singlet phase. *Physical Review B*, 72(14):140408, October 2005.

[50] Rich Lehoucq, Kristi Maschhoff, Danny Sorensen, and Chao Yang. Arpack software. *Website: http://www. caam. rice. edu/software/ARPACK*, 2007.

[51] Elliott H Lieb and Derek W Robinson. The finite group velocity of quantum spin systems. In *Statistical mechanics*, pages 425–431. Springer, 1972.

[52] S. P. Lim and D. N. Sheng. Many-body localization and transition by density matrix renormalization group and exact diagonalization studies. *Physical Review B*, 94(4):045111, July 2016.

[53] Sheng-Hsuan Lin, B. Sbierski, F. Dorfner, C. Karrasch, and F. Heidrich-Meisner. Many-body localization of spinless fermions with attractive interactions in one dimension. *arXiv:1707.06759 [cond-mat]*, July 2017. arXiv: 1707.06759.

[54] David J. Luitz. Long tail distributions near the many-body localization transition. *Physical Review B*, 93(13):134201, April 2016.

[55] David J. Luitz and Yevgeny Bar Lev. Anomalous Thermalization in Ergodic Systems. *Physical Review Letters*, 117(17):170404, October 2016.

[56] David J. Luitz and Yevgeny Bar Lev. The ergodic side of the many-body localization transition. *Annalen der Physik*, 529(7):1600350, July 2017.

[57] David J. Luitz and Yevgeny Bar Lev. Information propagation in isolated quantum systems. *Physical Review B*, 96(2):020406, July 2017.

[58] David J. Luitz, François Huveneers, and Wojciech de Roeck. How a small quantum bath can thermalize long localized chains. *arXiv:1705.10807 [cond-mat]*, May 2017. arXiv: 1705.10807.

[59] David J. Luitz, Nicolas Laflorencie, and Fabien Alet. Many-body localization edge in the random-field Heisenberg chain. *Physical Review B*, 91(8):081103, February 2015.

[60] David J. Luitz, Nicolas Laflorencie, and Fabien Alet. Extended slow dynamical regime close to the many-body localization transition. *Physical Review B*, 93(6):060201, February 2016.

[61] Cecile Monthus. Many-Body-Localization : Strong Disorder perturbative approach for the Local Integrals of Motion. *arXiv:1705.07570 [cond-mat]*, May 2017. arXiv: 1705.07570.

[62] Cécile Monthus. Level repulsion exponent$\upbeta$for many-body localization transitions and for Anderson localization transitions via Dyson Brownian motion. *Journal of Statistical Mechanics: Theory and Experiment*, 2016(3):033113, March 2016.

[63] Rahul Nandkishore and David A. Huse. Many-Body Localization and Thermalization in Quantum Statistical Mechanics. *Annual Review of Condensed Matter Physics*, 6(1):15–38, 2015.

[64] Vadim Oganesyan and David A. Huse. Localization of interacting fermions at high temperature. *Physical Review B*, 75(15):155111, April 2007.

[65] Roman Orus. Advances on Tensor Network Theory: Symmetries, Fermions, Entanglement, and Holography. *The European Physical Journal B*, 87(11):280, November 2014. arXiv: 1407.6552.

[66] Román Orús. A practical introduction to tensor networks: Matrix product states and projected entangled pair states. *Annals of Physics*, 349:117–158, 2014.

[67] Arijeet Pal and David A. Huse. Many-body localization phase transition. *Physical Review B*, 82(17):174411, November 2010.

[68] Rajat K. Panda, Antonello Scardicchio, Maximilian Schulz, Scott R. Taylor, and Marko Žnidarič. Can we study the many-body localisation transition? *arXiv:1911.07882 [cond-mat]*, November 2019. arXiv: 1911.07882.

[69] S. A. Parameswaran, Andrew C. Potter, and Romain Vasseur. Eigenstate phase transitions and the emergence of universal dynamics in highly excited states. *Annalen der Physik*, 529(7):1600302, July 2017.

[70] David Pekker and Bryan K. Clark. Encoding the structure of many-body localization with matrix product operators. *Physical Review B*, 95(3):035116, January 2017.

[71] David Pekker, Bryan K. Clark, Vadim Oganesyan, and Gil Refael. Fixed Points of Wegner-Wilson Flows and Many-Body Localization. *Physical Review Letters*, 119(7):075701, August 2017.

[72] David Pekker, Gil Refael, Ehud Altman, Eugene Demler, and Vadim Oganesyan. Hilbert-Glass Transition: New Universality of Temperature-Tuned Many-Body Dynamical Quantum Criticality. *Physical Review X*, 4(1):011052, March 2014.

[73] Oliver Penrose and Lars Onsager. Bose-Einstein Condensation and Liquid Helium. *Physical Review*, 104(3):576–584, November 1956.

[74] Asher Peres. Ergodicity and mixing in quantum theory. I. *Physical Review A*, 30(1):504–508, July 1984.

[75] Frank Pollmann, Vedika Khemani, J. Ignacio Cirac, and S. L. Sondhi. Efficient variational diagonalization of fully many-body localized Hamiltonians. *Physical Review B*, 94(4):041116, July 2016.

[76] Ponte Pedro, Laumann C. R., Huse David A., and Chandran A. Thermal inclusions: how one spin can destroy a many-body localized phase. *Philosophical Transactions of the Royal Society A: Mathematical, Physical and Engineering Sciences*, 375(2108):20160428, December 2017.

[77] Ionut-Dragos Potirniche, Sumilan Banerjee, and Ehud Altman. On the stability of many-body localization in $d > 1$. *arXiv preprint arXiv:1805.01475*, 2018.

[78] Andrew C. Potter, Romain Vasseur, and S. A. Parameswaran. Universal Properties of Many-Body Delocalization Transitions. *Physical Review X*, 5(3):031033, September 2015.

[79] Marcos Rigol, Vanja Dunjko, and Maxim Olshanii. Thermalization and its mechanism for generic isolated quantum systems. *Nature*, 452(7189):854–858, April 2008.

[80] V. Ros, M. Müller, and A. Scardicchio. Integrals of motion in the many-body localized phase. *Nuclear Physics B*, 891:420–465, February 2015.

[81] Pedram Roushan, Charles Neill, Jirawat Tangpanitanon, VM Bastidas, Anthony Megrant, R Barends, Y Chen, Z Chen, B Chiaro, A Dunsworth, et al. Spectral signatures of many-body localization with interacting photons. *arXiv preprint arXiv:1709.07108*, 2017.

[82] Abhisek Samanta, Kedar Damle, and Rajdeep Sensarma. Extremal statistics of entanglement eigenvalues can track the many-body localized to ergodic transition. *arXiv:2001.10198 [cond-mat]*, January 2020. arXiv: 2001.10198.

[83] Ulrich Schollwöck. The density-matrix renormalization group in the age of matrix product states. *Annals of Physics*, 326(1):96–192, January 2011.

[84] Michael Schreiber, Sean S. Hodgman, Pranjal Bordia, Henrik P. Lüschen, Mark H. Fischer, Ronen Vosk, Ehud Altman, Ulrich Schneider, and Immanuel Bloch. Observation of many-body localization of interacting fermions in a quasirandom optical lattice. *Science*, 349(6250):842–845, August 2015.

[85] Maksym Serbyn, Alexios A. Michailidis, Dmitry A. Abanin, and Z. Papić. Power-Law Entanglement Spectrum in Many-Body Localized Phases. *Physical Review Letters*, 117(16):160601, October 2016.

[86] Maksym Serbyn, Z. Papić, and Dmitry A. Abanin. Local Conservation Laws and the Structure of the Many-Body Localized States. *Physical Review Letters*, 111(12):127201, September 2013.

[87] Maksym Serbyn, Z. Papić, and Dmitry A. Abanin. Universal Slow Growth of Entanglement in Interacting Strongly Disordered Systems. *Physical Review Letters*, 110(26):260601, June 2013.

[88] Yu-Rong Shu, Dao-Xin Yao, Chih-Wei Ke, Yu-Cheng Lin, and Anders W. Sandvik. Properties of the random-singlet phase: From the disordered Heisenberg chain to an amorphous valence-bond solid. *Physical Review B*, 94(17):174442, November 2016.

[89] Rajeev Singh, Jens H. Bardarson, and Frank Pollmann. Signatures of the many-body localization transition in the dynamics of entanglement and bipartite fluctuations. *New Journal of Physics*, 18(2):023046, 2016.

[90] J. Smith, A. Lee, P. Richerme, B. Neyenhuis, P. W. Hess, P. Hauke, M. Heyl, D. A. Huse, and C. Monroe. Many-body localization in a quantum simulator with programmable random disorder. *Nature Physics*, 12(10):907–911, October 2016.

[91] Mark Srednicki. Chaos and quantum thermalization. *Physical Review E*, 50(2):888–901, August 1994.

[92] Mark Srednicki. The approach to thermal equilibrium in quantized chaotic systems. *Journal of Physics A: Mathematical and General*, 32(7):1163, 1999.

[93] Jan Šuntajs, Janez Bonča, Tomaz Prosen, and Lev Vidmar. Quantum chaos challenges many-body localization. *arXiv preprint arXiv:1905.06345*, 2019.

[94] G. Vidal, J. I. Latorre, E. Rico, and A. Kitaev. Entanglement in Quantum Critical Phenomena. *Physical Review Letters*, 90(22):227902, June 2003.

[95] Benjamin Villalonga and Bryan K. Clark. Characterizing the many-body localization transition through correlations. *arXiv:2007.06586 [cond-mat]*, July 2020. arXiv: 2007.06586.

[96] Benjamin Villalonga and Bryan K Clark. Eigenstates hybridize on all length scales at the many-body localization transition. *arXiv preprint arXiv:2005.13558*, 2020.

[97] Benjamin Villalonga, Xiongjie Yu, David J. Luitz, and Bryan K. Clark. Exploring one-particle orbitals in large many-body localized systems. *Physical Review B*, 97(10):104406, March 2018.

[98] Pauli Virtanen, Ralf Gommers, Travis E. Oliphant, Matt Haberland, Tyler Reddy, David Cournapeau, Evgeni Burovski, Pearu Peterson, Warren Weckesser, Jonathan Bright, Stéfan J. van der Walt, Matthew Brett, Joshua Wilson, K. Jarrod Millman, Nikolay Mayorov, Andrew R. J. Nelson, Eric Jones, Robert Kern, Eric Larson, CJ Carey, İlhan Polat, Yu Feng, Eric W. Moore, Jake Vand erPlas, Denis Laxalde, Josef Perktold, Robert Cimrman, Ian Henriksen, E. A. Quintero, Charles R Harris, Anne M. Archibald, Antônio H. Ribeiro, Fabian Pedregosa, Paul van Mulbregt, and SciPy 1. 0 Contributors. SciPy 1.0: Fundamental Algorithms for Scientific Computing in Python. *Nature Methods*, 17:261–272, 2020.

[99] Ronen Vosk and Ehud Altman. Many-Body Localization in One Dimension as a Dynamical Renormalization Group Fixed Point. *Physical Review Letters*, 110(6):067204, February 2013.

[100] Ronen Vosk and Ehud Altman. Dynamical Quantum Phase Transitions in Random Spin Chains. *Physical Review Letters*, 112(21):217204, May 2014.

[101] Ronen Vosk, David A. Huse, and Ehud Altman. Theory of the Many-Body Localization Transition in One-Dimensional Systems. *Physical Review X*, 5(3):031032, September 2015.

[102] Thorsten B. Wahl, Arijeet Pal, and Steven H. Simon. Efficient Representation of Fully Many-Body Localized Systems Using Tensor Networks. *Physical Review X*, 7(2):021018, May 2017.

[103] Franz Wegner. Flow-equations for Hamiltonians. *Annalen der Physik*, 506(2):77–91, 1994.

[104] Steven R White. Density matrix formulation for quantum renormalization groups. *Physical review letters*, 69(19):2863, 1992.

[105] Steven R White. Density-matrix algorithms for quantum renormalization groups. *Physical Review B*, 48(14):10345, 1993.

[106] Xiongjie Yu, David J. Luitz, and Bryan K. Clark. Bimodal entanglement entropy distribution in the many-body localization transition. *Physical Review B*, 94(18):184202, November 2016.

[107] Xiongjie Yu, David Pekker, and Bryan K. Clark. Finding Matrix Product State Representations of Highly Excited Eigenstates of Many-Body Localized Hamiltonians. *Physical Review Letters*, 118(1):017201, January 2017.

[108] Liangsheng Zhang, Bo Zhao, Trithep Devakul, and David A. Huse. Many-body localization phase transition: A simplified strong-randomness approximate renormalization group. *Physical Review B*, 93(22):224201, June 2016.

[109] Tianci Zhou and David J. Luitz. Operator entanglement entropy of the time evolution operator in chaotic systems. *Physical Review B*, 95(9):094206, March 2017.

[110] Marko Žnidarič, Tomaž Prosen, and Peter Prelovšek. Many-body localization in the Heisenberg XXZ magnet in a random field. *Physical Review B*, 77(6):064426, February 2008.